Conformational Dynamics Associated with Signaling in Tumor Necrosis Factor Receptors

A DISSERTATION
SUBMITTED TO THE FACULTY OF
UNIVERSITY OF MINNESOTA
BY

Andrew Kyle Lewis

IN PARTIAL FULFILLMENT OF THE REQUIREMENTS
FOR THE DEGREE OF
DOCTOR OF PHILOSOPHY

Dr. Jonathan N. Sachs, Adviser

December 2015

Acknowledgements

My experience at the University of Minnesota has been supported and shaped by a great number of people who deserve thanks. Anyone who has known me well enough to appear in this acknowledgement also knows that if I have ever attempted to be genuine or sentimental, it has failed awkwardly. So before I thank anyone, I first beg apology for what follows.

First and foremost, I am eternally and genuinely grateful to my adviser and mentor, Jonathan Sachs. He reached out for me to join his lab when my future in biomedical research seemed in peril. I had no experience (and truthfully, very little interest) in computational modeling, but Jonathan took me in insisting that I'd be running cell biology experiments and picking up the simulations along the way. I never thought that I'd become competent in both. Through thick and thin, he shaped me into an effective and ambitious scientist. None of this work could have been possible without his ongoing support.

Second, I would like to thank Chris Valley, my predecessor in the lab on the TNFR project, who has also been my colleague, co-author, teacher, advocate, and friend. When I was familiarizing myself with the lab, Chris did the hard work of training me in all of our protocols and tolerating my efforts as I "assisted" him with a few experiments. Everything I have done in the lab descended from his example.

I also owe thanks to the other members of the Sachs lab for their help, conversation, and company. Every one of them has shown me overwhelming kindness, even when I don't deserve it. Thanks to Jason Perlmutter, for his humor,

honesty, and rigorous expectations. Thanks to Anthony Braun for his ceaseless willingness to help and peerless expertise in membrane biology and computational methods. Thanks to Mani Vunnam for her ongoing guidance on life after graduation. Thanks also to Tiffany Senkow and Chih Hung Lo, who are taking on the TNFR project and made me, for the first time, a senior graduate student. Lastly I want to thank Ben Brummel and Ana West, who work in the other office on the other project, but are no less deserving of mention.

I would also like to thank members of the Thomas Lab, who on multiple occasions have gotten me going on a certain instrument or technique and have always been willing to share advice, reagents, or FRET constructs. Their influence is felt in nearly every chapter of this dissertation. I am also extremely grateful for all of our collaborators in the Thomas Lab, Hinderliter Lab, Cembran Lab, and Pomerantz lab. Their contributions have provided invaluable layering and depth to the work. I am especially grateful to my committee members, Dave Thomas, Alessandro Cembran, and Dave Odde, for taking the time to read this dissertation and sit for my defense.

I would like to thank my non-academic friends in Minnesota. When experiments go awry, they are there to remind me that I've still got a few things going for me. I would especially like to thank Lee Meier and my friends in the Macalester College Pipe Band. Among those I am especially thankful for Allie Schmitz.

Lastly I thank my family, especially my parents and sister. None of this would be possible without their influence through my formative years and ongoing support.

To my parents, Charlie and MaryAnn Lewis

Abstract

The long accepted model for tumor necrosis factor receptor (TNFR) signaling is that ligand binding causes receptors to trimerize, resulting in a stoichiometric change in their cytosolic domains. This model is incomplete in that it does not explain the importance of receptor self-interaction nor ligand/receptor network formation. Here, we introduce evidence for a novel TNFR activation mechanism based on network-induced conformational change in the receptor extracellular domain, which propagates through the transmembrane helices to bring about reorganization of the death domains.

First, we use normal mode analysis to suggest a mechanism whereby ligand binding induces a conformational change in the TNFR1 extracellular domain which propagates through the membrane to the cytosolic domain. We validate this experimentally by measuring FRET using fluorophore tagged TNFR1 chimeras. We then characterize a scissors-like open-to-closed transition in the disulfide-linked death receptor 5 (DR5) transmembrane dimer that couples the extracellular and cytosolic conformational changes. Using quantitative confocal image analysis, we show that DR5 ligand/receptor networks form in both the absence and presence of membrane cholesterol, but in the absence of cholesterol fail to induce signaling. These networks differ in that they do not contain disulfide-linked DR5 dimers and we run molecular simulations to offer an explanation. We then show that oxidation strengthens the methionine-aromatic interaction, a highly stabilizing motif found in many proteins including TNFR1 and DR5, using biophysical,

computational, and cell biological techniques. Lastly, we introduce mutations to the TNFR1 pre-ligand assembly domain to reduce its dimerization affinity and show that ligand binding does not directly depend on receptor self-association. Future work will determine the functional relevance of receptor dimerization and whether dimer dissociation can be exploited as a mechanism for TNFR1 signaling blockade. In summary, our results support a novel mechanism of TNFR activation that will guide the discovery and development of novel therapeutics for inflammatory disease and cancer.

Table of Contents

List of Tables

List of Figures

Preface

The contents of this thesis represent original work, published, in preparation, or submitted and awaiting review. The contributions from collaborators and publishing journals are detailed below. All other work was performed by the author, under the supervision and mentorship of Dr. Jonathan Sachs.

Chapter 2 – Adapted with permission from "Lewis, A. K., C. C. Valley, and J. N. Sachs. 2012. TNFR1 signaling is associated with backbone conformational changes of receptor dimers consistent with overactivation in the R92Q TRAPS mutant. Biochemistry 51:6545-6555." Copyright 2012 American Chemical Society.

Chapter 3 – Adapted with permission from "Lewis, A. K., Z. M. James, J. E. McCaffrey, A. R. Braun, C. B. Karim, D. D. Thomas, and J. N. Sachs. 2014. Open and Closed Conformations of the Isolated Transmembrane Domain of Death Receptor 5 Support a New Model of Activation. Biophysical Journal 106:L21-L24." Copyright 2014 Elsevier Inc.

EPR experiments were contributed by members of the Thomas lab, ZMJ, JEM, CBK, and DDT.

Chapter 4 – Article under review.

Lewis, A. K., Valley, C. C., Peery, S. L., Braun, A. R., Sachs, J. N., Death Receptor 5 networks require membrane cholesterol for proper structure and function.

Sucrose density and caspase-8 activation assays were performed by SLP and CCV. ARB assisted in scripting for image analysis.

Chapter 5 – Article under review.

Lewis, A. K**.**, Cembran, A., Senkow, T. L., Mahling R., Perell, G. T., McCarthy, M. R., Her, C., Horn, B. T., Valley, C. C., Karim, C. B., Gao, J., Pomerantz, W. C., Thomas, D. D., Hinderliter, A., and Sachs, J. N., Oxidation increases the strength of the methionine-aromatic interaction.

CSD search was contributed by GP and WCP. Quantum calculations were performed by MAJ and AC on simulations provided by AKL. CD was performed by RM, BTH, KD, and AH. Peptides were synthesized by CBK. CaM work was carried out by MRM, CH, and DDT. CaM simulations were performed by TLS.

Chapter 6 – In preparation for submission.

Chapter 1 – Introduction

1.1. The TNFR superfamily

The tumor necrosis factor (TNF) superfamily is a family of ~19 structurally related cytokines that carry out cell signaling by binding to one or more of the ~29 members of the TNF receptor (TNFR) superfamily (1). TNFs share a high degree of structural homology, but variable sequence, which allows them to target receptors with high affinity and specificity. TNFRs are type-I transmembrane proteins that mediate signal transduction for a wide range of processes including apoptosis (2), inflammation (3), cell survival (4), and lymphoid development (5). Commensurate with their role in normal signaling, TNFRs have also been implicated in a number of ailments, especially inflammatory diseases, infections, and cancer (6).

The unifying feature of the TNFR superfamily is an extracellular domain (ECD) consisting of 2 or more cysteine-rich domains (CRDs), which is responsible for binding to protein ligands (7). Each CRD is held together by pairs of disulfide-linked cysteines, which ascend the elongated TNFR structure like rungs of a ladder (8). CRDs are numbered from the N-terminus so that CRD1 is the furthest from the membrane followed by CRD2, CRD3, and so on, leading to the transmembrane domain, a single-pass α-helix that joins the ECD to the cytosolic domain. The presence of a death domain further classifies certain TNFRs as death receptors, although they do not necessarily mediate cell death. The death domain is a cytosolic region of approximately 80 residues that recruits intracellular adapter

proteins through their own death domains upon receptor activation to transduce further downstream signaling (9). Another group of TNFRs, named decoy receptors, are either secreted or membrane anchored and do not contain functional cytosolic domains. These modulate TNFR signaling by sequestering free ligand (10). The remaining members of the TNFR superfamily mediate signaling, though not through death domain interactions.

This chapter serves as an introduction to two death receptors, TNFR1 and DR5, which are the focus of this dissertation. These are selected because 1 – they are prime pharmaceutical targets for modulating inflammatory and apoptotic signaling, respectively, 2 – their structures are well studied and characterized, 3 – they both demonstrate ligand-independent self-assembly, 4 – their ligand-bound structures are highly similar, and 5 – they both demonstrate ligand/receptor clustering. These elements are critical for motivating and enabling our investigation of the conformational dynamics of death receptors upon activation using available experimental and computational, biophysical, and cell biological techniques.

1.2. TNFR1 signaling

TNFR1 is the ubiquitously expressed (11) prototypical member of the TNFR superfamily (12). The default signaling pathway of TNFR1 is pro-inflammatory and pro-survival (13). It is activated by either of two soluble ligands, TNF (TNFα) or lymphotoxin-α (LTα, also known as TNFβ) which it binds with similar affinity and to the same effect (14, 15). Both ligands also bind to TNFR2. TNF is expressed on activated macrophages and lymphocytes as a type-II transmembrane protein before it is proteolytically cleaved to produce a soluble cytokine. Before it is

cleaved, membrane bound TNF also complements soluble TNF to generate diverse responses in both the receptor and ligand presenting cells (via outside-in and inside-out signaling, respectively) by binding to either TNFR1 or TNFR2 (16). Likewise, LTα, although a soluble protein *per se*, heterotrimerizes with the type-II transmembrane protein, LTβ, similarly expanding its range of functions (17, 18). The receptor conformational dynamics that lead to signaling underlie each element of this complex system. For the sake of this dissertation, we consider the default ligand/receptor signaling pathways in model experimental systems, absent confounding effects that may occur *in situ*.

When it is activated, TNFR1 recruits adapter proteins to its cytosolic death domain to form a signaling complex. The death domain first sheds the inhibitory silencer of death domain (SODD), then binds TNFR associated death domain (TRADD) to the newly exposed binding interface (19). TRADD in turn binds to receptor interacting protein (RIP) (20) and TNFR-associated factor 2 (TRAF2) (21). The IKK complex then joins the signaling complex through TRAF2, is activated by RIP, then goes on to phosphorylate inhibitor of κBα (IκBα) (21, 22). Intact IκBα binds to the transcription factor, nuclear factor κB (NF-κB) and prevents it from entering the nucleus. When IκBα is phosphorylated and degraded (23), NF-κB is permitted to enter the nucleus where it binds directly to the genome and initiates inflammatory, pro-survival gene transcription (24). Intact IκBα can be easily detected by Western blot analysis, therefore IκBα degradation is commonly measured to monitor TNFR1 activation. Alternatively, TNFR1 mediated gene

transcription can be assessed quantitatively using a reporter plasmid with an NF-κB response element.

In certain conditions, including in some cancer cells (25), TNFR1 mediates caspase-dependent apoptosis. Instead of TRADD binding RIP and TRAF2, it recruits FAS-associated death domain (FADD) and caspase-8, which activates caspase-3 to trigger apoptosis (11). Because of its ability to induce apoptosis and true to its moniker, TNF was originally touted as a potential anti-cancer cytokine (26). Unfortunately, side effects due to the pro-inflammatory activity of TNF and LTα have prevented their systemic use as tumoricidal drugs (12).

1.3. TNFR1 in disease

TNFR1 is implicated in a range of inflammatory diseases including rheumatoid arthritis (27), TNF receptor associated periodic syndrome (TRAPS) (28), Crohn's disease (29), carotid thickening, myocardial infarction (30), deep vein thrombosis (31), and diseases of the central nervous system including multiple sclerosis (32) and Alzheimer's disease (33). These have been traced primarily to excessive, sustained expression of TNF (34-36), but also receptor mutation that results in misfolding and dysfunction (37). They been treated with great success by a class of biologic drugs called TNF-inhibitors that work by sequestering free ligand and reducing its bioavailability at sites of chronic inflammation (38). These drugs, which include Etanercept, Infliximab, and Adalimumab, sold as Enbrel®, Remicade®, and Humira®, respectively accounted for $27 billion in global sales in 2013 and represented 3 out of the top 4 best-selling pharmaceuticals (GaBI online, 2013). Etanercept is a TNFR2 fusion protein and Infliximab and Adalimumab are

both monoclonal antibodies against TNF (39). Only Etanercept binds to both TNF and LTα (40).

Despite their successes, TNF inhibitors are known to increase the risk of serious and life-threatening side effects including infections and malignancies (41). We have noted that TNF and LTα are part of a complex and balanced system of several ligands and receptors, therefore it is unsurprising that indiscriminate sequestration of ligand would result in some unexpected cell responses. Therefore, it is desirable to treat inflammatory disease by targeting TNFR1 directly, leaving the normal functional relationships among LTα, LTβ, TNF, TNFR2, and LTβ receptor intact. TNFR1-specific inhibition using domain antibodies or peptides has been successful in mouse models (37, 42), however an explanation of the mechanism of this inhibition is lacking. Therefore, a detailed understanding of the biophysical events that control ligand/receptor signaling is needed to rationally design and improve therapies for diseases associated with TNFR1 dysfunction.

1.4. DR5 signaling and therapeutic interest

Whereas TNFR1 primarily signals cell survival, DR5 almost always mediates apoptosis. DR5 is expressed as both a short and long isoform (DR5-S and DR5-L, respectively) which differ by the absence or presence of 29 amino acids at the junction between the ECD and the transmembrane domain (43). Both isoforms are activated by a common ligand, TNF-related apoptosis-inducing ligand (TRAIL or Apo2L) (44). When stimulated, it recruits FADD and caspase-8 to its death domain and initiates caspase-dependent apoptosis (45). DR5 has attracted therapeutic interest because it selectively mediates cell death in cancer cells,

leaving normal cells unaffected (46). Indeed, the TRAIL/DR5 apoptotic mechanism seems, at least in mice, to be part of normal tumor suppression, and the loss of TRAIL sensitivity may mark a critical step in tumor initiation and proliferation (47). The idea of using DR5 as a specific mediator of tumor apoptosis has driven the development of non-natural DR5 agonists (45, 48) and innovative superagonists (49, 50) to overcome TRAIL insensitivity. However, TRAIL resistance continues to be an obstacle and a more detailed understanding of the biophysical events surrounding DR5 activation is necessary (51, 52)

1.5. TNFR1 and DR5 structure, self-assembly, ligand-binding, and clustering

Despite their disparate functions, TNFR1 and DR5 share a number of structural characteristics that make them amenable to our pairwise investigation. Firstly, both receptors self-associate in the absence of ligand through a pre-ligand assembly domain (PLAD). When treated with the amine crosslinker, BS3, and analyzed by electrophoretic mobility shift, unliganded DR5 migrates as a trimer (43). Because BS3 is membrane impermeable, this assay shows that DR5 forms non-covalent trimeric interactions via its extracellular domain. However, its transmembrane domain contains obvious *dimerization* features. These include a cysteine (C209) in DR5-L which forms a disulfide bond with an apposed DR5-L chain upon ligand stimulation and a GxxxG dimerization motif, exactly one helix turn downstream (43, 53). DR5-S also contains this GxxxG motif and is believed to non-covalently dimerize, however it lacks a cysteine and cannot form a disulfide bond (43). The functional significance of this difference is not fully understood. One theory speculates that the disulfide linkage disrupts the symmetric architecture of

otherwise non-covalent ligand/receptor networks (explained below) containing both DR5-S and DR5-L, thereby limiting signaling (43). Alternatively, disulfide bonding is proposed to enhance DR5-L activity by locking it into a signaling-competent dimeric architecture (53). It is notable that a disulfide bond in another TNFR, p75 has been shown to be critical for receptor activation (54). No crystal structure yet exists for unliganded DR5.

As for TNFR1, an influential publication by Chan et al. has referred to its preligand state as trimeric (55), however more recent studies clearly state that it is dimeric (56). TNFR1 was first shown to dimerize by Naismith et al. in a crystal structure of its extracellular domain (57). Dimerization was shown to occur through symmetric non-covalent interactions in CRD1. TNFR1 was later shown to self-associate in live-cells, again by crosslinking cell surface proteins with the membrane impermeable amine crosslinker BS3. Unlike DR5, TNFR1 lacks any discernable dimerization motif in its transmembrane domain aside from a cysteine near its midpoint. However, as of this writing, this cysteine has not been shown to participate in a disulfide bond (55).

Structures of TNFR1 both with and without ligand have facilitated investigation into its manner of activation. Experimental evidence (58) first led to a model of stoichiometrically-driven activation. That is, the ligand-induced TNFR1 death domain trimer was hypothesized to permit binding of cytosolic adapter proteins, while the standalone death domain would not constitute the requisite TRADD binding-competent unit. The crystal structure of the LTα/TNFR1 complex (1tnr) seems to support this model, showing individual, non-interacting receptor

chains binding along the grooves between adjacent LTα protomers (8). The crystal structure of the TRAIL/DR5 complex (1d0g) shows these same general features suggesting a common manner of activation (59).

The structure of the preligand TNFR1 dimer strikingly revealed that its ligand-binding and self-assembly domains do not overlap. This led to speculation that the TNFR1 dimer could survive ligand binding, and rather than form trimers, it would form an extended hexagonal network in which ligand/receptor complexes constitute the vertices and receptor dimers form the edges (57). This model was advocated by others for TNFR1 (56, 60, 61) and extended to other TNFR superfamily members including DR5 (43) and Fas (62). Crosslinking experiments confirmed the formation of high-molecular weight oligomeric complexes of TNFR1 (55) and DR5 (43) upon ligand binding. Clustering has also been visualized by confocal microscopy for Fas (63-65), DR5 (43), and TNFR1 (66, 67).

Thus, while TNFR1 and DR5 activation is ultimately triggered by ligand binding, the trimerization model is incomplete in that it does not explain the importance of receptor self-interaction or ligand/receptor network formation. Furthermore, it does not account for ligand-independent activation observed when receptors are overexpressed (19, 68, 69).

This work introduces evidence for a novel TNFR activation mechanism based on ligand-induced conformational change in the receptor ECD, which propagates through the transmembrane helices to bring about reorganization of the death domains. We propose an ECD conformational change driven by ligand/receptor, receptor/receptor, and receptor/membrane interactions incurred

upon network formation. This conformational change induces a hinging motion through the transmembrane dimer, which reconfigures the cytosolic domains so that they are able to recruit adapter proteins. The studies are carried out for TNFR1 and DR5, however due to common structural characteristics across the TNFR superfamily, our results may be broadly generalizable. We selected TNFR1 for analysis of the extracellular domain because structures exist for both its ligand-bound and unbound states. The long isoform of DR5 was selected for studies of the transmembrane domain because its disulfide bond reduces the accessible conformational degrees of freedom and makes tractable the problem of predicting its structure. We hope to guide the discovery and development of novel therapeutics that exploit the features of this activation model to provide safer and more effective treatments for inflammatory disease and cancer.

Chapter 2 – TNFR1 Signaling is Associated with Backbone Conformational Changes of Receptor Dimers Consistent with Overactivation in the R92Q TRAPS Mutant

Adapted with permission from “Lewis, A. K., C. C. Valley, and J. N. Sachs. 2012. TNFR1 signaling is associated with backbone conformational changes of receptor dimers consistent with overactivation in the R92Q TRAPS mutant. Biochemistry 51:6545-6555.” Copyright 2012 American Chemical Society.”

2.1. Summary

The widely accepted model for tumor necrosis factor 1 (TNFR1) signaling is that ligand binding causes receptor trimerization, which triggers a reorganization of cytosolic domains and thus initiates intracellular signaling. This model of stoichiometrically driven receptor activation does not account for the occurrence of ligand independent signaling in over-expressed systems, nor does it explain the constitutive activity of the R92Q mutant associated with TRAPS. More recently, ligand binding has been shown to result in the formation of high molecular weight, oligomeric networks. Although the dimer, shown to be the pre-ligand structure, is thought to remain present within ligand-receptor networks, it is unknown whether network formation or ligand-induced structural change to the dimer itself is the trigger for TNFR1 signaling. In the present study, we investigate the available crystal structures of TNFR1 to explore backbone dynamics and infer conformational transitions associated with ligand binding. Using normal mode analysis, we characterize the dynamic coupling between the TNFR1 ligand binding

and membrane proximal domains and suggest a mechanism for ligand-induced activation. Furthermore, our data are supported experimentally by FRET showing that the constitutively active R92Q mutant adopts an altered conformation compared to wild-type. Collectively, our results suggest that the signaling competent architecture is the receptor dimer, and that ligand binding modifies domain mobilities intrinsic to the receptor structure, allowing it to sample a separate, active conformation mediated by network formation.

2.2. Introduction

Tumor necrosis factor (TNF) receptor 1 (TNFR1) is the prototypical member of the TNFR superfamily, a family of roughly 20 type I transmembrane receptors whose functions include triggering apoptosis,(2) inflammation response,(3) and cell survival.(4) TNFR1 is activated by binding one of two cognate ligands, TNFα or lymphotoxin-α (LTα, also called TNFβ) via its extracellular domain.(70) Upon ligand binding, a yet uncharacterized rearrangement of TNFR1 in the extracellular domain results in signal transduction across the membrane, causing the TNFR1 intracellular death domain to shed the silencer of death domain (SODD)(19) and subsequently bind to TNF receptor associated death domain (TRADD).(71) The signaling cascade culminates with NF-κB activation and inflammation response.(72) A less common outcome occurs in certain cell types and culture conditions wherein TRADD recruits Fas associated death domain (FADD), resulting in caspase activation and apoptotic cell death.(73) However TNFR1 is most commonly associated with its inflammation pathway.

Abnormal TNFR1 activity is linked to a number of diseases including rheumatoid arthritis,(27) TNF receptor associated periodic syndrome (TRAPS),(28) Crohn's disease,(29) carotid thickening, myocardial infarction,(30) deep vein thrombosis,(31) and diseases of the central nervous system including multiple sclerosis.(32) These diseases have been linked to a number of polymorphisms in the extracellular domain which cause abnormal folding, oligomerization, trafficking, and shedding behavior. Additionally, most mutants are unable to bind ligand. Notable exceptions are the R92Q and P46L mutations, which are termed "nonstructural polymorphisms" in that they bind ligand, traffic, and shed like wild-type, but exhibit abnormal, ligand-independent activity and lead to disease symptoms, albeit milder ones.(37) Common treatments for TNFR1 associated inflammatory diseases include etanercept, adalimumab, and infliximab.(38) Each of these drugs reduces symptoms by competitive inhibition, capturing free ligand and rendering it unable to bind receptor. However, no current treatments act directly on the TNF receptor, which may reflect a lack of knowledge regarding extracellular signaling mechanisms involving TNFR1. Therefore, a detailed understanding of the mechanism by which ligand binding to TNFR1 results in signal transduction across the membrane may provide valuable insight into targeting TNFR1.

While downstream events of the TNFR1 signaling pathway are well characterized, the mechanism by which ligand induces signaling across the membrane—i.e. ligand-independent receptor activation and ligand-induced reorganization in the membrane—is poorly understood. Therefore, the

fundamental relationship between the structure and function of TNFR1 is of great interest. TNFR1 is comprised of an N-terminal extracellular domain, a single-pass α-helical transmembrane (TM) domain, and a cytosolic death domain. Within the extracellular domain, two distinct regions of the receptor serve two main functions, pre-ligand assembly of monomeric receptor units(55) and ligand-binding of these pre-assembled complexes.(74) Ligand-independent assembly (Figure 2-1A) is driven through the membrane-distal pre-ligand assembly domain (PLAD), and deletion of these residues has been shown to prevent the homomeric association of TNFR1 monomers.(55) Ligand binding (Figure 2-1B) is driven through two receptor loops which provide high-affinity, high-specificity binding via a number of non-covalent interactions.(8) Recent evidence has suggested that in TNFR1, as well as other closely related proteins including TNF-related apoptosis-inducing ligand receptor 2 (TRAIL2, death receptor 5, DR5),(43) ligand-independent interactions and ligand binding occur together to generate highly organized network structures, (Figure 2-1C)(56) discussed further below. However, it is still unknown how the transition from a ligand-independent structure to a ligand-bound structure leads to signal transduction across the membrane.

TNFR1 is the only member of the TNFR superfamily for which crystal structures exist for both its ligand unbound (Figure 2-1D) and ligand bound (Figure 2-1E) states, albeit the extracellular domain only. The first structure solved was that of the TNFR1 ectodomain in complex with its ligand, LTα (PDB ID 1tnr, Figure 2-1E), revealing that the homotrimeric ligand binds symmetrically to three non-interacting TNFR1 protomers, with each protomer fitting into the groove between

adjacent ligand chains.(8) This trimeric, axisymmetric LTα-TNFR1 complex agrees with previous experimental evidence for 3:3 ligand-receptor binding stoichiometry and is often considered to be the signaling complex.(58) The receptor itself is comprised of a chain of 4 cysteine rich domains (CRDs), with each CRD stabilized by three pairs of disulfide-linked cysteine residues.(75) The ligand contacts are confined to CRD2 and CRD3. More specifically, ligand-receptor interactions in the receptor protomer are dominated by a loop at residues 77-81 and the turn of a beta hairpin between residues 107-113.(8)

A second crystal structure was later solved for the TNFR1 ectodomain pre-ligand homodimer (PDB ID 1ncf, Figure 2-1D).(57) An anti-parallel dimer structure was also solved, but is not generally believed to be relevant in a native biological system. The dimer structure reveals that in the absence of ligand, TNFR1 self-interacts with extensive dimer interactions in CRD1, the PLAD. In fact, only a single dimer interaction is found outside of the PLAD, a pair of hydrogen bonds between opposite Glutamines at residue 133. The significance of this pair of hydrogen bonds is unknown.

Despite there being crystal structures solved for TNFR1 in both its ligand-independent and ligand-bound forms, the relevant signaling mechanism at the level of receptor activation—that is, the transition from a ligand-independent dimer to a ligand-bound trimer—is still not known. Comparison of the two crystal structures, 1ncf and 1tnr, has not previously revealed any definitive tertiary structural difference between the ligand-independent and ligand-bound receptor.(57) Moreover, it is notable that the ligand binding domain and the PLAD

are on opposite faces of the receptor, and a structural alignment of the two crystal structures reveals that the homodimer can survive ligand binding without masking the dimerization interface or producing steric interference (Figure 2-1F). Despite these domains being structurally distinct, their functions have largely been considered intrinsically linked. Deletion of the membrane-distal PLAD prevents ligand binding and function, and therefore it is presumed that ligand-independent receptor assembly is a prerequisite for ligand binding and function.(76) However these studies are largely based upon receptor mutational analysis whereby entire protein domains are removed, which could influence the structure of ligand-binding regions. The structures of sequential CRDs are interdependent and folding of TNFR1 is highly sensitive to mutation.(37) Therefore, the relationship, if one exists, between the pre-ligand assembly domain and the ligand binding domain is yet unclear.

Nevertheless, ligand binding and dimerization do not appear to be mutually exclusive. Consequently, ligand binding does not necessarily result in the formation of a trimer, but an extended network of ligand/receptor complexes. Indeed, a crosslinking study by Chan et al. shows that ligand binding results in the appearance of high molecular weight oligomers, rather than the expected trimer/trimer complex.(55) Our recent work has emphasized specific ligand-induced receptor dimerization within the network structure of TRAIL in complex with DR5, a structurally homologous TNF ligand-receptor pair.(43) However, despite well-defined crystallographic structural data for the TNFR1 homodimer, its role within the TNFR1-LTα network has not yet been characterized. The model

proposed by our group and others is a hexagonal lattice wherein the ligand bound trimer forms each vertex and the receptor homodimer forms each edge (Figure 2-1 A-C).(43, 56, 61, 62)

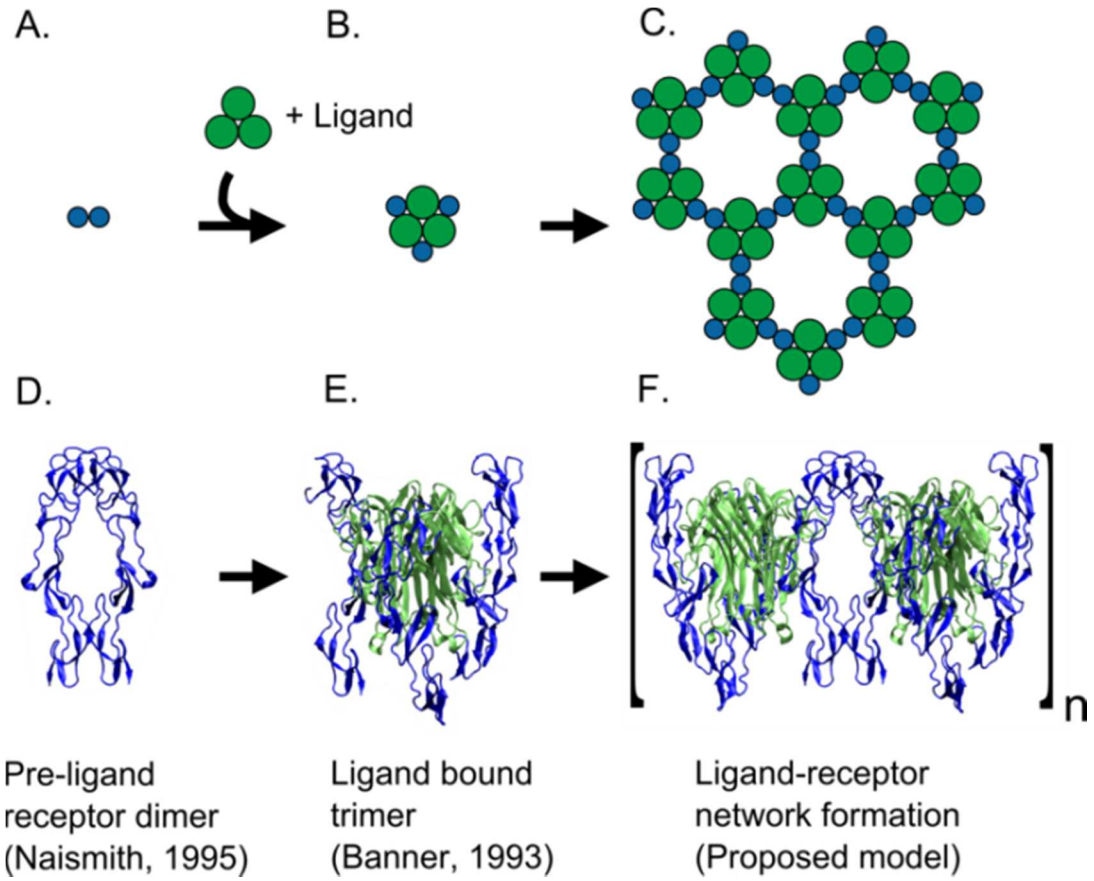

Figure 2-1. Ligand-receptor network model. The components of the TNFR1 hexagonal network are shown schematically with accompanying crystal structures. The receptor exists on the cell surface as a pre-ligand dimer (A, D). The trimeric ligand binds to three receptor protomers with trifold symmetry (B, E). However, this structure is not found in crosslinking studies, rather the ligand causes the formation of high molecular weight oligomers, modeled as a hexagonal lattice (C). The dimer of trimers subunit (i.e. a pair of ligand-bound trimers associated via the receptor dimerization interface) is the smallest networked unit (F).

Due to the structural similarity between receptor protomers in the 1ncf and 1tnr, an all-atom representation of such a network can be generated by structural alignment of the crystal structures (Figure 2-1F). The trifold symmetry of the

ligand/receptor complex leads to a hexagonal geometry as modeled. However, a conflict becomes apparent upon generation of the network through receptor-receptor dimerization of ligand-receptor trimers (i.e. “dimer of crystal structure trimers”) shown in Figure 2-1F. An overlay of the crystal structures producing the dimer of trimers structure reveals a tilt of approximately 35˚ between adjacent trimers so as to prevent this network from forming on a membrane that is essentially planar on the scale of protein geometry. Therefore, we propose a ligand-induced conformational change that causes the network to become planar and permit its formation as observed in experimental studies. We use normal mode analysis, a powerful computational tool that has been used to accurately describe structural transitions in a variety of proteins (77-79), to explore the conformational dynamics involved in ligand binding of TNFR1. Our observations are supported in part by our experiments and should inspire additional experiments in the future. In the present study, we investigate the backbone conformational dynamics of TNFR1, how they relate to signaling, and potential connections to ligand-receptor network formation.

2.3. Methods

2.3.1 Comparison of crystal structures

All protein coordinates were obtained from the Protein Data Bank (PDB, www.pdb.org, PDB ID 1ncf and 1tnr). The structural alignments and root mean square deviations (RMSD) were calculated using the RMSD Calculator extension of VMD.(80) The calculations were performed on the backbone atoms of the

indicated residues of both 1ncf chains (chains A and B) and the 1tnr receptor chain (chain R).

2.3.2 Normal mode and RMSF calculation

We calculated the full set of 3N normal modes for the Cα representations of the 1ncf and 1tnr crystal structures using the anisotropic network model tool, applying an exponential spring function, in LOOS.(81) The 1ncf chains were truncated to contain residues 14 to 150 for the purpose of symmetry, and the trifold symmetric 1tnr structure was kindly provided by David Banner.

The output eigenvectors and eigenvalues were used to calculate the mean square residue fluctuations according to

$$\langle \Delta r_i^2 \rangle \propto \sum_v \frac{e_i^2(v)}{\omega_v^2}, \text{ [1]}$$

where $e_i(v)$ and ω_v are the eigenvectors and angular frequency respectively of the dynamical matrix corresponding to atom i and mode v.

2.3.3 Cross-correlation calculation

Cross-correlation maps were calculated over the first 100 non-zero frequency normal modes according to

$$C_{i,j} = \frac{\sum_1^k \frac{e_i \cdot e_j}{\omega_k^2}}{\left(\sum_1^k \frac{e_i \cdot e_i}{\omega_k^2}\right)^{1/2} \left(\sum_1^k \frac{e_j \cdot e_j}{\omega_k^2}\right)^{1/2}}, \text{ [2]}$$

where e_i and e_j correspond to the eigenvectors of residues *i* and *j* respectively and ω_k is the angular frequency of the kth normal mode. Convergence was estimated by taking the Euclidean norm of the cross-correlation matrix.

2.3.4 FRET

pEYFP-N1 and pECFP-N1 vectors were a kind gift from David Thomas. The fluorophores had been previously mutated (A206K) to prevent dimer formation.(82) cDNA encoding TNFR1 was inserted at the n-terminus of the pEYFP-n1 and pECFP-n1 vectors using standard cloning technique. The TNFR1 sequence was truncated immediately downstream of the transmembrane domain such that the cytosolic domain was replaced with EYFP or ECFP. The R92Q mutation was introduced using standard point-mutagenesis technique and sequenced for verification.

HEK 293 cells were plated at 1:12 in a 6-well plate and transfected 48 hours later as follows. 0.5 µg ECFP-TNFR1 and 1.5 µg EYFP-TNFR1 were diluted into 25 µL 20mM HEPES. A second solution of 50 µg/mL polyethyleneimine (branched, MW ~25000) in 20mM HEPES was prepared. The two solutions were mixed at 1:1 by pipetting repeatedly and incubated at room temperature for 30 minutes. Cells were gently washed twice and resuspended in serum free DMEM. The DNA solution was added (50 µL total volume into each well of a 6-well plate) and the cells were incubated 4 hours at 37º C. The cells were then washed twice and incubated in serum-containing DMEM for 20 hours. Immediately prior to FRET imaging, cells were lifted by gentle trypsinization and replated on poly-D-lysine coated plates.

Live-cell FRET imaging was conducting using a Nikon Eclipse TE200 inverted microscope and a 40x objective fitted with a mercury lamp (XCite 120W Fluorescence Illumination System). Filters for excitation and emission of CFP

(430/24nm and 470/24nm, respectively) and YFP (500/20nm and 535/30nm, respectively) were controlled using an automated filter wheel (LudI MAC6000). Images were acquired using MetaMorph and analyzed with ImageJ. Energy transfer was measured by acceptor-selective photobleaching. Briefly, cells were imaged in the EYFP and ECFP channels every 20 seconds for 3 minutes. Between image captures, acceptor was bleached by continuous exposure through the EYFP excitation channel. FRET efficiency was calculated as the intercept of the linear fit of normalized EYFP fluorescence plotted against normalized ECFP enhancement with typical R^2 values of around 0.90. The FRET efficiencies measured from individual cells were plotted against EYFP intensity and fit to a two parameter saturable binding curve of the form

$$E = \frac{FRET_{max}[EYFP]}{K_D + [EYFP]}. \quad [3]$$

The model parameters were extracted to determine relative binding affinity (K_D) and maximum FRET efficiency ($FRET_{max}$) of the TNFR1 dimer.

2.4. Results

2.4.1 Structural differences between the 1ncf and 1tnr receptor crystal structures

To determine whether specific structural differences exist between TNFR1 in its ligand-independent dimeric and ligand-bound trimeric states, we used VMD to perform a global backbone structural alignment and calculate the RMSD between the pre-ligand 1ncf receptors and the ligand bound 1tnr receptor. We calculated the backbone RMSD on all resolved residues shared among the crystal structures (residues 15-150) between chains A and B of 1ncf and chain R of 1tnr.

The pre-ligand receptor protomers differ from each other by an RMSD of 1.12 Å, with chain B appearing slightly more curved than chain A. The RMSD between 1ncf chains A and B and 1tnr chain R are 1.68 Å and 1.96 Å, respectively. Naismith et al. originally reported the dimer structure and noted that the trimeric 1tnr receptor protomer solved 2 years prior by Banner et al. is slightly elongated and straighter compared to their pre-ligand dimer structure. Nevertheless, upon global alignment of all resolved residues, the structural differences between 1tnr and 1ncf appear to be minimal and are not consistent with our expectation of a ligand induced conformational change in the cytosolic domain (Figure 2-2A). However, the alignment algorithm results in structural deviations being distributed globally such that the total RMSD is minimized. If instead we assume that the dimer interface survives ligand binding and the PLAD remains rigid, it is reasonable to perform the alignment on only these residues, such that the dimer interactions remain intact. Moreover, we note that the B-factors of the 1ncf receptor suggest that residues 15-100 are relatively immobile compared to residues 101-150 (see Supporting Information), supporting the notion that residues involved in dimeric interactions within the PLAD are unchanged upon ligand binding if we assume preservation of the dimer. We calculated a local backbone alignment and RMSD based on only residues 15-100. While residues 15-100 align more tightly (RMSD = 0.83 Å and RMSD = 0.72 Å between chain R of 1tnr and chains A and B of 1ncf, respectively), a structural change becomes apparent in the ligand binding and membrane proximal domains (Figure 2-2B). The RMSDs calculated on residues 100-150 between chain R and chains A and B are similarly reduced (RMSD = 0.83 Å and

RMSD = 0.79 Å respectively), again showing that the differences between the ligand bound and ligand unbound structures correspond to a rigid body motion within the receptor protomer. Specifically, we found that in 1tnr, the ligand binding loop at residue 110 drops toward the membrane and that the membrane proximal domain rotates away from the dimerization interface. We then reconstructed the receptor dimer by aligning residues 15-100 of the 1tnr receptor protomer with both chains of 1ncf and found that the membrane proximal residues are substantially further apart, consistent with a conformational change in the TM and cytosolic domain (Figure 2-2C). These results show clearly that structural differences exist between TNFR1 in its dimeric state, and ligand-bound trimeric state. Whether this structural change is truly a consequence of ligand binding or of other crystallization conditions is unknown, however it does demonstrate a large degree of flexibility between the dimerization interface and the ligand binding and membrane proximal domains, which may be relevant to signaling in the full-length, membrane-anchored receptor.

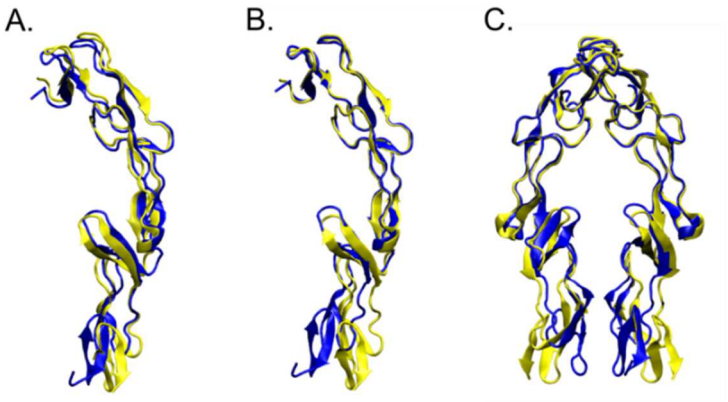

Figure 2-2. Alignment of the 1ncf and 1tnr receptor protomer structures. The alignment of 1ncf chain B (blue) and 1tnr chain R (yellow) shows that the global structural differences between the two structures are minimal (A). Alignment along residues 15-100 reveals a structural change in the membrane proximal residues, mediated by flexibility within the receptor chain (B). The structural change in the

membrane proximal residues becomes even more apparent when the 1tnr protomer is superposed onto both chains A and B of 1ncf (C).

2.4.2 Comparison of the crystal structures reveals increased flexibility in the PLAD of the ligand-bound trimer

To more completely characterize the backbone mobility of the TNFR1 protomer as well as the collective motions of the tertiary structure involved in the transition from the ligand unbound dimer to the ligand bound trimer, we calculated the normal modes of both the 1ncf and 1tnr structures. To date, the dynamic behavior of the TNFR1 backbone has been largely disregarded and its relationship to signaling has not been investigated. Normal mode analysis (NMA) is a powerful tool used to characterize the large-amplitude structural fluctuations of a protein, including conformational changes that occur on time scales not accessible by all-atom molecular dynamics. We calculated the normal modes of both structures using LOOS, which employs the anisotropic network model (ANM), reducing computational cost by coupling atoms through a single parameter energy potential in place of the traditional all-atom empirical force field.(81) ANM reveals the 3-dimensional structural properties of a protein by assuming that, while residue-specific atomic interactions guide the determination of the folded state, once folded the protein behaves to a large extent as an elastic solid, and molecular forces stabilizing the 3-dimensional geometry dominate.(83) The model is further simplified by reducing the treatment of residues to alpha-carbons only. While this appears to be an oversimplified model, normal mode analysis has been shown to

accurately predict structural changes in proteins in which multiple conformational states are known.(77, 84-86)

The protomer chains of 1ncf were truncated for symmetry to include only residues 14-150. The truncated residues (11-13 and 151-155) can reasonably be omitted because they form incomplete domains with negligible intramolecular contacts and do not contribute meaningfully to the resolved portion of the tertiary structure. To analyze the relative residue fluctuation of the receptor protomer, we summed the full set of 3N-6 inverse-eigenvalue weighted normal modes according to Equation 1. The peaks on the resulting plot show which regions of the backbone tend to be more mobile, with low-frequency collective motions dominating while high-frequency vibrations offer negligible contributions (Figure 2-3A). The two crystal structures show notable differences in the mobility of various protein regions.

In the all-atom representation, extensive non-covalent interactions within the PLAD of the 1ncf crystal structure at residues 47-49 stabilize the dimer interface (Figure 2-3A, Region ii). These residues are in turn stabilized by the loop formed at residues 23-27 (Region i), which does not form any dimer contacts, but is structurally coupled to the dimer interface of the PLAD. Comparing the residues fluctuations from the normal mode analysis of the homodimerized state (i.e. 1ncf) to the ligand-bound trimer state (i.e. 1tnr), both Regions i and ii are more flexible in the ligand-bound state due to the loss of dimeric intermolecular interactions across the PLAD interface. While the intermolecular side chain interactions that join the dimer are not present in our coarse-grained representation, the two chains

are near enough in the dimeric 1ncf structure that the exponentially decaying potential between them substantially influences the normal modes of the system. In the dimer state, these residues are surrounded by a larger number of close range interactions, and the region expectedly becomes more rigid, in agreement with the B-factors and justifying our treatment of the crystal structures.

2.4.3 The ligand bound state exhibits disparate flexibility in the ligand binding domains

The two predominant ligand binding domains of TNFR1 are formed by a loop at residues 77-81 (Figure 2-3A, Region iii) and the turn of a β-hairpin at residues 107-113 (Figure 2-3A, Region iv). They are coupled by a hydrogen bond between the backbone carbonyl of residue 80 and the backbone nitrogen of residue 114, which along with residue 104 transect the midpoint of the beta sheet. The midpoint of the beta sheet is further stabilized through a hydrogen bond between residues 104 and 131. Although the two ligand binding regions are tangentially coupled, they form two distinct and independent domains (Figure 2-3, Regions iii and iv), as the essential ligand binding residues of the β-hairpin are formed distally at residues 107-108. Furthermore, the two ligand binding domains target separate sets of residues within two separate protomers of the trimeric ligand.(8)

In the dimer state, both ligand binding domains are flexible due to the absence of ligand interactions. Region iii runs along the spine of the receptor protomer and forms multiple intramolecular contacts, while the beta hairpin (Region iv) projects prominently from the structure, tethered only at its midpoint.

As a result, the beta hairpin is substantially more mobile. Fluctuations in residues 77-81 are fully damped when buried by ligand binding, while Region iv remains somewhat flexible. If we treat the ligand as a rigid extension of the ligand binding domains, it is apparent that fluctuations in the β-hairpin would act to rotate the ligand about the rigid 77-81 loop. Conversely, this shows that the ligand can reorient with respect to the principal axes of the receptor by displacing Region iv while Region iii remains stationary.

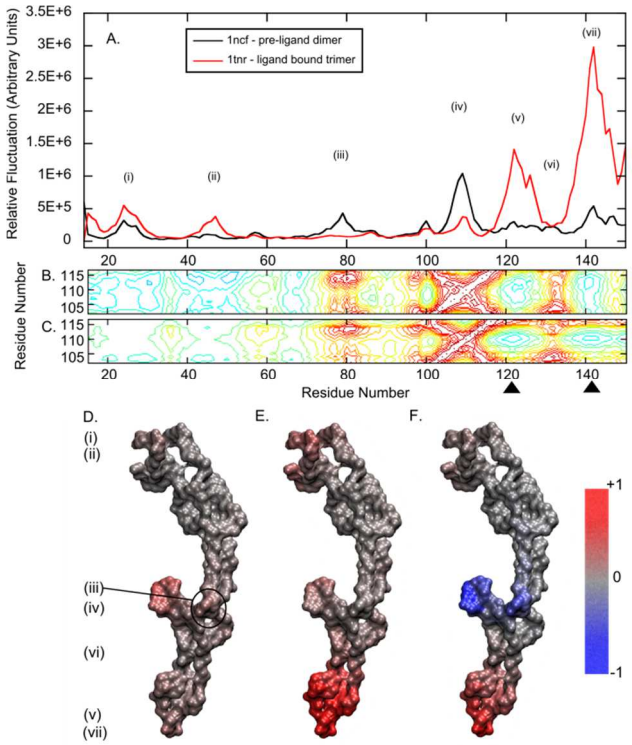

Figure 2-3. Normal mode analysis of the 1ncf and 1tnr structures. The residue fluctuations are shown for 1ncf (black) and 1tnr (red), summed over the full set of 3N-6 normal modes (A). The equal-time motional correlations are shown for residues 105-115 for 1ncf (B) and 1tnr (C). Normalized residue mobility is shown schematically for the 1ncf protomer (D) and 1tnr (E), with the difference (i.e. 1ncf mobility subtracted from 1tnr mobility) shown in (F). Relative mobility and differences in mobility are indicated according to the color bar.

2.4.4 The transition to the ligand bound state enhances flexibility in the membrane proximal domains

Approximately 22 residues leading to the TM domain are unresolved in both solved crystal structures and they are not believed to play a role in either ligand binding or dimerization.(57) The missing residues are expected to be highly structured, forming CRD4, which is stabilized by 3 pairs of disulfide-linked cysteines. The crystal structure gives coordinates for approximately half of CRD4, and we assume that the behavior of these residues reflects, or at least has direct influence on the behavior of the rest of the domain as well as the TM helix.

The membrane proximal domains (Regions v and vii) fluctuate modestly in the dimer structure, and the transition to the ligand bound state causes their mobility to increase dramatically (Figure 2-3A, F). That ligand binding results in such a substantial increase in the fluctuations of the membrane proximal residues is by itself evidence for ligand-induced conformational change in the TM domain, however we sought to determine the mechanism through which ligand binding exerts this influence. A potential explanation is that dimerization contacts, though they are few and long-distance, contribute to the stability of these regions in the 1ncf structure. However, the sole dimerization interaction outside of PLAD is a pair of hydrogen bonds formed symmetrically by apposed Q133 residues (Region vi), and the mobility at this residue is unaffected by the loss of dimer. Furthermore, we later show that the membrane proximal residues are flexible even where ligand-receptor trimeric and receptor-receptor dimeric interactions are present as in the ligand-receptor network model (discussed below). Thus, the increased flexibility in

Regions v and vii appears to be an allosteric effect of ligand binding, and not a direct result of dimer dissociation.

2.4.5 Motions in the 107-113 ligand binding loop and the membrane proximal domains are coupled

Comparing the fluctuations of the ligand-independent and ligand-bound crystal structures, we have shown two striking features that coincide with the transition from the ligand-independent receptor dimer state to the ligand-bound trimeric state. First, two regions of the TNFR1 protomer, one rigid and one flexible, bind to the ligand at two distinct sites, and second, ligand binding causes dramatically enhanced flexibility in the membrane proximal domains. In order to determine whether these phenomena are related, and if so, how the mobilities of these regions are correlated, we calculated the equal-time motional correlation between all residues pairs of the receptor protomer (for complete cross-correlation analysis of TNFR1 1ncf and 1tnr structures, see Supporting Information). The individual analysis of low-frequency normal modes provides valuable insight into large scale structural changes between functional conformations, however the observation of correlated motions between protein domains in a single eigenvector does not necessarily imply that they are coupled over the full range of motion of the system.(87) Therefore, to understand the coupled motions of protein domains, it is necessary to calculate the cross-correlation over a sufficient range of normal modes such that the cross-correlation matrix becomes converged. We calculated the cross-correlation over the first 100 non-zero frequency normal modes

according to equation 2, using the Euclidean norm as an estimate of convergence (see Supporting Information).

The cross-correlation is shown for TNFR1 residues 100-117, the mobile ligand binding β-hairpin, for both the 1ncf and 1tnr structures (Figure 2-3B and C, respectively). Qualitatively, the correlation peaks do not appear to change upon ligand binding. If we assume that the signaling competent unit is the dimer and that the ligand initiates signaling through coupled deformation of the membrane proximal region via the ligand-binding β-hairpin, this demonstrates that the ligand-independent dimer is intrinsically predisposed to the same correlated motions as the ligand-bound trimer, and is thus capable of initiating signaling. What differs is the relative mobility of the ligand binding and membrane-proximal domains in each structure (Figure 2-3A); so while the liganded complex is flexible and may access the signaling conformation with ease, the pre-ligand dimer is rigid and reaches the signaling conformation with relatively lower frequency. This result suggests that the ligand-independent dimer is capable of initiating signaling, consistent with results showing that unliganded TNFR1 triggers NF-κB activation when overexpressed(19) or in the case of the constitutively active R92Q mutant.(88) Moreover, ligand binding to the wild type receptor changes the overall energy landscape thus providing access to a range of active structures that are inaccessible (or energetically unfavorable) in the absence of ligand.

As mentioned above, residues 104 and 114 are structurally proximal and functionally related to residue 80, which is reflected by highly correlated motion between them (Figure 2-3B, C). Positive correlation is present between the ligand

binding residues of the β-hairpin and residues 77-81, however this appears to be an indirect effect of the strong structural coupling at the midpoint of the beta sheet. Positive correlation at residues 107 and 108 is greatly diminished compared with residues 104 and 114, suggesting that it is merely a consequence of structural proximity. Also, the mobility of residue 80 is abolished in the ligand bound state as shown in Figure 2-3A, so although the motions are somewhat correlated, they are negligible in magnitude and likely correspond to modest rigid body translations.

The ligand binding β-hairpin (Region iv) and the membrane proximal domains (Regions v and vii) are mobile (Figure 2-3A), and their motions are highly anti-correlated, as shown by the negative peaks localized at residues 120 and 140 (Figure 2-3B, C, arrowheads). That is, motion in Region iv tends to cause opposite motion in Regions v and vii. Recalling the structural arrangement of the immobile residues, the ligand binding domain and the membrane proximal domains appear to rotate through a rigid axis defined by residues 80, 104, 117, and 133 (Figure 2-4). If we again consider the ligand as a rigid extension of the ligand binding domains and assume that the behavior of the TM domain is heavily influenced by that the membrane proximal residues, it follows that reorientation of the ligand about the principal axes of the receptor may propagate through CRD4 to generate a structural change in the TM domain.

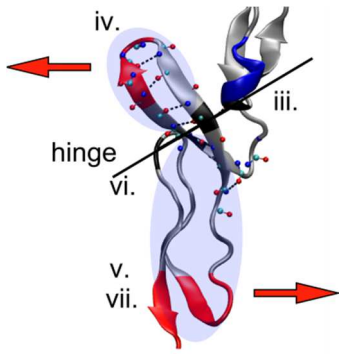

Figure 2-4. The ligand binding region is coupled with the membrane proximal residues. The anti-correlated ligand binding domain and membrane proximal residues are highlighted. The correlation analysis suggests that Region iv and Regions v and vii rotate as a rigid body about the axis defined by the immobile residues 80, 104, 117 and 133 (black line). This reveals a mechanism by which ligand-induced displacement of the ligand binding β-hairpin propagates as a structural change in the membrane proximal domains.

2.4.6 FRET

Based on our normal mode analysis and comparison of the crystal structures, we predict that signaling is caused by a structural change in the receptor dimer. We experimentally tested our prediction of an active conformation by performing FRET measurements on ECFP and EYFP tagged chimeras of wild-type and mutant TNFR1. We tagged TNFR1 such that the intracellular death domain is truncated and the fluorophore is substituted in its place. Placement of the fluorophore immediately downstream of the TM domain without a flexible linker region prevents it from sampling a wide range of geometric configurations so that the distance measured between fluorophores more accurately reflects changes in the extracellular domain propagated through the membrane. While removal of the death domain abolishes the native function of TNFR1 by preventing it from binding cytosolic adapter proteins, it allows us to directly observe how the behaviors of the

intracellular and extracellular domains are coupled, as we have done recently for a related family-member, Death Receptor 5.(43) We measured FRET by acceptor photobleaching where the enhancement in fluorescence by the donor fluorophore after selective photobleaching of the acceptor yields a quantitative measure of the distance between the two fluorophores (Figure 2-5A). We take the FRET efficiency as the theoretical maximum donor enhancement at 100% acceptor bleaching (see Supporting Information).

To determine the active dimeric structure of TNFR1, we measured receptor energy transfer in a constitutively active mutant, R92Q, and compared the energy transfer to the wild type receptor. The TNFR1 R92Q mutant is known to induce mild inflammatory symptoms in patients with TRAPS.(37) Furthermore, it has been shown in vitro that the R92Q mutation causes elevated basal NF-κB activation, while ligand induced NF-κB activity is comparable to wild-type.(88) We observed measurable ligand-independent energy transfer in both wild-type TNFR1 and the R92Q mutant demonstrating clearly that both wild-type and mutant receptors oligomerize within the plasma membrane. We confirmed the dimeric nature of these interactions in both the wild type and R92Q mutant by plotting ECFP vs. EYFP intensity during photobleaching (Figure 2-5B,C). As previously described(89, 90) dimeric donor/acceptor interactions display a linear bleaching profile between lost EYFP intensity and gained ECFP intensity, while the formation of higher order oligomers is revealed as deviation from linearity. Our ECFP vs. EYFP profiles are consistent with dimeric interaction between membrane receptors, and more importantly, the degree of oligomerization is indistinguishable

between wild-type TNFR1 and R92Q. Therefore the constitutive activity observed in the R92Q mutant is the result of a receptor structural change rather than a change in receptor oligomerization.

To determine the structural difference that exists between wild-type TNFR1 and R92Q as propagated through the membrane, FRET efficiency was plotted as a function of EYFP intensity (the EYFP intensity is proportional to total receptor concentration) on a single cell basis (Figure 2-5D,E). The plot of FRET vs. EYFP intensity shows a monotonically increasing curve, which can be fit to a two-parameter saturable binding curve as previously described.(43, 82, 90) From the model fit, we are able to decouple the structural properties of the receptor dimer from its dimerization affinity based on the extracted model parameters, where the $FRET_{max}$ reflects the average distance between the donor and acceptor fluorophores and the K_d provides a measure of their affinity. Interestingly, based on our model fit, R92Q dimerizes with a lower $FRET_{max}$ than the wild-type receptor, suggesting that the average fluorophore separation is greater in the mutant as compared to the wild type receptor (Figure 2-5F). Moreover, R92Q dimerizes with a lower K_d than the wild type receptor, suggesting that the mutant homodimerizes with greater affinity (Figure 2-5G). Though it is unknown whether the change in affinity is due to interactions involving the mutant or due to large scale changes in receptor structure, the combination of higher affinity and a change in cytosolic domain separation in the R92Q mutant may both contribute to its ligand-independent activity. Because of limitations in the maximum attainable transfection levels, there is some degree of uncertainty in the model fits due to the scarcity of

data points in the plateau region at high EYFP intensity. We note that the extent to which our data populate the plateau regions in the scatter plots is similar to previously published studies using the same fitting technique.(90-92) To eliminate any bias resulting from the uneven distribution of data points, we have binned the data and refit the curves (see Supporting Information). While binning slightly diminishes the difference in both $FRET_{max}$ and K_d between wild-type and R92Q, the overall effect is unchanged. Specifically, the R92Q mutation leads to a 27% or 39% reduction in $FRET_{max}$ and a 27% or 55% reduction in K_d taken from the binned data or raw data respectively. We also calculated the average FRET efficiency from cells expressing high levels of EYFP and found that, without depending on a model fit, the R92Q mutation leads to a significant reduction in FRET of 19%, consistent with our conclusion that the mutation causes separation of the cytosolic domains (see Supporting Information).

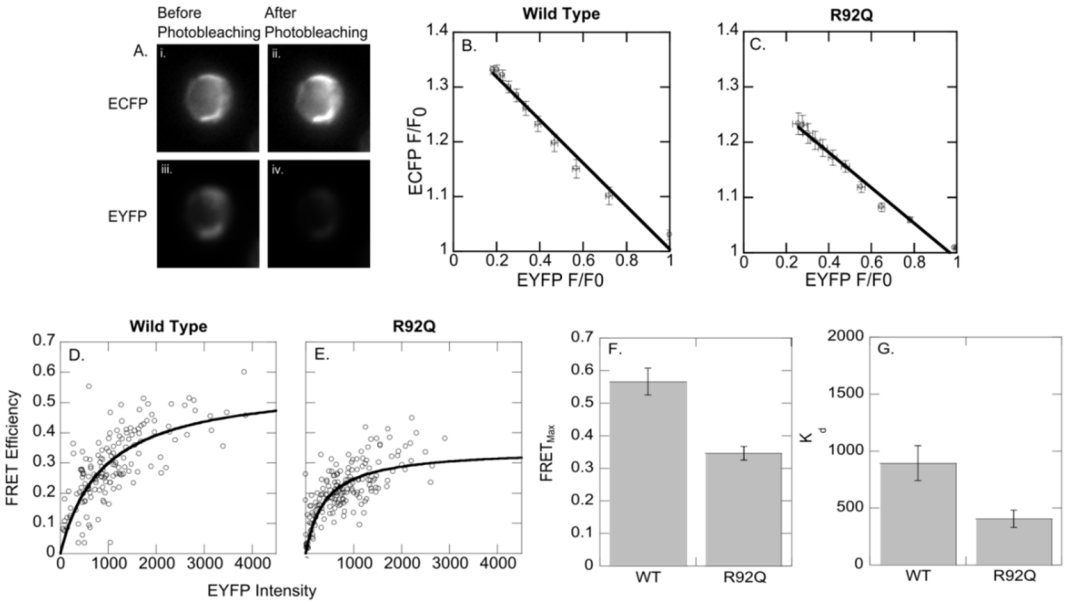

Figure 2-5. FRET analysis of the constitutively active R92Q mutant . Energy transfer was measured by acceptor selective photobleaching. A single cell is shown in the ECFP channel before (A,i) and after (A,ii) photobleaching, and the EYFP channel before (A,iii) and after (A,iv) photobleaching. ECFP was plotted against EYFP during

the photobleach to discern the oligomeric state of the WT (B) and R92Q (C) receptors. FRET efficiencies of individual cells were plotted against EYFP intensity and fit to a two-parameter saturable binding curve for WT (D) and R92Q (E). The model parameters were extracted. $FRET_{max}$ relates to the structure of the receptor dimer (F) and K_d provides a measure of the relative affinities (G). Error bars represent the error of the fit.

Collectively, our FRET results suggest that the TNFR1 R92Q mutation results in an altered structure—an open conformation with increased separation between the cytosolic domains of the receptor dimer. We propose that this open conformation adopted by R92Q is the signal competent configuration and that the same conformational is enforced through ligand induced binding as predicted by our normal mode and crystal structure analysis described above. However, direct measurement of ligand induced changes in FRET is complicated by the formation of ligand/receptor networks. The formation of networks introduces multimeric donor/acceptor combinations, and it is not possible to measure the energy transfer in only the TNFR1 homodimer. While we predict a ligand-induced decrease in dimeric FRET, others have reported a ligand-induced increase in overall FRET, which may reflect the formation of such networks leading to an overall increase in energy transfer.(61) We predict that ligand binding would lead to a separation of the fluorophores in the receptor dimer that is subsumed within the network, resulting in decreased energy transfer. However, despite a reduction in dimeric energy transfer, the clustering of fluorophores due to network formation would increase overall energy transfer measured using steady state techniques (we estimate from the crystal structure that network formation would draw non-dimer

receptors within 30 Å of each other, where the Förster distance of ECFP-EYFP is approximately 49 Å(93)). The net effect of these two competing contributions to FRET complicates the analysis in the presence of ligand. We do expect that ligand-induced networks would manifest as a non-linearity in the ECFP vs. EYFP bleaching profile (Figure 2-5B and 5C) due to the presence of multiple acceptors within the FRET distance of each donor molecule. Fluorescence lifetime imaging and model-based fitting algorithms are better suited for determining dimeric energy transfer in a complex system with many donor-acceptor pairs.

2.5. Discussion

Due to the structural similarity between the crystal structures of the pre-ligand, dimeric TNFR1 and ligand-bound, trimeric TNFR1, a receptor conformational change has not previously been considered as a potential trigger for signal initiation. As a result, the widely accepted model for TNFR1 activation is that ligand binding causes its trimerization, thereby resulting in a reorganization of the cytosolic domains, and that the receptor trimer is the signaling competent architecture, however the precise molecular mechanism of TNFR1 signal initiation at the level of ligand-receptor binding is uncharacterized. Further, the current trimerization model does not account for ligand-independent signaling as in the R92Q mutant or in overexpressed systems nor does it explain the significance of ligand-receptor network formation. We have identified a potential conformational change in the receptor backbone, consistent with ligand binding and reorganization of the cytosolic domains. In this study, we provide evidence that the signaling

competent architecture is the dimer, and that ligand binding and network formation serve to stabilize an active dimeric conformation.

Our results are consistent with our hypothetical model in which ligand binding induces a conformational change in the cytosolic domains and forms organized networks via dimeric receptor interactions. However the precise mechanism through which ligand displaces the ligand binding β-hairpin has not been described. Ligand binding causes TNFR1 to form networks, modeled as a hexagonal lattice as in Figure 2-1C. We generated a dimer of trimers model, the smallest networked subunit (Figure 2-1F), by structural alignment of the 1ncf and 1tnr crystal structures and found that while networks may form without steric interference between dimerization and ligand binding, the resulting structure is not planar with respect to the membrane. The principle axes of adjacent ligands in the dimer of trimers are tilted at an angle of approximately 35º with respect to one another. Expansion of the network beyond two trimer subunits will result in further conflict with the membrane, forming a spiraling structure rather than the flat hexagonal structure, co-planar with the membrane as predicted (see Supporting Information). This conflict is shown schematically in Figure 2-6A (network tilting is shown in two dimensions for clarity). In order for the network to form, the ligand-receptor complex must undergo a structural change so that adjacent trimer subunits are co-planar with each other and with the membrane. We believe this conformational change is consistent with the observed structural difference between the inactive wild type and the constitutively active R92Q mutant in the absence of ligand, and that the conformational change is consistent with the

altered mobility observed in our normal mode analysis (Figure 2-6B). This further suggests that the function of the receptor is dictated not by ligand-induced changes in death domain stoichiometry, as previously thought, but rather by a network stabilized conformational change in the receptor dimer.

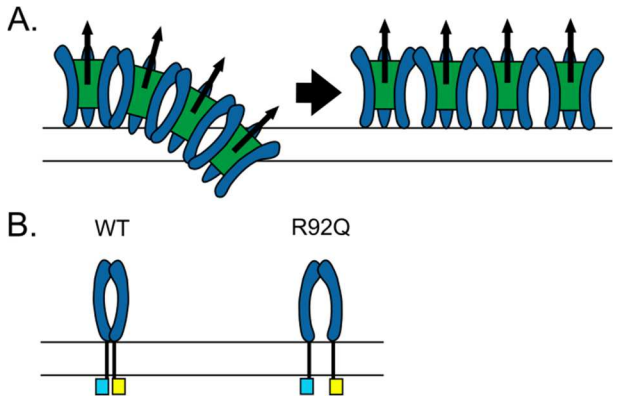

Figure 2-6. Receptor conformational change and network flattening. FRET analysis shows the formation of an altered conformation in the cytosolic domain in the R92Q mutant compared with wild type (A). We propose that the same conformational change is induced by ligand-receptor network formation. The ligand-receptor network, as generated by structural alignment of the 1tnr and 1ncf crystal structures, results in a steric conflict with the would-be membrane. This conflict is illustrated schematically in two dimensions for clarity. Adjacent ligand trimers are tilted at an angle of approximately 35º. To alleviate this steric conflict and grow the ligand-receptor network, a structural change must occur in the receptor dimer to allow the network to become coplanar with the membrane (B).

Normal mode analysis of the dimer of trimers reveals that the essential motions of network flattening can be characterized by just two low-frequency modes (Figure 2-7). It is important to note that the analysis of individual normal modes does not reveal the equal-time correlated motions of protein domains, however individual modes can be useful in roughly describing large-amplitude structural changes in the protein complex. In order to flatten, the ligand trimers must rotate and separate at their membrane proximal end (Figure 2-7A, top), as well as swivel in the plane separating the two ligand trimer structures (Figure 2-

7A, bottom). Figure 2-7A, top and bottom show the dimer of trimers structure prior to any displacement. The flattening motions are described by normal mode 1 and normal mode 3, respectively (Figure 2-7B, top and Figure 2-7B, bottom). Normal mode 2 corresponds to an asymmetric rotation of the dimer through an axis perpendicular to the membrane and does not contribute to flattening. After an arbitrary displacement along normal modes 1 and 3, it is apparent that the dimer of trimers becomes flat with respect to the membrane (Figure 2-7C, top and Figure 2-7C, bottom show the dimer of trimers structure after displacement through modes 1 and 3 respectively).

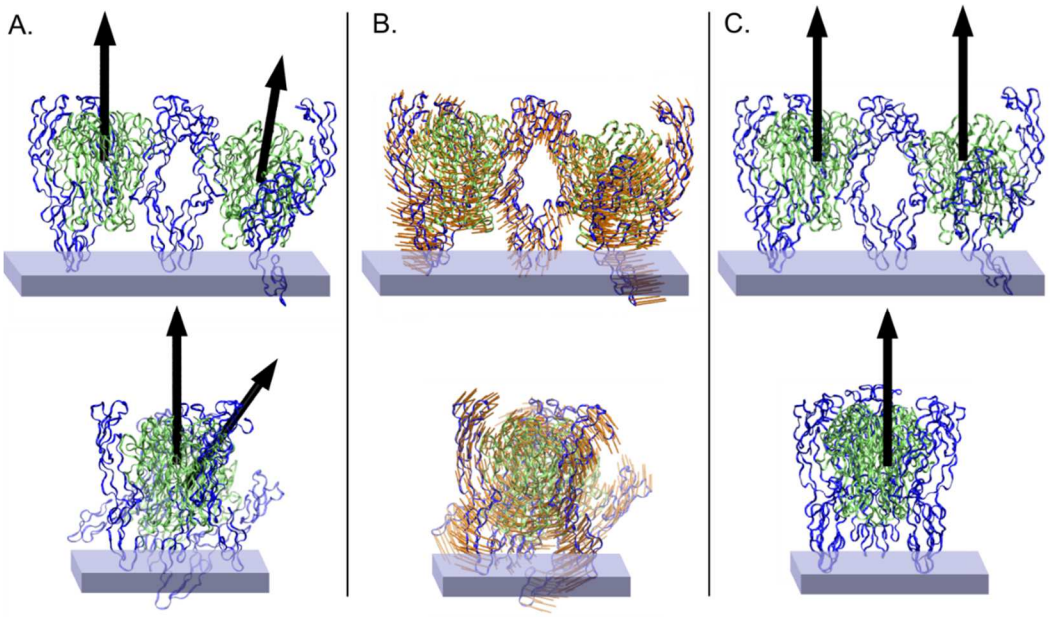

Figure 2-7. The normal modes of the dimer of trimers predict flattening. The dimer of trimers formed by structural alignment of the 1ncf and 1tnr crystal structures is shown from the front (A-C, top) and side-view (A-C, bottom). Both structures are shown prior to any displacement through the normal modes in panel A. Vectors are drawn corresponding to the principal axis of each ligand trimer. Porcupine plots illustrating the collective motions described by modes 1 and 3 are shown (B, top and bottom respectively). The resulting structures after arbitrary displacement through mode 1 and 3 are flattened to permit network extension (C, top and bottom respectively).

Normal mode analysis of the dimer of trimers model shows, as in 1tnr, that mobility is increased in the membrane proximal regions compared to 1ncf (Figure 2-8). Indeed, the membrane proximal domains at Regions v and vii and the ligand binding loop at Region iv become the most mobile regions of the structure (Figure 2-8B, red indicates mobile regions). Therefore, we propose that it is the change in the orientation of the ligand with respect to the principal axis of the receptor, enforced by network formation within the planar membrane, that displaces the mobile ligand-binding β-hairpin about the rigid ligand-binding domain at residues 77-81. We suggest that this conformational change propagates to the membrane proximal region as illustrated in Figure 2-4, thereby resulting in a structural change in the TM and cytosolic domains.

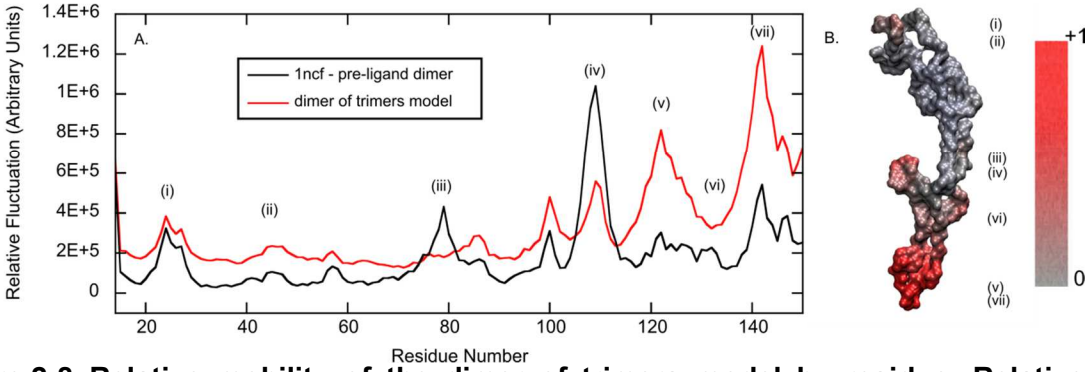

Figure 2-8. Relative mobility of the dimer of trimers model by residue. Relative fluctuations by residue were calculated as in Figure 2-3 for the dimer of trimers model. Residue mobility differs substantially compared to 1ncf (A). The relative fluctuation is shown schematically in (B).

We are the first to show a higher degree of separation in cytosolic domains of a constitutively active, disease-related mutant as compared to the wild type TNFR1. As such we believe that separation of the cytosolic domains of the TNFR1

dimer is consistent with its activation. The mechanism coupling cytosolic domain separation with binding of adaptor proteins has not yet been explored and no structural data exists characterizing the interaction of the TNFR1 death domain with its cytosolic adaptor proteins. However, a crystal structure has been solved revealing homodimeric organization of the TNFR1 death domain.(94) Further studies have shown that the residues involved in homotypic death domain interactions are also responsible for, or overlap with residues responsible for binding to TRADD.(95) Therefore it is conceivable that separation of the TNFR1 cytosolic domains – that is, transition to the active state – causes dissociation of the death domain dimer and allows TRADD to bind to the previously concealed homodimerization/TRADD binding sites. The key residues involved in SODD binding have not been mapped, nor has its structure been solved, therefore we reserve speculation on its function in TNFR1 cytosolic domain separation.

The idea of ligand induced cytosolic domain separation as a signaling mechanism has been previously investigated using FRET in integrin $\alpha_L\beta_2$.(92) Upon ligand binding to their extracellular domains, the alpha and beta subunits of the receptor dimer undergo a conformational change, resulting in “swinging-out” of their cytosolic domains, and this structural change activates the receptor and initiates outside-in signaling, measured by FRET(92) intracellular tyrosine phosphorylation.(96) A similar mechanism has been proposed for the activation of p75 neurotrophin receptor (NTR), a fellow member of the TNFR superfamily. Ligand binding is believed to result in a scissors-like movement in the receptor dimer about a disulfide hinge in the transmembrane region, causing the

extracellular domains to join and the cytosolic domains to separate. This conformational change was observed using FRET and it is believed to expose binding interfaces for downstream signaling factors.(54)

In our proposed model of TNFR1 activation, the signaling competent stoichiometric unit is the dimer. The role of the ligand in mediating the separation of cytosolic domains and transition to the active state is two-fold. In one respect it modifies the intrinsic structural fluctuations in the receptor backbone, allowing it to more readily sample the active conformation. This is supported by our cross-correlation map and suggests that while the TNFR1 dimer is capable of initiating signaling, it is unlikely to do so due to restricted mobility in key domains. While the ligand-independent receptor does not form networks or experience the associated flattening constraint, in certain energetically unfavorable circumstances, it may be able to reach a signaling state as in the R92Q mutant. The ligand serves to mitigate this energetic barrier, allowing the ligand-bound receptor to readily adopt an active conformation. Second, ligand mediates network formation. The ligand receptor network, due to it being necessarily co-planar with the membrane, enforces and stabilizes the altered receptor conformation by displacing the ligand binding domain, which in turn causes a conformational change in the transmembrane and cytosolic domains. Additionally, the network may play a role in concentrating the signal or in stabilizing the dimer. We have shown that the R92Q mutant dimerizes with higher affinity that the wild type, however it is unknown whether this is a consequence of interactions involving the mutant itself or of its adopted active configuration. If the receptor dimer forms with higher affinity in its active state, it

follows that network enforced conformational change would also generate a stronger dimer, amplifying its signaling properties.

Collectively, our results inspire a novel perspective in membrane receptor activation and ligand-receptor network formation. While ligand is known to induce network formation, we have shown that this oligomerization is not enough to explain the signaling event. Rather, by virtue of its formation, the network conspires with the planar membrane to enforce conformational change and receptor activation. Therefore, the relevant signaling event associated with ligand-induced TNFR1 activation involves a conformational change due to collaborative interactions between ligand-receptor, receptor-receptor, and receptor-membrane, which together provide an external force to overcome the energetic barrier between inactive and active states.

2.6. Supplemental Figures

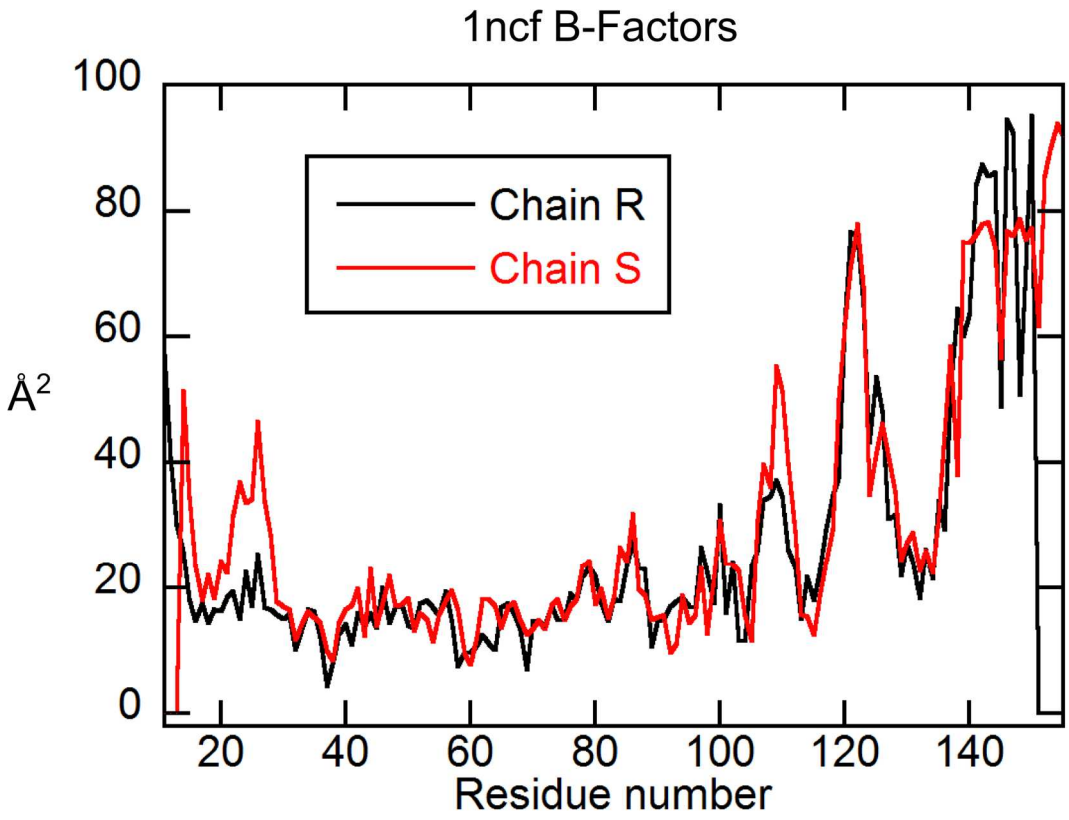

Figure 2-9. Backbone B-factors of chains R (black) and S (red) of the 1ncf crystal structures. B-factors are averaged over the backbone N, C, O, and Cα atoms.

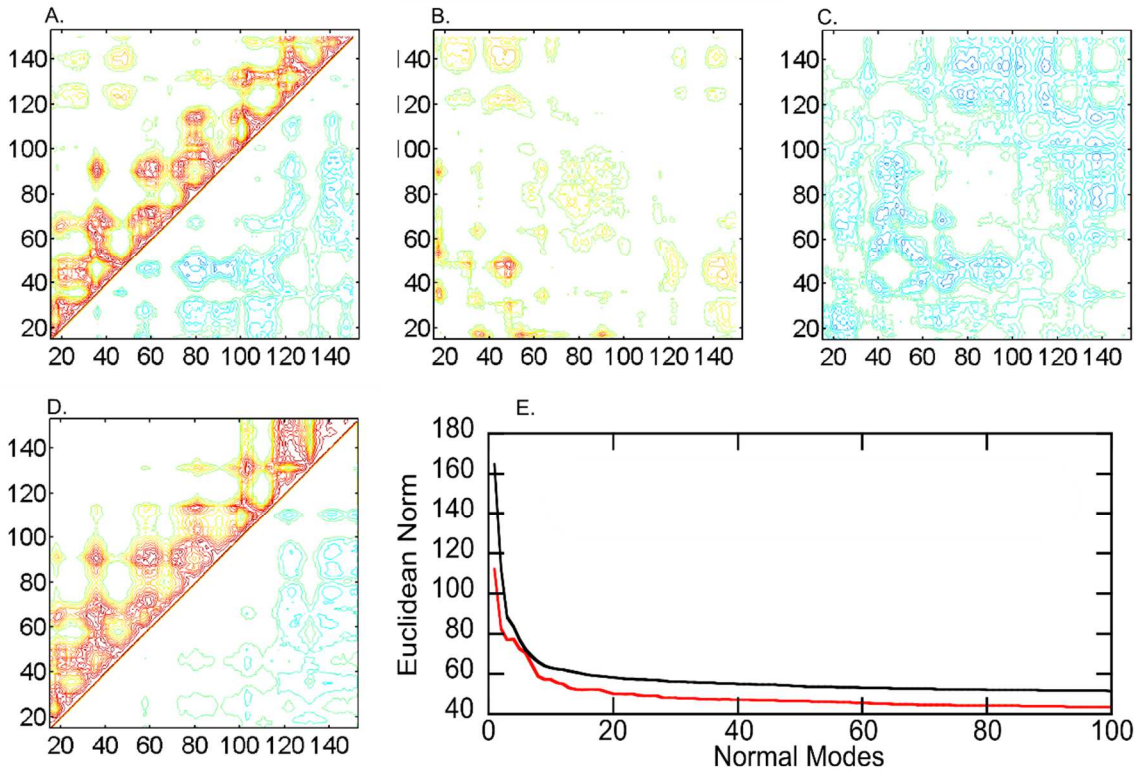

Figure 2-10. Intramolecular cross-correlation maps based on the first 100 modes of the normal mode analysis for chain A or R of the 1ncf (A) and 1tnr (D) crystal structures respectively. Positive correlations are plotted in the upper left and negative correlations in the lower right. Positive (B) and negative (C) intermolecular correlations between residues A and B are plotted for the 1ncf structure. The Euclidean norm is plotted as an estimate of convergence (E).

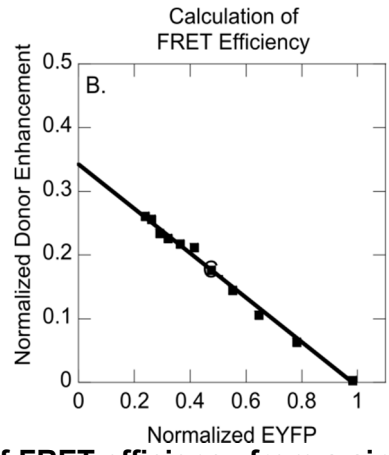

Figure 2-11. Calculation of FRET efficiency from a single cell. The FRET efficiency is taken as the y-intercept of the linear fit.

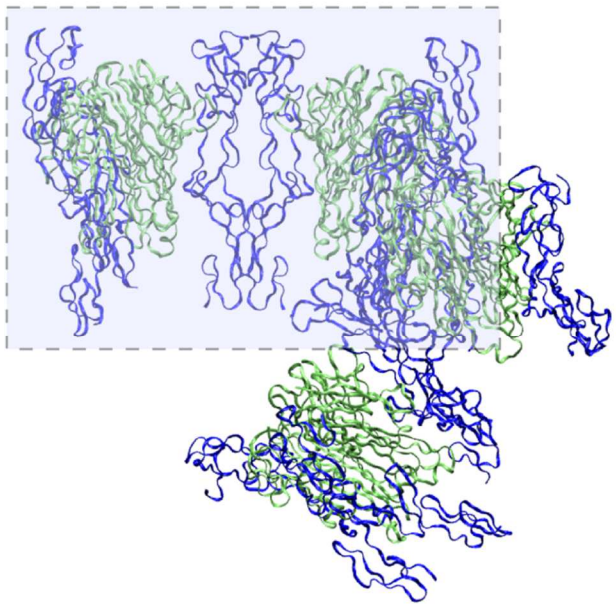

Figure 2-12. Growing the ligand-receptor network to 4 ligand-bound trimer subunits through structural alignment reveals substantial pitch. The dimer of trimers is highlighted.

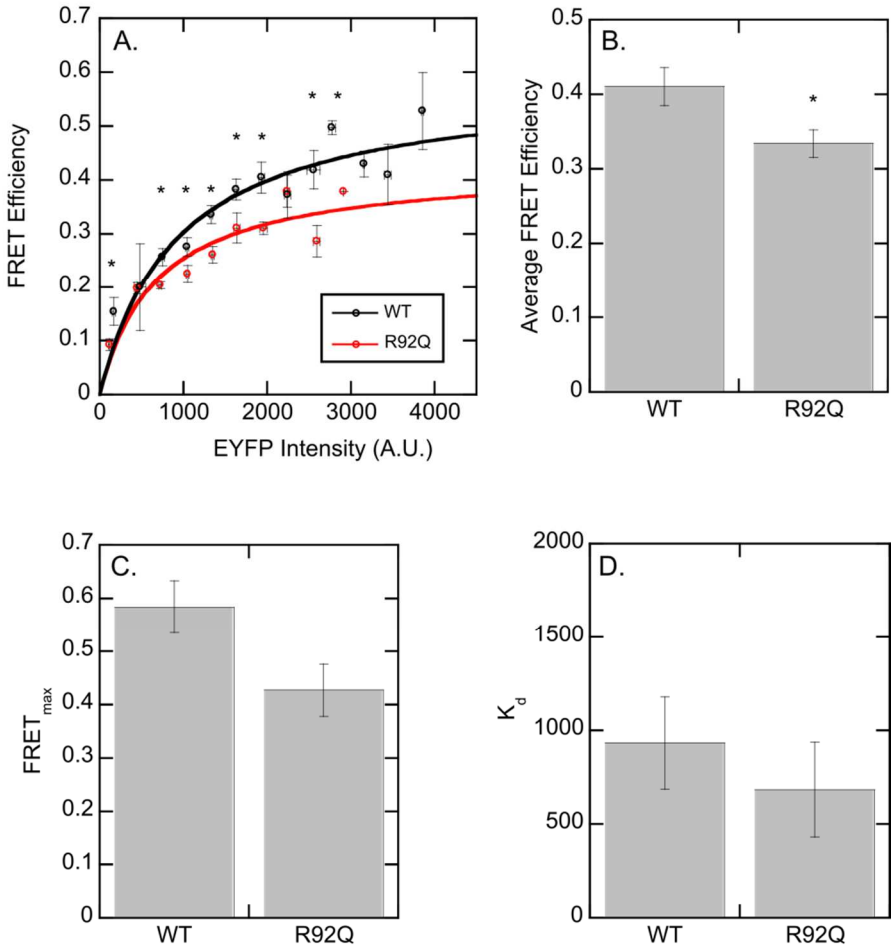

Figure 2-13. Model fitting to the FRET data after binning (A). Data points are denser at intermediate EYFP intensity, and therefore this region has the strongest influence on the curve fit. Binning distributes the data points used for curve fitting evenly to remove this bias. Statistical significance (p-value < 0.05) between equivalent bins in the WT and R92Q measurements is denoted with (*). Average FRET efficiency was calculated for cells expressing high EYFP concentrations (2000 – 3000 A.U.) (B). Calculation of FRET efficiency without model fitting yields the same conclusion – that the R92Q mutation results in an increase in the FRET distance. $FRET_{max}$ and K_d are reported as in the unbinned raw data (C and D respectively).

Chapter 3 – Open and Closed Conformations of the Isolated Transmembrane Domain of Death Receptor 5 Support a New Model of Activation

3.1. Prefatory note

This study expands on my contribution to an earlier published work in the Sachs lab, where a complete description of methods and results can be found (43). The focus of that study was the supramolecular organization of TRAIL/DR5 networks and a key finding was that the long isoform of DR5 (DR5L) forms a disulfide bond in its transmembrane domain upon ligand binding. This disulfide bond reduces the available degrees of freedom of the TM dimer and simplifies the problem of predicting its structure. We ran replica exchange molecular dynamics (REMD) simulations of the disulfide-linked dimer and analyzed the resulting low-energy states for likely dimer conformations. Also notable is the presence of a GxxxG sequence, which is a known dimerization motif (97). Our simulations predicted a right-handed dimer in which the GxxxG motifs were in close contact. The following study starts with this dimer structure and explores the free energy of available conformations as the dimer opens and closes, with the disulfide bond acting as a hinge.

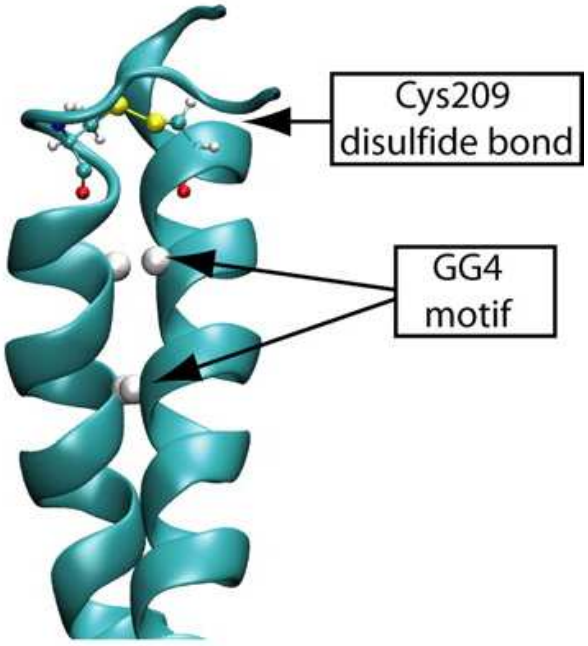

Figure 3-1. REMD predicted structure of the DR5L transmembrane domain. Adapted from Valley et al. (43)

3.2. Summary

It has long been presumed that activation of the apoptosis-initiating Death Receptor 5, as well as other structurally homologous members of the TNF-receptor superfamily, relies on ligand-stabilized trimerization of non-interacting receptor monomers. We and others have proposed an alternate model in which the TNF-receptor *dimer*—which sits at the vertices of a large supramolecular receptor network of ligand-bound receptor trimers—undergoes a closed-to-open transition, propagated through a scissors-like conformational change in a tightly bundled TM domain dimer. Here we have combined electron paramagnetic resonance spectroscopy and potential of mean force calculations on the isolated TM domain

of the long isoform of DR5. The experiments and calculations both independently validate that the opening transition is intrinsic to the physical-character of the TM domain dimer, with a significant energy barrier separating the open and closed states.

3.3. Introduction

Death receptor 5 (DR5) is a member of the tumor necrosis factor receptor (TNFR) superfamily that mediates apoptosis when bound by its cognate ligand, TNF-related apoptosis inducing ligand (TRAIL) (98). Upregulated in cancer cells, DR5 is among the most actively pursued anticancer targets (99). TRAIL binds to preassembled DR5 trimers at their extracellular domains (ECDs), causing the formation of oligomeric ligand-receptor networks that are held together by receptor dimers (43). In the long-isoform of DR5, this dimer is crosslinked via ligand-induced disulfide bond formation between two transmembrane (TM) domain α-helices at Cys-209, and is further stabilized by a GxxxG motif one helix turn downstream (43).

Our recent study of the structurally homologous TNFR1 showed that receptor activation involves a conformational change that propagates from the extracellular domain to the cytosolic domain through a separation (or opening) of the TM domains of the dimer (60). We have therefore hypothesized that the activation of DR5, and indeed all structurally homologous TNF-receptors, involves a scissors-like opening of the TM domain dimer (Figure 3-2Figure 3-1).

Using electron paramagnetic resonance (EPR) spectroscopy, a technique that has been used previously to study TM helix architecture and dynamics (100,

101), and potential of mean force (PMF) calculations (102, 103), the present study addresses the question of whether the isolated disulfide-linked DR5-L TM domain dimer occupies distinct open and closed states (Figure 3-2), and how its dynamic behavior contributes to the free-energy landscape of the opening transition of the full-length receptor.

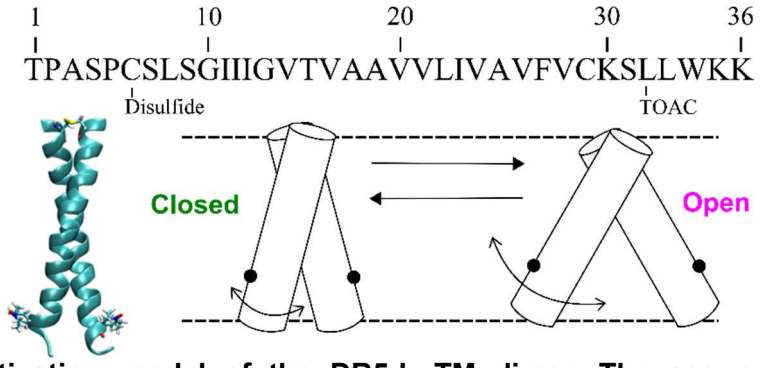

Figure 3-2. Activation model of the DR5-L TM dimer. The sequence (top) and positions of the disulfide bond and TOAC spin label in our previously published model (bottom, left) are shown. We propose an activation model (bottom, right) in which the transmembrane dimer pivots at its disulfide bond to reach an active open conformation.

3.4. Results and Discussion

The DR5-L TM domain was synthesized with TOAC, an amino acid with a nitroxide spin label rigidly fixed to the α-carbon (104), incorporated at position 32 (Figure 3-2), with some minor modification to facilitate EPR measurements. Previous work confirmed that this peptide forms disulfide-linked dimers (e.g. via comparison to 2-ME treated sample) and a negligible population of higher order oligomers (further supported by model fitting of the EPR data below). For peptide work, residues were renumbered such that Thr-204 corresponds to Thr-1, and so on. The cytosolic Cys-29 (which we previously showed does not participate in a disulfide bond in cells) was replaced with serine to prevent the formation of

antiparallel disulfide-linked dimers, and Trp-34 was replaced with tyrosine to prevent intrinsic fluorescence in fluorescence studies (not published). CW dipolar EPR (sensitive only to spin-spin distances less than 25 Å) was used to measure TOAC-TOAC distances within the TM dimers and revealed an ordered Gaussian distribution centered at 16 Å (FWHM = 4 Å), corresponding to a closed state (Figure 3-3A). DEER (sensitive to spin-spin distances from 15 – 60 Å) also detected a short distance consistent with the dipolar EPR data, along with a longer, disordered component (32.9 Å, FWHM = 28 Å) (Figure 3-3B). Together, these measurements indicate the presence of a compact, ordered closed state and a broader, disordered open state. EPR on oriented membranes also indicated two structural states. Global fitting revealed two populations of spin label tilt angles (orientation of the nitroxide principal axis relative to the membrane normal): a narrow conformation (24°, FWHM = 20°), and a disordered conformation (50°, FWHM = 48°) (Figure 3-3C). This bimodal orientational distribution (Figure 3-3C) is remarkably consistent with the bimodal distance distribution (Figure 3-3B).

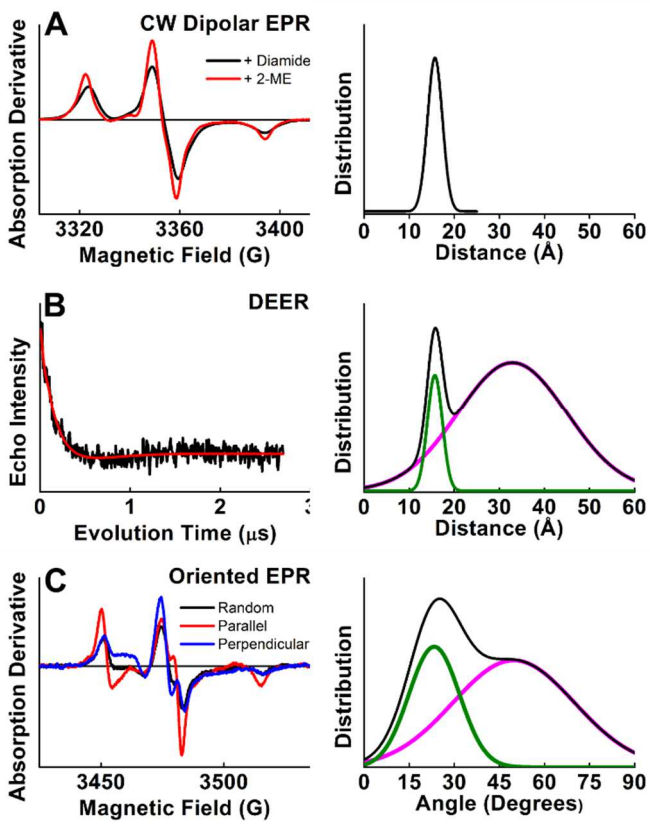

Figure 3-3. EPR spectra (left) of 32-TOAC-DR5 in lipid, and resulting structural distributions (right). (A) CW dipolar EPR spectra (left) of dimer (1 mM diamide) and monomer (1 mM 2-mercaptoethanol). Best fit spin-spin distance distribution was a single Gaussian centered at 16 ± 2 Å (right). (B) DEER waveform (left) of 32-TOAC-DR5 dimer was best fit (right) to a 2-Gaussian distribution. The short distance was constrained to agree with the CW data, since DEER has poor sensitivity for distances less than 20 Å. The long distance distribution is centered at 32.9 Å and is much broader. (C) CW EPR spectra (left) of 32-TOAC-DR5, with the membrane normal oriented parallel (red) and perpendicular (blue) to the field. Simultaneous (global) fitting of these spectra reveals narrow and broad components (right). In B and C, the overall distribution is plotted as black, while the closed and open components are plotted as green and magenta, respectively.

We subsequently conducted a potential of mean force (PMF) calculation (105) using the DR5-L TM dimer starting configuration developed by our group previously (43), embedded in a DMPC bilayer, with the Leu-32/Leu-32 C_α distance ($r_{32\text{-}32}$) as the reaction coordinate. Three calculations were run from independent

starting configurations, each using 50 windows spaced in 0.5° increments, and run for 20 ns at each window (totaling 3μs). Each of the calculations yielded a similar result, and the mean free energy curve (Figure 3-4A) agrees remarkably well with our EPR measurements: a narrow distribution at the closed conformation (~16 Å, Figure 3-4B) separated by an ~3 kcal/mol energy barrier from a broad distribution of accessible open conformations (centered at ~27 Å, Figure 3-4C). The individual PMF plots can be found in Figure 3-5).

In the closed state, the helices are tightly packed at the GxxxG interfacial motif and all the way down the juxtaposed helix faces at residues Ala-18, Leu-22, Ala-25, and Val-26. The tight packing is aided by kinking and twisting of the two helices around their common axis, increasing the interacting surface area. In the open conformations, the Ala-18, Leu-22, Ala-25, and Val-26 pairs are dissociated and, interestingly, the GxxxG motif at Gly-10 and Gly-14 remains tightly packed. The open state energy well is only slightly less favorable than the closed state (by ~2 kcal/mol), and its free energy profile is relatively broad and flat. The increased crossing angle in the open state is facilitated by straightening of the helix kink and is not accommodated by a change in bilayer thickness (Figure 3-7A, B).

The observed change in helix-helix distance (10 Å between the two minima in the PMF) is extremely close to that observed previously in live-cell FRET studies of a constitutively active form of TNFR1 (~8 Å change between states using large fluorescence probes at the cytosolic domains) (60). The change observed in the EPR data (17 Å) may be an overestimate because the measurement is made between TOAC spin labels that likely protrude from the two helices, depending on

rotational orientation. These results collectively show that activation of these receptors requires a small, but clearly significant conformational opening of the TM domains. One important note is that our EPR experiments recapitulate the equilibrium distribution of the two states despite there being no driving force to traverse the barrier between them (~3 kcal/mol in the closed-to-open transition and ~1 kcal/mol in the open-to-closed transition, Figure 3-4). We do not interpret the results to mean that the dimer necessarily traverses these barriers at 4° C. Rather, there likely exist multiple reaction paths for dimerization of the abstracted TM domains. Finally, in the context of the full-length receptor, how the ligand induces a conformational change capable of overcoming the closed-to-open barrier remains an important question.

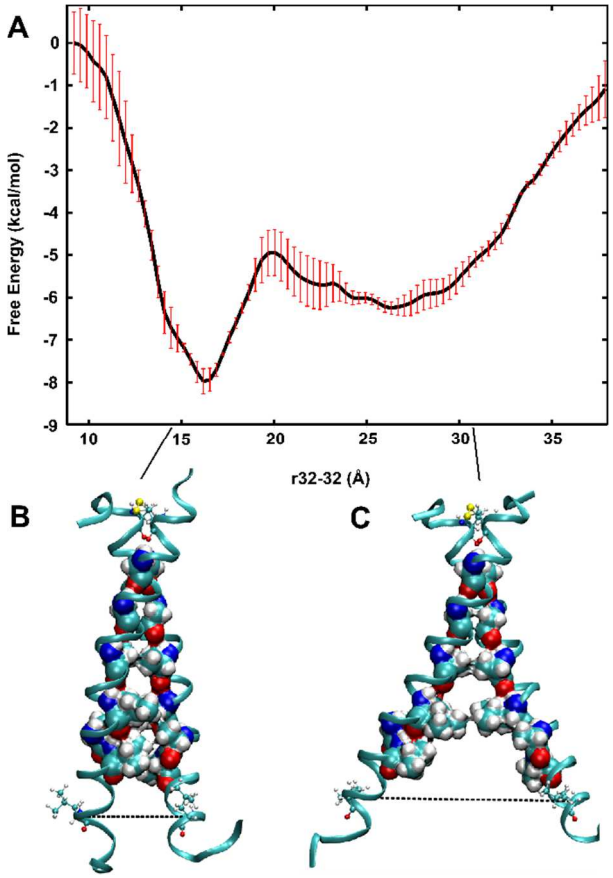

Figure 3-4. PMF calculation of the DR5 TM domain dimer along the Leu-32/Leu-32 distance reaction coordinate. The PMF calculation reveals a narrow closed state and a broader open state separated by a free energy barrier.

Whether the observed structural transition in the TM domain dimer of the long-isoform of DR5 is a ubiquitous conformational switch that acts over the entire TNFR superfamily remains unknown. Vilar et al. first proposed a similar scissors-model for activation of p75 neurotrophin receptor, which has a cysteine at the center of its TM helix (54). The short isoform of DR5 lacks a TM domain cysteine, but does form non-covalent dimers in cells, with likely TM domain dimer contacts (43). Among the other closely related and structurally homologous members of the TNFR superfamily, TNFR1 contains a cysteine at the center of the TM domain, but lacks any discernible small residue motifs (e.g. GxxxG). TNFR2 lacks a TM

cysteine on the extracellular side, but does have a GxxxG motif positioned similarly to that of DR5. On the other hand, Death Receptor 4, whose functional distinction from DR5 has remained somewhat elusive, lacks both a cysteine and any recognizable small-residue hydrophobic motif.

In summary, we have extended recent findings that point to the TM domain of DR5 as an essential structural component in the conformational change associated with activation. Our findings that the DR5-L TM domain occupies distinct open and closed states, separated by a substantial energy barrier, points the way to further studies across the TNF-receptor superfamily.

3.5. Supplemental Methods

3.5.1 EPR sample preparation

For CW dipolar EPR measurements (Figure 3-3A), 32-TOAC-DR5 was reconstituted at 0.4 mM in DPC buffer (15 mM dodecyl phosphocholine, 50 mM phosphate buffer, pH 8.1), with 1 mM diamide or 1 mM 2-mercaptoethanol to maximize or eliminate spin-spin interactions, respectively. This environment was selected because prior simulation studies suggested that the hydrophobic length of DR5 closely matches the DPC micelle diameter, and this would favor the formation of the predicted closed state. The open state would be undetectable using CW dipolar EPR. Furthermore, DPC micelles produced the non-interacting monomeric spectrum under reducing conditions needed to interpret the disulfide-bonded dimer spectrum. DR5 stock in trifluoroethanol (TFE) was dried under N2 gas and stored under vacuum overnight to remove residual solvent. The next day, DPC buffer was added to the sample and thoroughly vortexed. Samples with

added diamide were incubated overnight at 4 °C to allow for disulfide bond formation, while samples with added 2-mercaptoethanol were measured by EPR spectroscopy after 10 minutes to prevent complete spin label reduction.

For DEER experiments, 32-TOAC DR5-peptide was reconstituted at 700 lipids/DR5 (mol/mol) into 2.5:2.5:1 DMPC/POPC/DHPC (mol/mol) bicelles in 50 mM HEPES, 1 mM diamide, pH 7.0 (106). Bicelles were used to reduce background effects arising from the distribution of protein within the sample. Bicelles allow for a more homogenous (3D) protein distribution, as opposed to lipid vesicles which tend to produce sub-3D distributions. Briefly, lipid stocks in chloroform and DR5 stock in TFE were combined, dried under N2 gas, and then stored overnight in a vacuum desiccator. The next day, the lipid/DR5 film was resuspended in HEPES/diamide buffer by thorough vortexing and water bath sonication. The reconstituted bicelle sample was then incubated overnight at 4 °C to allow for disulfide bond formation.

For oriented EPR measurements, 32-TOAC-DR5 was reconstituted at 100 lipids/DR5 (mol/mol) into 4:1 DOPC/DOPE (mol/mol) lipid bilayers (107). This oriented bilayer system is well-established for protein orientation studies. Briefly, lipid stocks in chloroform and DR5 stock in TFE were combined, dried under N2 gas, and dissolved in a solution of 99:1 methanol/ddH2O (vol/vol). The sample was deposited onto an 8x10 mm glass cover slip, and stored under vacuum overnight to remove solvent. The next day, the sample was transferred into a sealed glass desiccator containing saturated ammonium phosphate solution, and incubated just above the liquid surface at 42°C for 24 hours. Following this rehydration, a second

cover slip was placed atop the sample. The sample was gently compressed, and sealed in Parafilm.

3.5.2 EPR Spectroscopy:

Conventional (continuous wave, CW) EPR spectra were acquired at X-band (9.5 GHz) with a Bruker EleXsys E500 spectrometer equipped with the ER 4122 SHQ (CW dipolar EPR) or TE 4101 OR (oriented EPR) resonator. Temperature was maintained at -73 °C (CW dipolar EPR) or 23 °C (oriented EPR) with a quartz dewar insert and a nitrogen gas flow temperature controller. EPR spectra were acquired with 2 mW (dipolar EPR) or 5 mW (oriented EPR) microwave power, 100 kHz modulation frequency, 3 G modulation amplitude, and 120 G sweep width. For CW dipolar EPR, the sample was pipetted into a glass capillary and supported by a sample holder, while for oriented EPR, the sample on glass cover slip was attached to a flat cell, and rotated within the resonator to align the membrane normal parallel and perpendicular to the field. All EPR spectra were baseline-corrected and then normalized to the double integral.

Spectral simulations and least-squares fits to determine CW dipolar spin-spin distance and probe orientation were performed as described previously (108). In all cases, data were fit to a model corresponding to a sum of Gaussian distributions (of distance or orientation). The number of components was increased until no further improvement in the fit was achieved. Analysis of distance distribution from CW dipolar EPR using Tikhonov regularization gave results similar to those using the Gaussian analysis.

4-pulse DEER (109) was performed at Q-band and 65 K on a Bruker EleXsys E580 spectrometer equipped with a SuperQFT-u bridge and an ER 5107D2 resonator. The decay was analyzed using DEERAnalysis2011 (110), with the raw data truncated by 500 ns to remove a small artifact introduced by observer/pump pulse excitation overlap (111), and then background-corrected assuming a homogenous 2D model. The resulting waveform was fit to a two Gaussian model, where one component was constrained to match the mean distance and full-width half-maximum (FWHM) determined by CW dipolar EPR, while the remaining parameters (mean distance and FWHM of the second component, populations of both components) were varied. As with CW dipolar EPR, Tikhonov regularization yielded a distance distribution to that obtained by Gaussian analysis.

3.5.3 PMF calculation and molecular dynamics

To further characterize the observed open and closed TM dimer structures, we conducted molecular dynamics (MD) simulations and calculated a potential of mean force (PMF) using the Leu-32/Leu-32 Cα distance as a reaction coordinate. A starting structure of the DR5L transmembrane homodimer was previously generated using replica exchange molecular dynamics (43). Residues are renumbered such that Thr-204 in the full length protein corresponds to Thr-1 in our synthetic peptide, and so on. The starting configuration was rotated through the Cys-6 disulfide dihedral angle to generate starting configurations for 50 windows of the PMF calculation, varying by 0.5° each. This transformation was chosen to

avoid placing stress on the disulfide bond. The reaction coordinate was taken as the distance between the Cα atoms of Leu-32 to correlate with measured distances from the EPR experiments. These distances varied from 9.48 – 36.74 Å, spaced by roughly 0.6 Å. A 2 kcal/mol/Å2 harmonic bond was applied using the NAMD Colvars module to restrain the reaction coordinate at all stages of simulation. Each dimer configuration was inserted into an all-atom, 128 lipid DMPC bilayer using CHARMM-GUI, and solvated with TIP3 water at ~50:1 water:lipid ratio (112).

NPT ensemble simulations were performed using the CHARMM 36 parameters. Constant temperature (303 K) and pressure (1 atm) were maintained using the Langevin piston and Nosé-Hoover algorithms, respectively. Electrostatics were calculated using the particle mesh Ewald method with a 1.5 Å grid spacing and 4th order interpolation. Lennard-Jones interactions were cutoff at 10 Å. Each window was minimized using NAMD 2.8 for 1000 steps, then equilibrated with Cα harmonic constraints of 1, 0.1, and 0.01 Kcal/mol/Å2 for 2 ns at each stage with a 2 fs time step. Equilibrated systems were simulated unrestrained (except for the harmonic bond restraining the reaction coordinate) for 24 ns, with the final 20 ns used in the PMF calculation. The PMF was calculated at 300K with 100 bins using the weighted histogram analysis method (WHAM) algorithm developed by Grossfield (105). The simulations were performed in triplicate from randomly seeded velocities and the WHAM calculations were performed for each. The PMFs were shifted to equalize the mean free energies, then the mean and standard error of the 3 curves were plotted. PMFs of independent simulations are plotted in Figure 3-5. Error analysis for each individual

run was conducted using the integrated Monte Carlo bootstrapping code, with a decorrelation time of 0.24 ns, as calculated for Cα atoms using Loos (81).

Helix kink angle was calculated for both chains between the principal axes of residues 6-20 and 22-32 over all simulation time from the three replicated systems, and reported in Figure 3-7A. The electron density profile was calculated for all atoms on centered trajectories from each of the three replicated systems, and the mean reported in Figure 3-7B. Both calculations were performed using Loos (81) on trajectories from windows 15 and 34, in which the r32-r32 bond distance was restrained to the minima of the closed and open states respectively.

3.6. Supplemental Figures

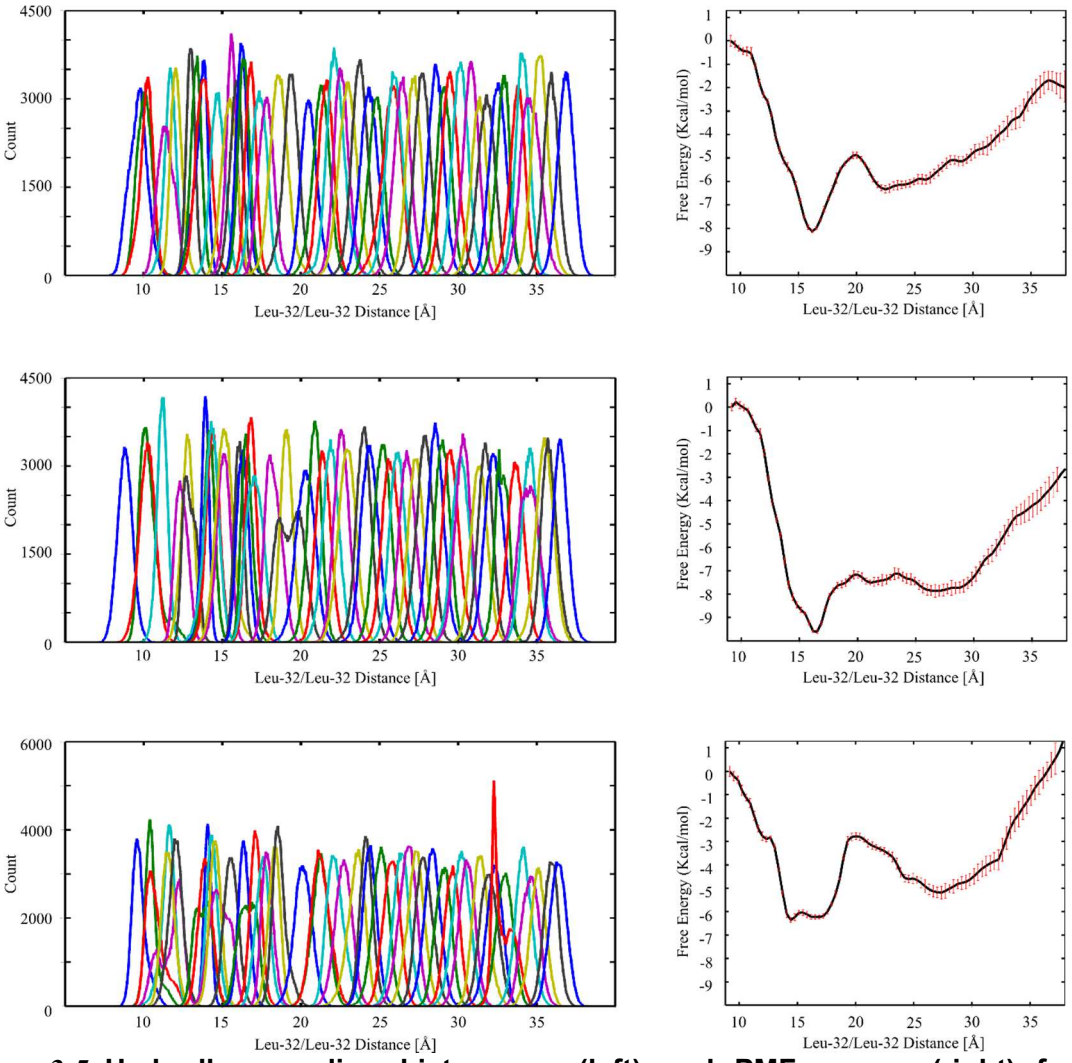

Figure 3-5. Umbrella sampling histograms (left) and PMF curves (right) for 3 independent simulations.

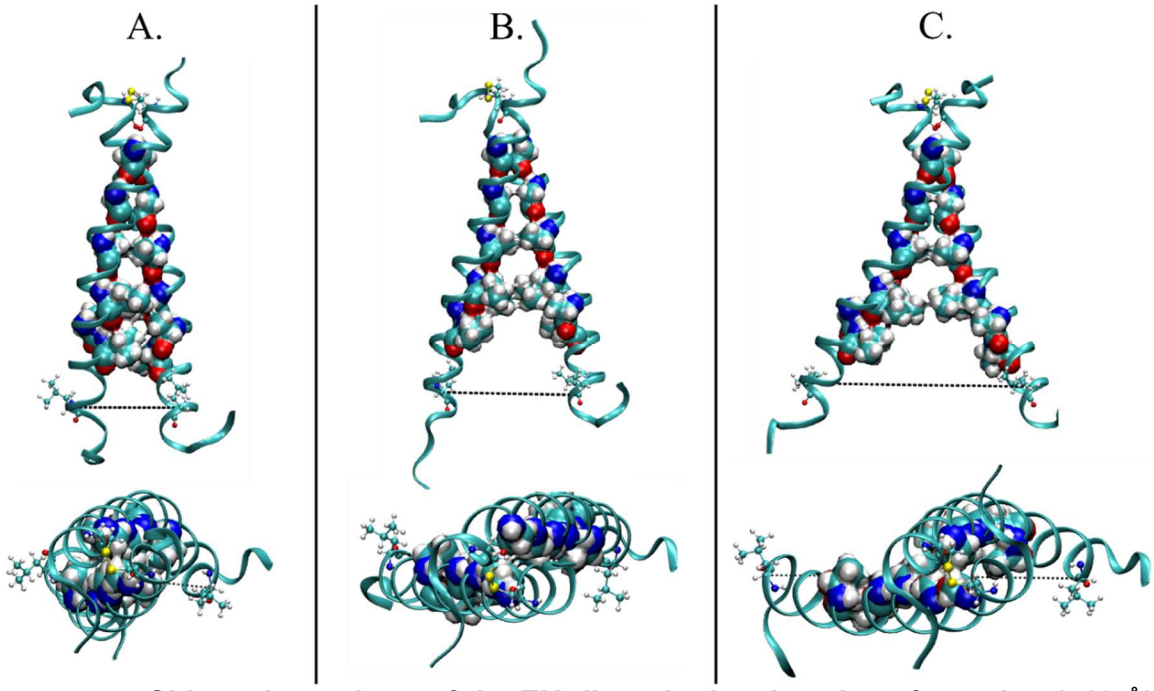

Figure 3-6. Side and top views of the TM dimer in the closed conformation (~16 Å) (A), at the local energy barrier (~20 Å) (B), and in the open conformation (~30 Å) (C).

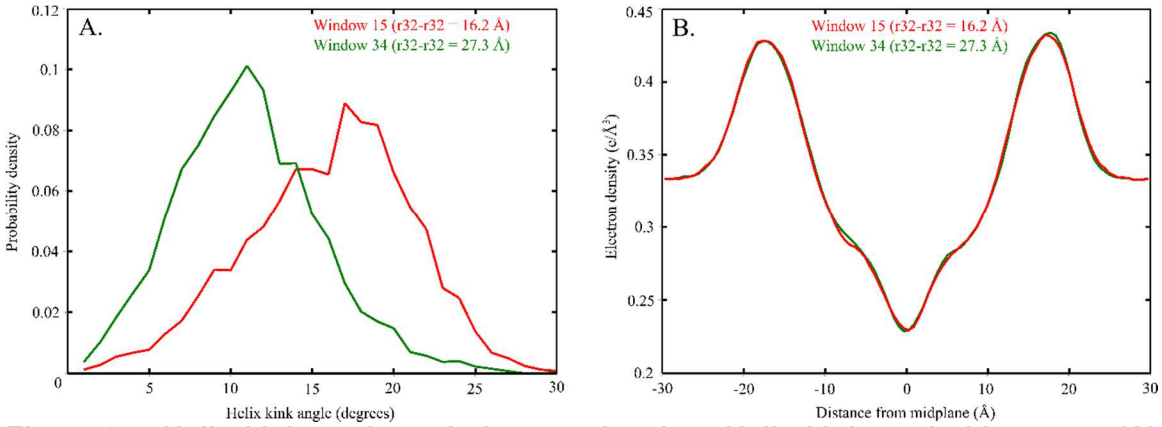

Figure 3-7. Helix kink angle and electron density. Helix kink angle histogram (A) and electron density (B) calculated over all three replicated simulations. TM dimer opening is accommodated by straightening of the helix kink and not a change in bilayer thickness.

Chapter 4 – Death Receptor 5 Networks Require Membrane Cholesterol for Proper Structure and Function

4.1. Summary

Death receptor 5 (DR5) is an apoptosis-inducing member of the tumor necrosis factor superfamily whose activity has been linked to lipid rafts. Upon ligand binding, DR5 forms large clusters within the plasma membrane that have often been assumed to be manifestations of raft co-localization. However, we have recently shown that DR5 clusters are more than just randomly aggregated receptors. Instead, they are highly structured networks held together by receptor dimers. These dimers are stabilized by specific transmembrane helix-helix interactions, including a disulfide bond in the long-isoform of the receptor. The complex relationship between DR5 network formation, transmembrane helix dimerization, raft localization and receptor activity has not been established. It is unknown whether the membrane itself plays an active role in driving DR5 transmembrane helix interactions or in the formation of the networks. We show that cholesterol depletion in cells does not inhibit the formation of DR5 networks. However, the networks that form in cholesterol depleted cells fail to induce caspase cleavage. These results suggest a potential structural difference between active and inactive networks. As evidence, we show that cholesterol is necessary for covalent dimerization of DR5 transmembrane domains. Molecular simulations suggest that dimerization is facilitated by increased helicity and deeper partitioning of Cys209 in a thicker bilayer.

4.2. Introduction

Death receptor 5 (DR5) is an apoptosis-inducing member of the tumor necrosis factor (TNF) receptor superfamily that is activated by TNF-related apoptosis-inducing ligand (TRAIL) or other agonists (113-117). The TRAIL-DR5 signaling pathway is of great therapeutic interest, as exogenous TRAIL prevents tumor growth and, in contrast to other apoptosis-inducing ligands such as FasL, does not exhibit systemic cytotoxicity (118). Thus, DR5 is widely regarded as a potential target in the treatment of cancer (45, 46, 119, 120) with a number of its ligands, including recombinant human TRAIL and antibody agonists (as we will study here), currently in clinical trials (121-126) (see also clinicaltrials.gov). However, TRAIL resistance has proven to be a challenging barrier to the success of DR5-based cancer therapies (51, 52). Thus, continued efforts to understand the complex events involved in DR5 signal propagation, including the initiating events at the membrane, will be useful for understanding therapeutics currently in clinical trials as well as discovering novel DR5-targeted therapeutics.

TRAIL- and agonist-induced apoptosis is initiated by the formation of large (~300-500 nm diameter) DR5 receptor networks in the plasma membrane (43, 63, 127, 128). We have shown that these networks are structured lattices, modeled by us and others as trimeric ligand-receptor complexes held together by dimeric receptor junctions (one monomer from each pair of ligand-receptor complexes) (43, 56, 60-62). Ligand induced receptor dimerization is consistent with crystallographic and functional evidence showing that both intracellular protein

domains and downstream proteins form stable and functional dimeric complexes (62, 129-133). We also showed that the dimeric junctions of DR5 networks are stabilized through interactions between amino-acids in the transmembrane helices, which form tight dimeric bundles in the membrane (43, 53). In the long-isoform of DR5, a disulfide bond forms between TM helices upon activation. Although the short-isoform lacks the disulfide bond, both the long and short isoforms contain the well-established GxxxG TM helix interaction motif, which allows for tight packing at the interface of the two monomeric helices (97, 134).

We have also recently suggested that the receptor dimer of TNFR1 (a structurally homologous member of the same superfamily as DR5), undergoes a conformational transition upon activation (60). This is a very different model than what has previously been proposed for TNF-Receptor activation. In earlier models, activation was thought to involve receptor trimerization and a stoichiometric change in the cytosolic domain that required no conformational changes (i.e. receptor backbone rearrangements) (8, 59). Our molecular calculations, on the other hand, support a model in which signal initiation is a consequence of the mechanical strain placed on the receptors as the network grows. More specifically, we have suggested that the extracellular domain of the receptor dimer pivots outwards on network formation, and that as a consequence the transmembrane dimer opens like scissors (closed in the inactive state, open in the active state) (53, 60). This model of activation has been supported by several recent studies on TNFR1 (76, 135, 136).

Given that ligand-induced dimeric interactions of DR5 occur in part via transmembrane residues, it stands to reason that the membrane itself may play an active role in driving the dimeric interactions that promote network-formation. Cholesterol-rich microdomains in the plasma membrane, often referred to as lipid rafts, play an active role in signal transduction in a number of pathways (137-139) including several that involve members of the TNFR superfamily. Ligand-bound TNFR1 localizes to rafts, and recruits downstream signaling proteins (140, 141). The death receptor Fas has been shown to localize to rafts in a ligand-dependent manner (142), though others have observed ligand-independent raft localization (143). In DR5, Song et al. showed that caspase-8 cleavage in TRAIL-sensitive cells could be inhibited by treatment with methyl-β-cyclodextrin (MβCD) (144). Multiple other studies have shown that DR5 function correlates with its migration into lipid rafts (144-148). However, it is unknown whether localization within cholesterol-rich lipid microdomains is associated with receptor oligomeric structure, i.e. DR5 dimerization and network-formation.

Here, we find that the extent of agonist-induced DR5 clustering is not diminished by cholesterol-depletion. However, cholesterol depletion greatly reduced the ability of DR5 to initiate caspase-dependent apoptosis. We attribute this to the formation of non-functional ligand-receptor networks that differ from functional networks by a reduction in the population of constituent disulfide-linked DR5 dimers. Collectively, these results offer the first evidence that membrane heterogeneity plays a central role in dictating the structural details and functional activity of DR5 networks. These results further support a model in which DR5

networks have a specific structure, and that lipid rafts do not simply corral high local concentrations of receptors, but play an essential role in driving ligand-receptor network architecture.

4.3. Materials and Methods

4.3.1 Cell culture and reagents

Jurkat cells were cultured in RPMI-1640 media (HyClone) supplemented with 10% FBS, 4mM L-glutamine, penicillin and streptomycin and maintained between 10^5 and 10^6 per mL at 37˚C and 5% CO2 in a water-jacketed incubator. DR5 antibody agonist (mAb631), and fluorescent secondary antibody (NL557) were purchased from R&D Systems. DR5 antibody for Western blots was purchased from Cell Signaling Technologies.

4.3.2 Detergent resistant membrane extraction

Detergent resistant membrane (DRM) and detergent soluble membrane (DSM) fractions were isolated as previously described (144, 149, 150). Briefly, Jurkat cells (10^8 cells) were treated with DR5 agonist or control, resuspended in 550 µl TNE buffer (150mM NaCl, 2mM EDTA in 50mM Tris-HCl, pH 7.4) and homogenized 20 times using a 25 gauge needle. Homogenate (500 µl) was mixed with an equal volume of 2% Triton X-100 in TNE buffer supplemented with protease inhibitors (yielding a 1% Triton X-100 final concentration) and lysis proceeded for 30 minutes on ice. Samples were centrifuged at 10,000g for 5 minutes at 4˚C, and post-nuclear supernatants (1 ml) were mixed with 2ml of 56% sucrose, transferred to a SW41 ultracentrifuge tube, and overlaid with 5ml of 35% sucrose and 5ml of 5% sucrose. All sucrose solutions were prepared in TNE buffer

(150). Step gradients were centrifuged at 39,800 rpm (271,000g) at 4˚C for 18 hours using a SW41Ti rotor centrifuge. Gradients were fractionated into 9 fractions of equal volume using a Gradient Station (BioComp Instruments). Protein content in each fraction was measured by BCA assay (Pierce) and compared to a BSA standard curve. Cholesterol content in each fraction was measured using Amplex Red cholesterol assay (Invitrogen Life Technologies). DR5 migration into DRM fractions was analyzed by TCA precipitation and Western blot analysis, using equal volumes of each fraction. Results are from 3 independent experiments.

4.3.3 Caspase-8 activity

Caspase-8 activity was measured as previously described (43). Jurkat cells were treated with a DR5-specific antibody agonist at 1 μg/ml for 4 hours at 37˚C. Caspase activity was measured using CaspGLOW Red Active Caspase 8 staining kit (BioVision) according to manufacturer instructions. Fluorescent labeled active caspase-8 was detected by flow cytometry (FACSCalibur) over 50,000 cells. Data was analyzed using FlowJo software (Tree Star, Inc.), where identical gating schemes were used to determine the percentage of caspase-8 active cells.

4.3.4 Cholesterol extraction

To extract membrane cholesterol, Jurkat cells were washed in PBS and resuspended in serum-free media (RPMI-1640). Cells were treated with 5mM methyl-beta-cyclodextrin in serum-free RPMI for 30 minutes at 37˚C, then gently washed with PBS before stimulation with agonist.

4.3.5 Western blotting

Jurkat cells were washed with PBS and treated with DR5-specific antibody agonist for 1 hour in PBS. In cross-linking experiments, cells were then treated with 1 mM of the amine-reactive membrane-impermeant crosslinker BS3 (Pierce) for 30 minutes at room temperature, then quenched with 20 mM Tris-HCl (pH 7.5) for 15 minutes at room temperature. Cells were pelleted by centrifugation and lysed in RIPA buffer (50mM Tris-HCl pH 7.5, 150 mM NaCl, 0.5% Sodium deoxycholate, 0.1% SDS, 1% NP-40) supplemented with protease inhibitors and 10 mM iodoacetamide for 1-2 hours at 4˚C. Total protein concentration of lysates was determined by BCA assay (Pierce) and equal amounts of total protein (~80ug) were mixed with 4x NuPAGE sample buffer (in the absence of reducing agents), boiled for 10 minutes, and loaded on 4-12% Bis-Tris SDS-PAGE gel (Invitrogen). Proteins were transferred to nitrocellulose membrane and probed using an antibody against DR5 (D4E9, Cell Signaling) and anti-rabbit HRP-conjugated secondary antibody (GE Amersham), and detected using ECL Plus (GE Amersham).

4.3.6 Confocal imaging and analysis

Jurkat cells were untreated or treated with 5mM MβCD to deplete cholesterol as described above. Cell washes in subsequent steps were performed by centrifuging at 10g and gently resuspending in ice-cold PBS with 1% FBS. Cells were washed once and treated with mAb631 agonist at 5 μg/mL in PBS with 1% FBS for 30 minutes on ice. DR5 was removed by washing twice, and cells were

resuspended with 5 μg/mL NorthernLights557 in PBS with 1% FBS, then tumbled for 30 minutes at 4C. Cells were then washed twice, resuspended, and plated on poly-lysine coated 35 mm glass-bottom culture dishes (MatTek Corporation) for imaging. Cells were allowed to settle before taking images.

Cells were imaged using an Olympus IX82 inverted microscope equipped with a FluoView FV1000 laser scanning confocal head with 543 nm laser excitation and 555-655 nm emission using a 100x (1.3NA) oil immersion objective lens. All images were acquired at the same laser intensity and resolution (1600x1600 pixel, 0.079 um/pixel edge).

Images were analyzed using MATLAB. Each image, containing 10–30 cells was first smoothed using a low-pass 2D finite impulse response filter with a Gaussian window. Background intensity was subtracted for each image by selecting a region of the field containing no cells. Each cell border was selected manually from the light field image, and these points fit to an ellipse. A 30 pixel shell along this ellipse was isolated, avoiding the inclusion of any potential fluorescence in the cytoplasm (some cells showed limited internalized label). Angular intensity was then determined along the shell in 1° bins. The peak positions were determined using the MATLAB ‘findpeaks’ command on an ideal low-pass filtered angular integration trace. The peak locations were used as parameters to fit the raw angular integration trace to a 1D mixed Gaussian distribution, which solved for the maximum intensity and standard deviation of each peak.

4.3.7 Replica exchange molecular dynamics of the long isoform DR5 transmembrane domain

All-atom Replica Exchange Molecular Dynamics (REMD) was run using the MMTSB toolset (151). DR5 is expressed as both long and short isoforms (DR5-S and DR5-L), where the long isoform is able to form disulfide-linked dimers, while the short isoform is not. We used DR5-L here to expand on our finding that disulfide bonding in DR5 depends on membrane cholesterol. The starting structure of the DR5-L transmembrane (TM) domain was an ideal helix using residues 200-239 (SSPGTPASPCSLSGIIIGVTVAAVVLIVAVFVCKSLLWKK). The single transmembrane helix was duplicated to generate a dimer and the two segments were started ~8 Å from each other. Simulations used the CHARMM 22 parameters(152, 153) with CMAP correction(154) and the SHAKE algorithm (155). The protein was centered in an implicit bilayer, modeled using the Generalized Born with simple switching function (156, 157). The hydrophobic thickness was set to 32 and 40 Å to model non-raft and raft domains, respectively, and the switching length was set to 0.6 Å. 16 replicates were run from 4 independent starting configurations at 300K – 600K using the Nosé-Hoover method to control the temperature(158). Each replicate was run for 10 ns (total of 640 ns for the 4 sets of 16 replicates) using a 2 fs time step. Replica exchange was attempted every 1000 steps with a success rate of ~20%. Structures from the 300K window were used for analysis.

4.4. Results

4.4.1 DR5 signal transduction in response to agonistic antibody is raft-dependent

TRAIL induction causes DR5 to migrate into cholesterol-rich, detergent resistant membrane (DRM) fractions and when the membrane is cholesterol-depleted by MβCD treatment, DR5 signaling via caspase-8 activation is inhibited (144). This study uses the agonistic antibody, mAb631 in lieu of TRAIL to trigger DR5 signaling. Thus we first determined that the effects of mAb631 and TRAIL induction of DR5 with respect to its raft/non-raft behavior are consistent. Jurkat cells were treated with agonistic antibody, lysed, and separated by sucrose gradient ultracentrifugation as described in Materials and Methods. Activation by agonistic antibody causes DR5 to relocate from high density fractions to lower density, cholesterol rich fractions (Figure 4-6), consistent with DR5 behavior in response to TRAIL. We then investigated whether agonist-induced, DR5 dependent caspase-8 activation depends on DR5 migration to DRM fractions. We treated cells with MβCD to deplete membrane cholesterol, thereby preventing DR5 relocation to cholesterol-rich membrane fractions, then treated cells with agonistic antibody and measured caspase-8 activation. Jurkat cells with membrane cholesterol (i.e. not treated with MβCD) efficiently activate caspase-8 upon the addition of DR5 agonist (Figure 4-1, compare gray and black distributions). Pre-treatment with MβCD results in a reduced ability of these cells to activate caspase-8 (Figure 4-1, compare gray and black distributions).

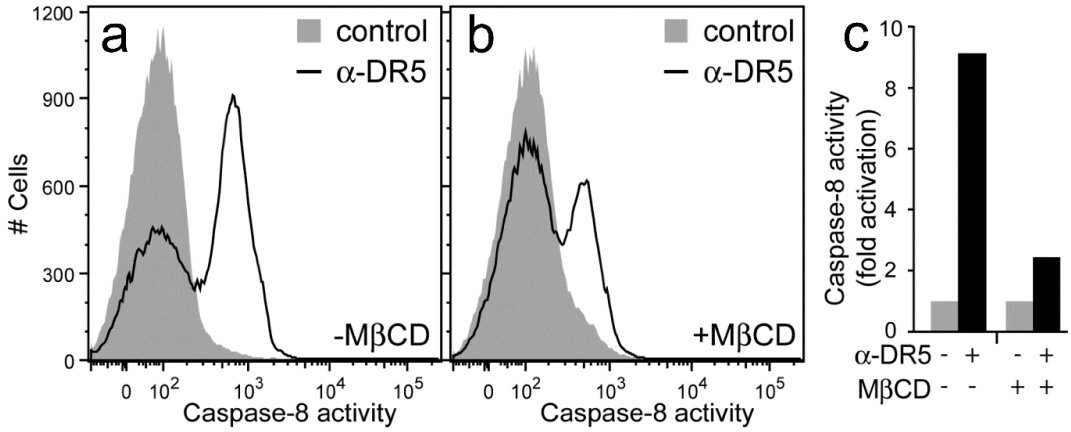

Figure 4-1. Membrane cholesterol is required for efficient activation of caspase-8 by DR5. Jurkat cells were pre-treated with either control (A) or MβCD (B), followed by no treatment or α-DR5 (grey distribution and black line, respectively), and caspase-8 activity was measured using Red-IETD-FMK and flow cytometry. Plotted is a histogram of caspase-8 activity level showing the ligand-dependent activation of caspase-8 and reduced activity in cells pre-treated with MβCD. (C) The activation of caspase-8 is quantified using identical gating schemes on each population, and the results are plotted as fold activation of caspase-8.

4.4.2 Ligand-receptor networks form in the absence and presence of membrane cholesterol

DR5 agonistic antibody has been established to induce DR5 network formation (43), and we have confirmed above that it drives the co-localization of the receptor to cholesterol-rich membrane fractions. However, there is no clear evidence that lipid rafts induce DR5 network formation or *vice versa*. Ligand-receptor networks are routinely identified using confocal fluorescence microscopy, as in this study, in order to quantify cluster size and number (43, 63, 127). Jurkat cells were pre-treated with MβCD (or control), to extract membrane cholesterol, and cells were subsequently treated with DR5 antibody agonist. Receptor-bound agonist was labeled with fluorescent secondary antibody and imaged using confocal microscopy to quantitatively determine the extent of network formation in

the membrane with and without MβCD treatment (Figure 4-2). Treatment of Jurkat cells with MβCD has been shown to deplete cholesterol within 30 minutes in a dose-dependent manner and extracts cholesterol preferentially from the plasma membrane, since it is not believed to enter live cells (159). Cell cholesterol content was measured using the Amplex Red assay to confirm ~50% cholesterol depletion in MβCD treated cells. We measured 0.45 μg cholesterol per μg lysate in untreated vs. 0.19 μg cholesterol per μg lysate in MβCD treated cells, a reduction of 58%. Removal of cholesterol much beyond 50% has been shown to cause substantial cell death in Jurkat cells (160). Images were taken in 3 separate experiments and the mean and standard error of each measurement were calculated.

In both untreated and MβCD treated cells, stimulation with labeled mAb631 resulted in punctate staining along the cell membrane indicating ligand-receptor clustering (Figure 4-2a,b) as has been shown previously in DR5 and other members of the TNFR superfamily (43, 65, 128, 160-163). To determine the number and size distribution of these DR5 networks we fit the angular intensity trace to a 1D mixed Gaussian distribution (Figure 4-2c). The total integrated label intensity reports the total ligand bound per cell, while the total number of peaks in each cell reports the number of independent networks, and the heights and widths of the individual Gaussians were used to determine network size. Quantitative analysis revealed no significant differences in the extent of network-formation in untreated and MβCD treated cells. Total fluorescence per cell was determined by taking the area-under-the-curve (AUC) of the raw angular intensity trace. The AUC in the untreated and MβCD treated cells were $1.49 \times 10^5 \pm 3.8 \times 10^4$ and $1.17 \times 10^5 \pm$

2.06x10^4, respectively (Figure 4-2d), indicating that cholesterol depletion did not inhibit mAb631 binding. The average number of clusters per cell was 38.2 ± 0.85 and 39.3 ± 0.95 in the control and MβCD treated cells respectively (Figure 4-2e). Peaks were counted as any bin along the angular integration with higher intensity than both neighboring bins, and therefore, any fluorescence above background is counted. The Gaussian integral of each of the networks, calculated as $a|c|\sqrt{\pi}$ where a is the height of the curve peak and c is the standard deviation, reveals the distribution of cluster sizes (Figure 4-2f). DR5 in both the control and MβCD treated cells formed networks with integrated intensity varying widely between ~10 and 2x10^4 (intensity units) with equivalent distributions. Error bars are calculated from triplicate experiments and reported for every eighth bin for clarity. Lastly, we plotted the distribution of network widths (calculated as $4 \times c$ to represent the arc length in degrees containing 95.4% of the labeled receptor) (Figure 4-2g). Again, both control and MβCD cells behaved the same, with network sizes centered at 10°. Assuming a cell of radius 3 μm, a 10° arc spans 524 nm, which is on the same scale as the Fas networks measured by Siegel et al. (63). To conclude, treatment with MβCD does not prevent agonist binding, and no difference in average network size is discernible in cholesterol depleted vs. control cells, strongly suggesting that mAb631-DR5 clustering is not raft dependent.

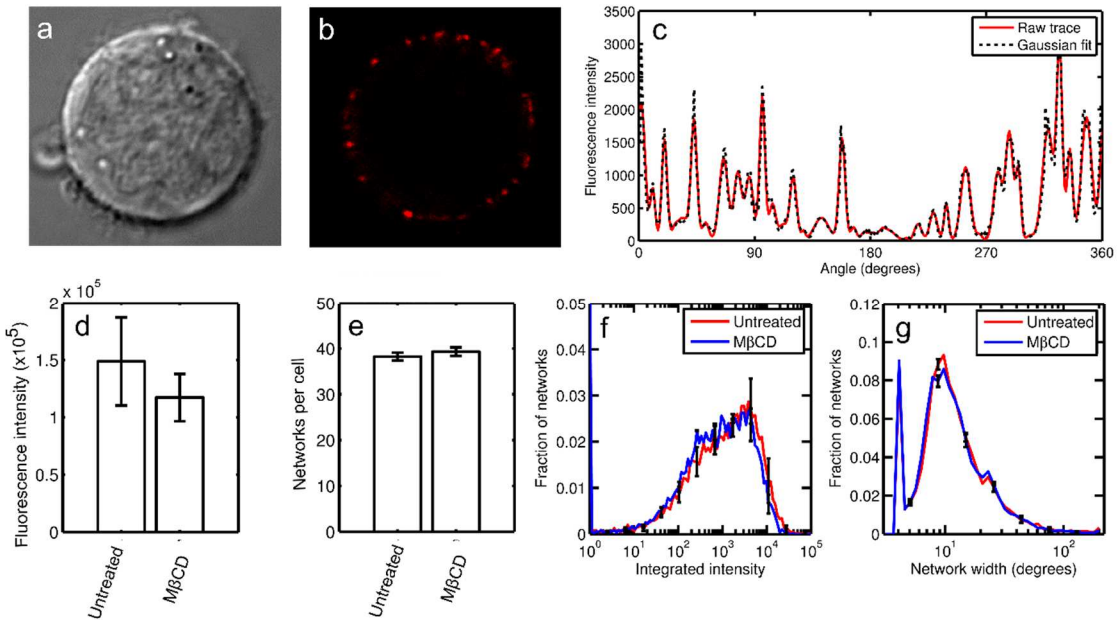

Figure 4-2. Ligand-receptor cluster formation does not require membrane cholesterol. Jurkat cells were treated with mAb631 and labeled with fluorescent secondary antibody. Shown are Jurkat cells under transmitted luminescence (a), ligand-receptor clusters illuminated by fluorescently labeled agonist antibody (b), and the angular fluorescence intensity trace for the cell shown (c). The raw trace is shown in black and the Gaussian fit in blue. The total ligand bound (d), number of clusters per cell (e), and distribution of SPOTS sizes are invariant between untreated and MβCD treated cells.

4.4.3 Membrane cholesterol is required for dimerization of DR5 in response to ligand

We have shown previously that upon the addition of antibody agonist DR5 forms disulfide-linked dimers that are subsumed within ligand-receptor networks (43). Figure 4-3 repeats this result, and is expanded to assess whether extraction of membrane cholesterol has any effect on ligand-induced DR5 dimerization. Jurkat cells were pre-treated with MβCD (5mM) or left untreated, and cells were subsequently washed and treated with DR5 antibody agonist, cross-linked, and lysed. Equal amounts of total protein were run on non-reducing SDS-PAGE and DR5 dimerization and oligomerization were analyzed by Western blot (Figure 4-

3a). As can clearly be seen in the control cells, the ligand-induced DR5 dimer band disappears upon cross-linking (compare lane 2 to 4), because the dimer becomes part of the larger crosslinked network. The dimer band is present in the uncrosslinked sample (lane 2) because it is held together by a disulfide bond between TM helices via Cys-209, as previously shown (43). The networks can be seen clearly as high molecular weight species larger than 260 kDa, and are induced by addition of ligand in both untreated and MβCD treated cells (lanes 4 and 8).

Cells pre-treated with MβCD have a markedly diminished ability to form DR5 dimers (Figure 4-3a, b). To better evaluate the extent to which MβCD inhibits disulfide-linked dimerization of DR5, we ran the agonist treated and untreated samples with and without MβCD, then densitometrically quantified the amount of dimer using ImageJ. The Western blot in Figure 4-3b shows a smaller reduction in dimerization than that in Figure 4-3a, however quantification reveals significant differences between dimerization in untreated vs. MβCD treated cells (from 7 independent experiments). In cells containing cholesterol, the addition of ligand causes a four-fold increase in the dimeric population of DR5. After pre-treatment of Jurkat cells with MβCD, ligand causes only a 2.5-fold increase in DR5 dimerization (Figure 4-3c). Therefore, while depletion of membrane cholesterol does not alter the formation of large DR5 networks, it does influence the covalent structure of DR5 dimers subsumed within these oligomers.

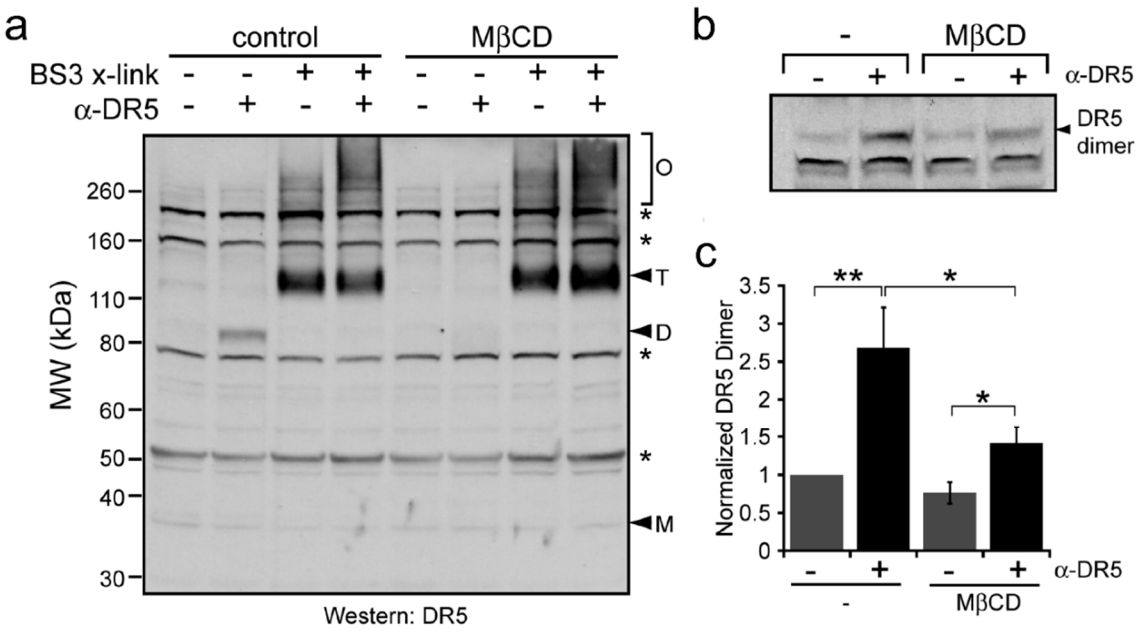

Figure 4-3. Extraction of membrane cholesterol inhibits ligand-induced DR5 dimer formation. Jurkat cells were pre-treated with either control or MβCD, as indicated, to extract membrane cholesterol. Cells were subsequently washed and treated with α-DR5 agonist and lysed. Lysates were analyzed via non-reducing SDS-PAGE and Western blot using an antibody against DR5. Agonist-bound DR5 formed oligomeric networks in both untreated and MβCD treated cells (a, lanes 4 and 8). Asterisks indicate non-specific bands. Disulfide-linked dimerization of DR5 via Cys209 occurred only in untreated cells (a, lane 2).Shown is the dimeric form of DR5 at approximately 85kd from a separate experiment (b).Quantification of DR5 dimer bands shows a significant increase in DR5 dimerization upon treatment with ligand, and that pre-treatment with MβCD diminishes DR5 dimerization (c).

4.4.4 Molecular simulations suggest that membrane thickness controls DR5-L TM domain helical stability and Cys209 partition depth

We have shown that migration to DRM fractions is necessary for ligand-induced DR5-L covalent dimerization, however the biochemical and structural features of lipid rafts that promote disulfide-bond formation are unknown. To further explain this finding, we ran REMD simulations to explore differences in the preferred low-energy conformations of the DR5-L TM dimer in a thick (40 Å,

corresponding to cholesterol-rich) vs. a thin (32 Å, corresponding to cholesterol-depleted) bilayer. We have previously simulated the disulfide-linked TM dimer to predict the structure and dynamics of the covalent dimer (43) however, here we simulated two un-bonded monomers. We hypothesized that disparate bilayer thicknesses would give rise to differences in monomer-monomer interactions, tilt, and helicity, and suggest the basis by which the thicker membrane promotes disulfide-bond formation. REMD is a powerful computational tool that allows a system to rapidly overcome free energy barriers and access low-energy conformational states while preserving ergodicity, however our results should be interpreted with the caveat that the accessible conformational space of the isolated TM domains, absent explicit membrane molecules, differs from that of the intact protein *in situ*.

We previously observed the formation and stability of the tightly packed GxxxG dimerization motif (97, 134) in the disulfide linked DR5 TM domain dimer, one helical turn downstream of Cys209 (43). This motif is likewise stable in the non-bonded dimer in both the 32 Å and 40 Å bilayers (Figure 4-4). We expect that the presence of this motif stabilizes the dimer and thus promotes disulfide bond formation. Interestingly, the occurrence of the motif is more frequent in the thicker bilayer (Figure 4-4A). It should be noted that while this bilayer thickness dependence was clearly observed in two of the four starting configurations, the difference was less convincing in the other two (Figure 4-7).

We then investigated three other possible thickness dependent differences: helix tilt, helicity, and partition depth. Because our simulation of the isolated TM

domain is able to access conformations that may not be sampled by the full-length protein or are otherwise not pertinent to the TM domain dimer (e.g. those in which the two helices are non-interacting), for the remainder of the analysis we compared only those structures in which the GxxxG interface was present (Figure 4-4a, boxed) The overall trends were the same if we considered all structures generated by the simulations. Bilayer thickness-dependent helix tilt and helical content due to hydrophobic mismatch (mismatch between the bilayer thickness and hydrophobic length of the TM domain) are often cited as determinants of TM domain behavior. We observed low tilt angles in both the 32 Å and 40 Å bilayers with little evidence of dependence on thickness (average tilt of 19˚ and 23˚ respectively, Figure 4-7). We then used the DSSP algorithm (164, 165) to calculate peptide secondary structure to determine whether bilayer thickness influenced helicity. We found that the same residues were helical in both bilayers, however helicity was increased by ~40% throughout the hydrophobic length of the peptide in the thicker bilayer (Figure 4-4b). The most obvious explanation for an increase in helicity is that the interfacial (N-terminal), partially solvent-exposed residues in the thinner bilayer become more stably folded in the thicker bilayer in order to minimize their free energy. This offers an explanation for how the thicker bilayer favorably positions the two Cys209 residues for disulfide bond formation (by stabilizing them in the helices on the same helical face as the GxxxG motif).

The DR5 TM domain notably contains a Trp at residue 237 which partitions to the switching region of the bilayer (corresponding to the headgroup/acyl chain region of an explicit bilayer). Trp residues are well-known to anchor TM helices in

this region (166-170). As shown in Figure 4-4c,d, Trp237 partitions to the switching region in both systems. This causes Cys209 to partition to the switching region of the 32 Å bilayer, but draws Cys209 deeper into the low-dielectric region (corresponding to the bilayer interior) of the 40 Å bilayer. Immersion of these interfacial residues in the hydrophobic region of the bilayer may promote their folding into a stable helix. Additionally, a hydrophobic environment has been theorized to dramatically reduce the energy barrier of disulfide-exchange (171), and burial of Cys209 in the bilayer may enhance the rate of disulfide bond formation in rafts. Thus, a combination of increased helicity and hydrophobic immersion of Cys209 in thicker bilayers may explain the increased propensity to form disulfide-linked dimers.

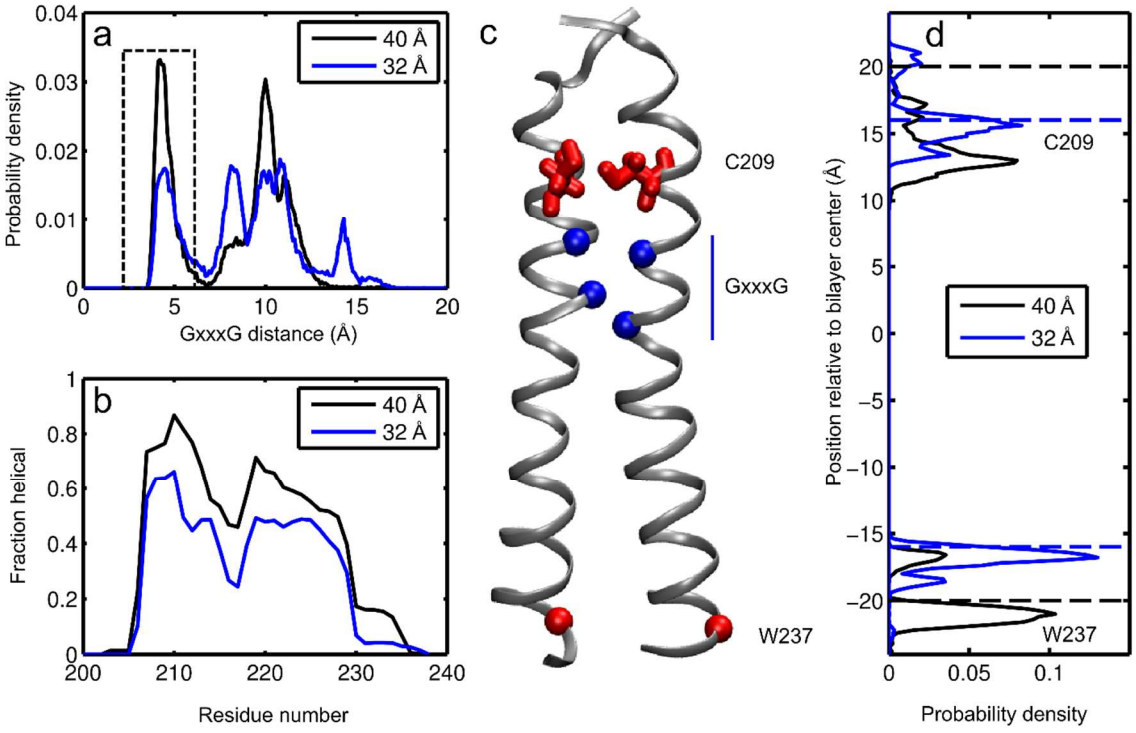

Figure 4-4. Membrane thickness affects DR5-L TM domain helical stability and Cys209 partition depth. The DR5-L transmembrane dimer was simulated using

REMD. The average GxxxG distance was plotted to identify the likely dimer conformation (< 6 Å, dashed box). This dimer conformation was sampled in both the 40 Å (black) and 32 Å (blue) implicit bilayers representing raft and non-raft domains respectively (a). Subsequent analysis is conducted on only these frames. The fraction of frames with helical secondary structure shows increased helix stability in the 40 Å bilayer (b). A snapshot of the simulated peptide in its GxxxG dimer configuration is shown with C209 shown in red, the G(213)xxxG(217) motif shown as blue spheres, and W237 shown as a red sphere (c). Trp237 (Cα atom) partitions directly outside the switching region in both the 40 Å (black) and 32 Å (blue) bilayers. Cys209 (sulfur atom) partitions at the switching region in the 32 Å bilayer (blue), but deep within the low dielectric region in the 40 Å bilayer (black) (d). The positions of the switching regions of each bilayer are shown as dashed horizontal line.

4.5. Discussion

Raft-dependent activation has been previously observed in a number of TNF receptors including DR5 (144) when induced by TRAIL. We have shown that raft-dependence is similarly a feature when DR5 is activated by agonistic antibody. Previously, Song et al. showed that DR5 in non-rafts (in TRAIL insensitive cells) triggered the NF-κB pathway rather than the apoptotic pathway (144). We did not investigate whether mAb631 induces NF-κB activation in cholesterol-depleted cells, however ongoing work will investigate this possibility. If mAb631 does activate the inflammatory pathway in cholesterol-depleted cells, it would suggest that DR5 clusters that are not stabilized by disulfide bonding recruit different cytosolic machinery that activates the NF-κB pathway, either by favoring a different dimer structure or by altering the dimerization kinetics of the TM domain.

An additional possibility that we have not directly addressed is whether the depletion of cholesterol (elimination of rafts) prevents the co-localization of the receptor with the intracellular signaling machinery (the death inducing signaling complex, or DISC). In the case of Fas-induced apoptosis, the components of the

DR5 DISC are not constitutively present in the rafts (142), and they have been shown to co-immunoprecipitate with DR5 in both rafts and non-rafts (144). Therefore, the available evidence suggests that co-localization of the DISC and DR5 is not purely raft-driven. Nonetheless, our data cannot fully rule out this possibility.

Raft-driven disulfide-bond formation has also been observed in the TM domain of the influenza A M2 protein (172). The TM domain of M2 resembles that of DR5-L with respect to its secondary structure, presentation of an extracellular cysteine, and propensity to form disulfide bonded multimers. Most importantly, the extent of dimerization of the M2 TM helix via disulfide bonding was shown to directly depend on both bilayer thickness (varied by changing the lipid chain length) and cholesterol concentration (which is also known to increase bilayer thickness) (173, 174). Specifically, Cristian et al. maximized disulfide-bond formation of the 28.5 Å long M2 peptide in a 26.5 Å POPC bilayer (172). This translates to an angle of 21.6°, effectively the same as our measured angles for DR5-L. Furthermore, their result predicts that disulfide bond formation would be maximized in a thick, ~40 Å bilayer for DR5-L, a 43 Å TM domain measured from Cys209 to W237. This biophysical result is consistent with our finding in cells that lipid rafts, which are both thicker and more enriched in cholesterol than non-rafts, drive DR5-L disulfide-linked dimerization.

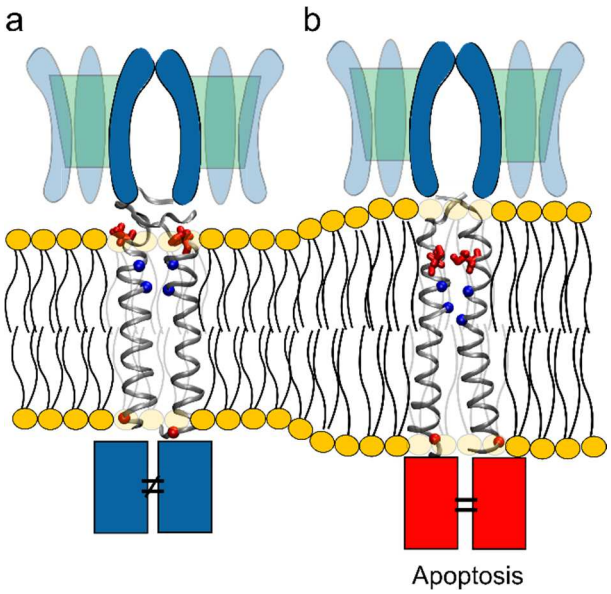

Figure 4-5. Updated activation model for DR5 incorporating bilayer structure. Instability in the transmembrane helix inhibits covalent dimerization of DR5 via Cys209 in non-rafts (a). Translocation to lipid rafts draws the cysteines into the bilayer interior, stabilizing the TM helices and driving disulfide bond formation (b).

To conclude, our findings are further evidence that signaling by DR5 is driven by the formation of highly-organized networks in which structure is guided by not only receptor-receptor and ligand-receptor interactions, but also receptor interactions with the lipid membrane. Specifically, our results show that network formation does not depend on the local lipid microenvironment. However, in order for networks to be functional, at least in the case of the long isoform, the DR5 transmembrane domain must undergo raft-dependent dimerization via Cys209. In non-rafts, instability in the transmembrane helix inhibits covalent dimerization of DR5-L. When the receptor translocates into lipid rafts, the cysteines are drawn into the bilayer interior, stabilizing the TM helices and driving disulfide bond formation (Figure 4-5). The disulfide-linked DR5 dimer, subsumed within the ligand-receptor

network that is immersed in a lipid raft, can then undergo a transition to the active state as our previous results suggest (53, 60).

4.6. Supplemental Figures

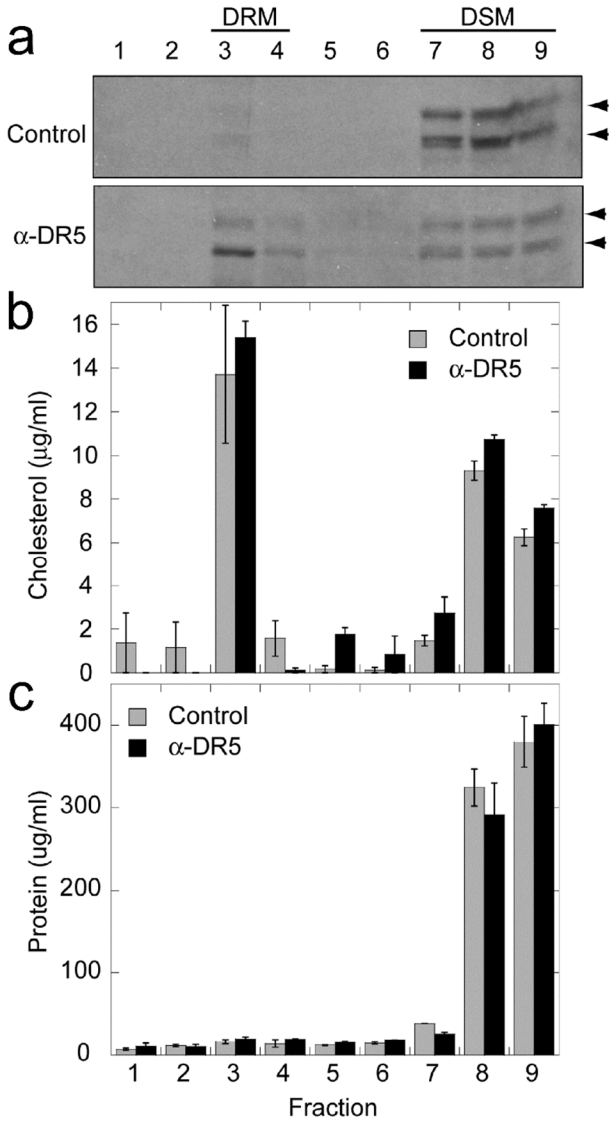

Figure 4-6. Agonistic antibody causes relocalization of DR5 into cholesterol-rich membrane regions. (A) Jurkat cells were treated with DR5 agonist (α-DR5) or left untreated, triggering DR5 migration from high-density DSM fraction to low density DRM fraction upon stimulation with agonist. DR5 isoforms are indicated by arrowheads. (B) Cholesterol concentration in each fraction shows cholesterol enrichment in DRM fraction 3, suggesting the presence of cholesterol-rich lipid

rafts, in control and agonist treated samples (gray and black bars, respectively). (C) Total protein content measured in each fraction in the absence and presence of agonist (grey and black bars, respectively).

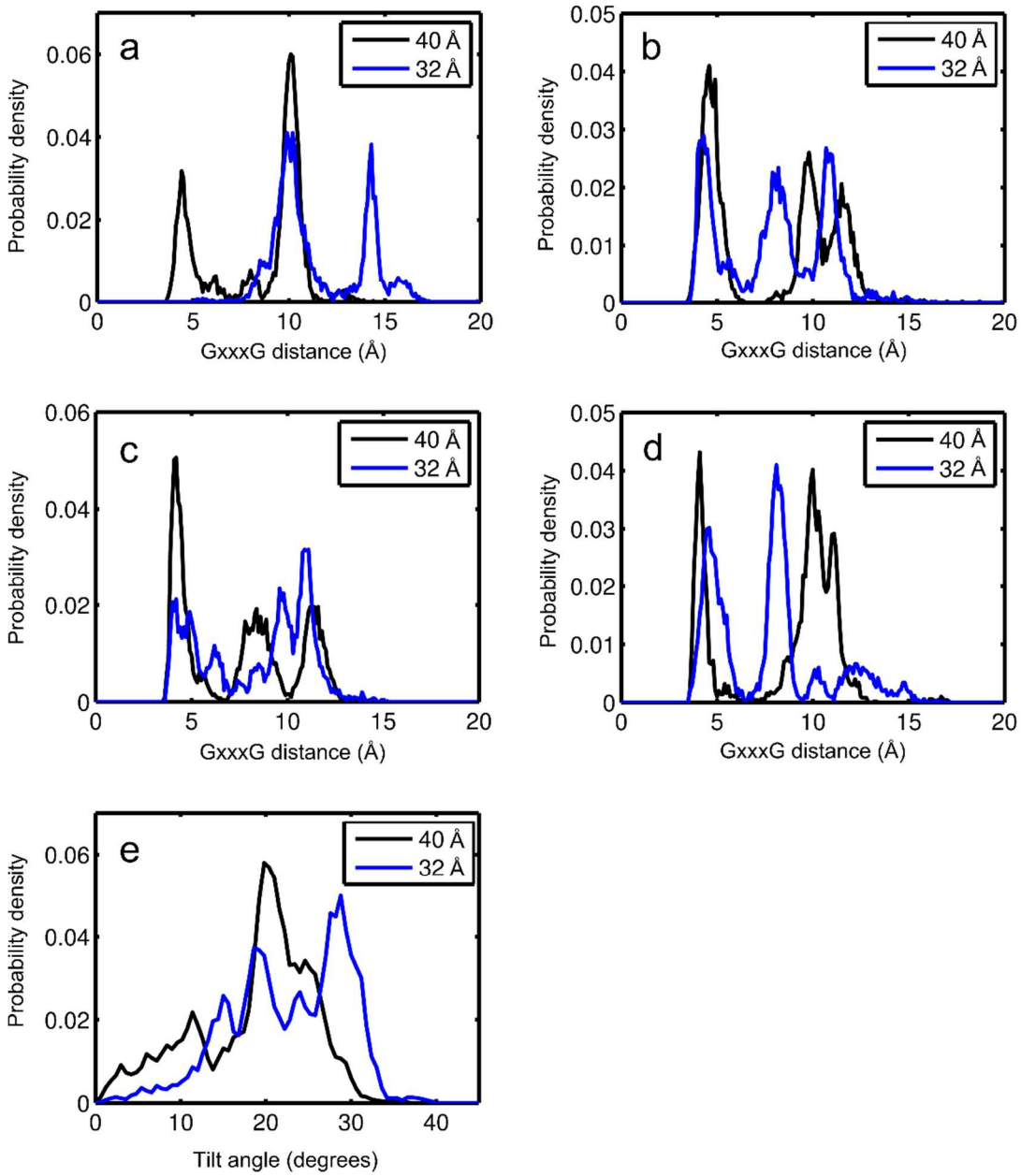

Figure 4-7. Plots of GxxxG distance for REMD simulations from each of the 4 starting configurations (A-D). Tilt angles of the GxxxG dimer conformations in the 40 and 32 Å bilayers (E).

Chapter 5 – Oxidation Increases the Strength of the Methionine-aromatic Interaction

5.1. Prefatory note

This chapter builds on a previous publication in the Sachs Lab that studied the prevalence and importance of the methionine-aromatic interaction, especially where it serves as a critical element of the binding interfaces that join TRAIL to DR5 and LTα to TNFR1(43). As a middle author of that paper, I contributed immunoprecipitation and functional data that showed that abolishing either component of these methionine-aromatic motifs resulted in substantial reduction in LTα/TNFR1 binding and signaling. That publication left a lingering question – what happens to the methionine-aromatic motif when methionine is oxidized? – The LTα/TNFR1 system was well suited to address this question as the methionine was in the ligand and could be modified without subjecting the cell to cytotoxic levels of oxidative stress. Thus, we ran the same experiments, oxidizing LTα instead of mutating it. This led to the multi-disciplinary, in-depth investigation of oxidation of the methionine-aromatic motif that follows.

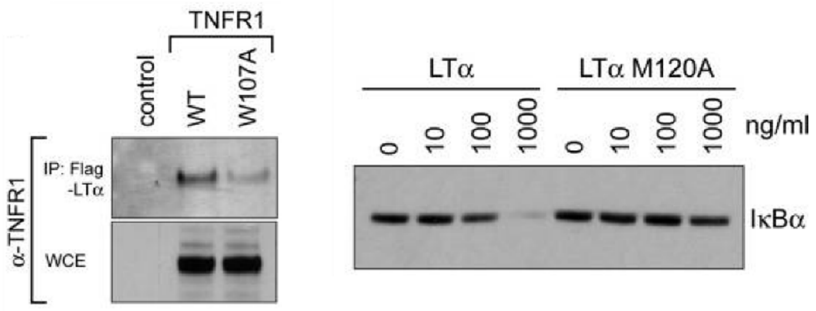

Figure 5-1. The met-aromatic interaction in LTα/TNFR1. Mutation of the aromatic-containing residue within the structurally homologous loop in TNFR1 disrupts

interaction with its cognate ligand, LTα, measured by immunoprecipitation. Whole cell lysates show equal expression of wild type and mutant receptor (left). Cells were treated with various concentrations of LTα ligand, wild type and mutant. Mutation of the sulfur-containing methionine residue within LTα ligand disrupts the function, shown by degradation of IκBα at various concentrations of ligand (right). Adapted from Valley et al. (43).

5.2. Summary

Oxidation of methionine disrupts the structure and function of a range of proteins, but little is understood about the chemistry that underlies these perturbations. We show, using quantum mechanical calculations, that the strength of the methionine-aromatic interaction motif, a driving force for protein folding and protein-protein interaction that has emerged in recent years, is increased by 0.5 – 1.4 kcal/mol when methionine is oxidized and no hydrogen bonds are formed. We performed thermal denaturation experiments on model peptides to show that oxidation of the motif stabilizes the interaction by 0.5-0.6 kcal/mol. We also find that non-hydrogen bonded interactions between dimethyl sulfoxide and aromatic groups are prevalent in both the Protein Data Bank and Cambridge Structural Database, and are enriched over dimethyl sulfoxide/aliphatic interactions. We confirm the biological relevance of these findings through a combination of cell biology, electron paramagnetic resonance spectroscopy and molecular dynamics simulations on 1) calmodulin structure and dynamics and 2) lymphotoxin-α/TNFR1 binding. Thus, the methionine aromatic motif is a determinant of protein structural and functional sensitivity to oxidative stress.

5.3. Introduction

The methionine-aromatic motif is now recognized as a promiscuous, highly stabilizing non-covalent interaction that forms between methionine thioether sulfurs and the aromatic rings of nearby (~5 Å) tyrosine, tryptophan, and phenylalanine residues(175-180). Methionine-aromatic interactions are present in ~33% of protein structures (Protein Data Bank (PDB) as of 2012), and the majority of those structures have more than five instances of the motif. The motif is significant because it is substantially stronger than a purely hydrophobic contact, suggesting that it plays a unique role in stabilizing both protein structure and ligand-receptor binding(175), and potentially expanding on the evolutionary significance of methionine as a member of the amino-acid library.

Methionine-aromatic interactions were first detected in a small bioinformatics study that found alternating sulfur-containing and aromatic amino acids in eight protein structures(179, 180). An analysis of 36 protein structures in 1985(177) and our exhaustive analysis of the PDB (as of 2012) confirmed that methionine-aromatic interactions are enriched compared to aromatic interactions with non-sulfur-containing amino acids(175). A search of the Cambridge Crystallographic Structural Database (CSD) similarly found an abundance of sulfur-aromatic (S/Ar) interactions between the C-S-C divalent sulfur motif and aromatic groups(176). The interaction free energy between methionine and phenylalanine has been studied experimentally(181, 182). One such study measured the Met-Phe interaction (-0.65 ± 0.15 kcal/mol) in a thermal unfolding experiment of a synthetic helical peptide with phenylalanine and methionine at

positions *i* and *i*+4 respectively(182). Quantum calculations by Pranata revealed an interaction energy of 1-3 kcal/mol at a range of 4-6 Å between dimethyl sulfide (DMS) and benzene(178). Our own quantum calculations confirmed these results, and expanded the analysis to include DMS interactions with phenol and indole, recapitulating the methionine-tyrosine and methionine-tryptophan interactions, respectively, and identified that dispersion interactions are the major contributors to stability(175).

In addition to forming highly stabilizing interactions with aromatic residues, methionine is uniquely important because it is susceptible to oxidative modification(183). Oxidation is widely studied in the context of diseases ranging from inflammatory diseases (such as Crohn's disease(34), rheumatoid arthritis(184) and irritable bowel syndrome(185)) to pulmonary fibrosis(186, 187) and cancer(188, 189) among others. In oxidizing environments, the methionine thioether can undergo modification with the addition of one or two sulfonyl oxygens to become methionine sulfoxide (Met^{Ox}) or sulfone, respectively(183). Elevated levels of methionine sulfoxide have been detected in diseased tissues, but methionine sulfone is rare(190). Methionine sulfoxidation is known to regulate the activity of certain proteins, while in other cases, methionine-rich domains protect critical amino acids from oxidation by removing free radicals and regulating the local redox environment(191).

Despite this functional significance, the specific molecular mechanism through which proteins sense and respond to oxidative modification of methionine residues has not been fully characterized. It has been posited that polarization of

the methionine thioether by oxidation could weaken the methionine-aromatic interaction by ablating the hydrophobic contribution(192), but this has never been tested experimentally. In the present study we will show the opposite to be true – that oxidation of methionine strengthens its interaction with aromatic residues, and that this has the potential to disrupt native conformation and alter protein function. Importantly, we show that the interaction is strengthened even in the absence of a hydrogen bond between the sulfoxide oxygen (acceptor) and donor hydrogens (on Tyr or Trp). Through quantum mechanical calculations, we show that the interaction between the dipole moment of dimethyl sulfoxide (DMSO) and the aromatic ring quadrupole moment is the main contribution to the increased stability of the motif.

We start by analyzing both the PDB and the CSD to identify and characterize interactions between DMSO (a small molecule analog to Met^{Ox}) and aromatic groups in the crystal structures of proteins and small molecules. DMSO has previously been shown to solubilize tryptophan more readily than leucine, alanine, and glycine(193), so we expected to find that it specifically interacts with aromatic sidechains. We then performed quantum mechanical calculations on model compounds to determine the strength of the sulfoxide-aromatic interaction, and assessed the potential contribution of hydrogen bonding on the motif in a variety of solvent environments. We then isolated and determined the strength of the specific interaction between unoxidized and oxidized methionine and the sidechain of phenylalanine by extending a previously described helix unfolding experiment and performing a double mutant cycle analysis(182).

We investigated the effects of site-specific methionine oxidation on the methionine-aromatic interaction in two biologically important proteins. First, using a combination of electron paramagnetic resonance (EPR) spectroscopy and replica-exchange molecular dynamics (REMD) simulations, we probe the effects of oxidation on the structure of calmodulin (CaM). CaM is one of the best-documented examples of a protein whose function is modulated by methionine oxidation. The nine methionine residues are targets for reversible oxidation, which serves as a mechanism through which the cell senses and responds to oxidative stress by modulating metabolism and energy utilization(194-197). Published data suggests that methionine oxidation can perturb local secondary structure, induce conformational disorder, and disrupt key hydrophobic interactions(198-201). Methionine oxidation in CaM has been shown to induce global structural changes(202) and impair the ability of CaM to regulate the ryanodine receptor calcium channel(203-205), the plasma membrane Ca^{2+} ATPase(202, 206-209), and other targets(210, 211). Here we provide evidence that interactions between methionine and aromatic side chains play a crucial role in CaM structure, correlating with functional changes induced by oxidation.

Second, we investigate lymphotoxin-α (LTα) binding to tumor necrosis factor receptor 1 (TNFR1), which we showed is stabilized by a methionine-aromatic interaction between M120 of LTα and W107 of TNFR1(175). TNFR1 is a type-I transmembrane protein that is activated by its ligand, LTα, and initiates the pro-inflammatory NF-κB pathway(12). Given that LTα has been implicated in a number of diseases that are also associated with local oxidative stress(34, 184-

189), and because the extracellular environment at sites of chronic inflammation and tumor is oxidative(212), it is critical to understand the impact of oxidation on the ligand's binding and potency in activating TNFR1. Tumor necrosis factor (TNF) is a ligand that binds to the same receptor targets and is similar in sequence, structure, and function to LTα, but notably lacks methionine residues. This provides a biologically relevant model system in which to directly investigate the effect of methionine oxidation on the methionine-aromatic motif. We find that oxidation of M120, which is indispensable for ligand-receptor binding via its interaction with W107, unexpectedly interferes with ligand activity and binding. Further investigation suggests this to be a result of competing interactions between oxidized M120 and nearby intramolecular tyrosine residues.

5.4. Results

5.4.1 DMSO-aromatic interactions are prevalent in small molecule and protein crystal structure databases

To find examples of sulfoxide-aromatic interactions, we searched the PDB and CSD for occurrences of DMSO molecules near aromatic rings (Figure 5-2). The PDB is a repository containing crystal structures of proteins and the CSD is the analogous repository for organic and metal-organic small molecules. We analyzed a non-redundant subset of the PDB comprised of all structures containing at least one DMSO molecule. Structures sharing >90% sequence identity were represented by a single structure with the highest score as ranked according to RCSB PDB quality factor algorithm. Redundant structures were excluded, as they do not represent truly independent data points for the purposes of our informatics

study. Our search yielded 205 unique structures containing a total of 872 DMSO molecules. A representative example showing a tyrosine aromatic ring and DMSO is shown in Figure 5-2a. There is a clear enrichment of aromatic residues 4-7 Å, with a maximum at 5Å, from DMSO sulfurs as compared to all amino acids or the aliphatic amino acids, closely resembling the radial density function for methionine in our previous study(175) (Figure 5-2b). 451 (51.7%) DMSO molecules were found within 7 Å of the center of the nearest aromatic residue. Only 32 of these (7.1%) are in position to accept a hydrogen bond from either tryptophan or tyrosine. Thus, hydrogen bonding does not play a substantial role in DMSO-aromatic bonding in the PDB. Our search of the CSD similarly found an ~50% enrichment of DMSO-aromatic contacts (representative example, Figure 5-2c) compared to C-CH_2-C-aromatic pairs (Figure 5-2d), which were used previously as non-interacting control to show the enrichment of the Met-aromatic motif(176). Again, only a small percentage of the CSD instances of DMSO/phenol or DMSO/indole pairs were in position to form a hydrogen bond (<14%).

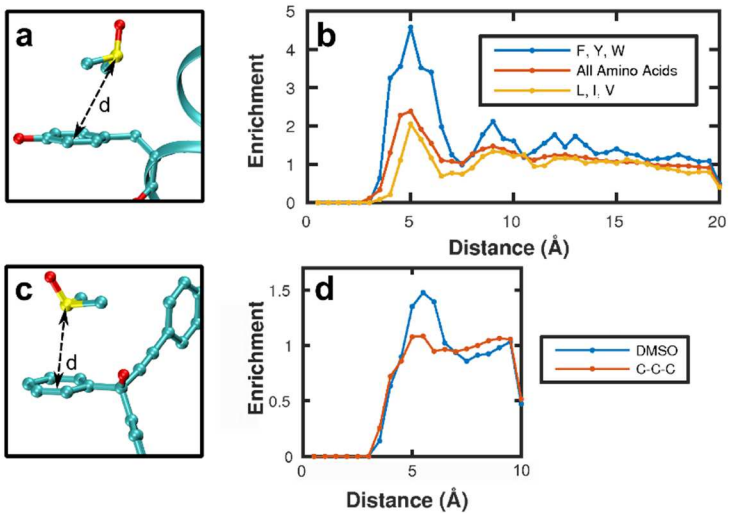

Figure 5-2. Structural informatics search of the CSD and PDB. A representative snapshot of a DMSO-aromatic interaction taken from the PDB (PDB: 4KAD) (a). The radial distributions of all amino acids and aromatic amino acids is plotted relative to DMSO, showing a clear enrichment of aromatic residues 4-7 Å from DMSO (b). We compare to the radial density of all amino acids and the aliphatic amino acids, Leu, Ile, and Val, relative to DMSO. A representative snapshot of a DMSO-aromatic interaction taken from the CSD (CSD: AWUHEF) (c). The radial density of aromatic groups relative to DMSO sulfur shows an enrichment around 4-7 Å (d). We compare to the radial density of aromatic groups relative to C-CH_2-C motifs, which are non-interacting.

We then parsed the frequency of methionine-aromatic interactions in the PDB <7 Å between DMSO and the center of phenylalanine, tyrosine, and tryptophan individually. Figure 5-3a shows that the interaction is more prevalent with Tyr and Trp than with Phe when normalized by the relative abundance of each of these amino acids in our non-redundant, DMSO-containing subset of the PDB. This trend is not explained by relative solvent accessibility, as Trp and Phe have similar solvent accessibilities, while that of Tyr is somewhat higher(213). We calculate a 1.3 and 1.4 fold preference for tyrosine and tryptophan over phenylalanine, respectively, translating to a ~0.3 kcal/mol increase in Met-Tyr and Met-Trp stability compared to Met-Phe. Therefore, these database results suggest that, even though hydrogen bonding is not common in the interaction motif, DMSO interacts more favorably with tyrosine and tryptophan than with phenylalanine. This has similarly been observed in cation-π interactions in proteins, where the more electron rich Pi systems of tryptophan and tyrosine relative to phenylalanine make them more attractive to positively charged ligands(214).

5.4.2 Quantum calculations reveal that oxidation strengthens the sulfur-aromatic interaction

The interaction energy between the reduced (DMS) and oxidized (DMSO) models of methionine with the model aromatic compounds benzene, phenol, and indole was calculated with full geometry optimizations using the Møller-Plesset perturbation theory at the second order (MP2) in gas phase as described in the Quantum Calculations Methods section. The results corrected for basis set superposition error are reported in Table 5-1 and the corresponding structures are shown in Figure 5-7. Uncorrected interaction energies and M06-2X data are shown in Table 5-4. The data show that upon oxidation of DMS to DMSO the complex with benzene is 0.9 kcal/mol more stable. To understand the origin of this stabilization we first tested the possible contribution of dispersion interactions, which we previously found contributed to the increased stability of the complex between DMS and benzene when compared to its sulfur-free analog, propane(175). The results (Table 5-5) show that the dispersion energy contribution for DMS/benzene is -8.4 kcal/mol, and for DMSO/benzene it is -8.2 kcal/mol. The change in dispersion energy contribution is small (0.2 kcal/mol) and is more stabilizing for the DMS/benzene interaction than for the DMSO/benzene. Therefore dispersion interactions are not the source of the stronger interaction energy in the oxidized complex. Rather, the stronger interaction can be explained in terms of the interaction between the dipole moment of DMSO and the aromatic ring quadrupole moment. The calculated dipole moment for DMS is 1.8 Debye, while in DMSO the enhanced polarization due to the presence of oxygen results in

a dipole moment of 5.0 Debye roughly aligned along the S=O bond. Furthermore, both DMS and DMSO maximize dispersion interactions with the benzene ring by aligning the Me-S-Me moiety over the ring plane; as a result, in the DMS/benzene complex the orientation of the small dipole of DMS is orthogonal to the benzene quadrupole moment, while in DMSO/benzene the angle between the S=O bond and the ring is approximately 120°, which is well poised for a favorable dipole/quadrupole interaction. The Natural Bond Orbital (NBO) charge analysis for the complex and isolated species (see Table 5-6 and Figure 5-9) supports this explanation, showing a large positive charge (+1.19 e) on the sulfur that can interact with the π electron cloud, balanced by a negative charge (-0.96 e) on the oxygen that is pointing away from the benzene ring (see Figure 5-7).

	Benzene	Phenol	Indole
DMS	-2.4	-4.9	-4.7
DMSO	-3.3	-10.6	-10.0

Table 5-1. Interaction energies for DMS or DMSO with benzene, phenol and indole. Results in kcal/mol are computed for fully optimized structures at the MP2/6-311+G(d,p) level and corrected for basis set superposition error. The corresponding structures are reported in Figure 5-7.

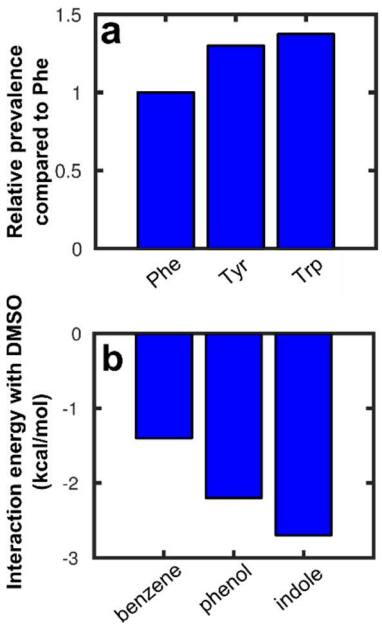

Figure 5-3. Relative frequency of DMSO interactions with phenylalanine, tyrosine, and tryptophan corresponds to interaction energy. The fraction of DMSO molecules participating in a methionine-aromatic interaction with each aromatic residue is plotted. These values are normalized against the abundance of each aromatic group in the PDB subset analyzed and shows enrichment of interactions with tyrosine and tryptophan compared to DMSO-phenylalanine interactions (a). Interaction energies calculated at the MP2/6-311+G(d,p) with CP-corrections for the complexes between benzene, phenol, and indole and DMSO. The structures exclude hydrogen bonding and are calculated using ensembles of configurations from the simulations as described (b).

Table 5-1 shows that for phenol and indole the change in interaction energy upon oxidation of DMS to DMSO (-5.7 and -5.3 kcal/mol, respectively) is of larger magnitude than for benzene. Such a large change cannot be explained in terms of enhanced dipole/quadrupole interactions, and is a result of specific hydrogen bond interactions between the negatively charged DMSO oxygen and the hydrogen of the phenol hydroxyl group or the indole amine (see Figure 5-7). To determine the relevance of hydrogen bonding in sulfoxide-aromatic interactions in a range of environments, we ran molecular dynamics simulations of DMSO and phenol, or indole in hexane, ethyl acetate (EtOAc), or TIP3P water using the adaptive biasing

force (ABF) module in NAMD. We found (see Figure 5-10) that DMSO hydrogen bonded substantially with phenol and indole in hexane. Thus, in this nonpolar environment we expect the contribution of the hydrogen bond to outweigh the increased interaction energy of the S/Ar motif. Importantly, in EtOAc (a polar non-protic solvent with dielectric constant of 6, fairly representative of the interior of a protein), hydrogen bonding occurred much less frequently. Therefore, the S/Ar motif plays a relevant role in the stabilization of the complex in this environment. Finally, in water hydrogen bonding between DMSO and the aromatic residues was essentially absent and replaced by solvation of the DMSO sulfonyl group and the aromatic hydrogen donor by water. This last simulation mimics the conditions of residues on the surface of a protein, which are often involved in protein-protein interactions(215).

To disentangle the energy contribution due to specific hydrogen bonding from that of sulfur-aromatic interaction, we performed quantum mechanical calculations on two ensembles of configurations from our simulations in EtOAc. Benzene and DMS systems were also run to compare to the results of our full optimization calculations. As discussed above, the EtOAc intermediate dielectric constant (~6) and its capability of accepting hydrogen bonds allows the complexes between DMSO and phenol/indole to sample both hydrogen-bonded and non-hydrogen-bonded conformations with similar probability. Therefore, by separating the structures that contained only sulfur-aromatic interactions from those that were hydrogen-bonded (see Methods), we analyzed two ensembles of conformations that are good mimics of the interactions on the surface of a protein and in its

hydrophobic core. The results reported in Table 5-2 and Figure 5-3b for ensembles of structures explicitly sampled in EtOAc solvent are in good agreement with the data from the full optimization reported in Table 5-1, and together indicate that (a) in the absence of hydrogen bond, oxidation of DMS to DMSO strengthens the sulfur-aromatic interaction by 0.5 - 1.5 kcal/mol, and (b) in hydrogen bonded structures (rare in proteins) the stabilization of the complex can be as strong as 8 kcal/mol.

	Benzene	Phenol	Indole
DMS	-0.9	-1.0	-1.3
DMSO Non H-bonded	-1.4	-2.2	-2.7
DMSO H-bonded		-9.0	-7.5

Table 5-2. Interaction energies in EtOAc. Interaction energies in kcal/mol of DMS or DMSO with benzene, phenol, and indole in EtOAc.

5.4.3 Evaluation of Oxidation in a Model Peptide Scaffold

To experimentally assess the database findings and quantum results, we used thermal denaturation of peptide constructs that were designed based on a previously reported 15-residue peptide scaffold. Thus, our approach recapitulates and expands on the first published experiments that were used to assess the strength of the S/Ar interaction (see Methods)(182). In that study, in which oxidation was not addressed, the Met-Phe pair was found to interact (ΔG_{int}) with 0.65 kcal/mol, establishing the baseline for our investigation of the oxidized methionine-aromatic interaction (which we denote as S^{Ox}/Ar). The peptides used here are the same as in that study: a phenylalanine is placed at position 9 and a methionine (or methionine sulfoxide) residue is placed at position 13 (Table 5-8). The peptide scaffold was originally designed such that the strength of the

interaction at these *i*, *i*+4 sites determines the thermal stability of the peptide secondary structure.

As shown in Table 5-3, our experiments reproduced the original S/Ar result for Met-Phe (ΔG_{int}=0.62 kcal/mol). Then, upon oxidation of the methionine, the data shows that the interaction between methionine and phenylalanine is doubled (strengthened by 0.62 kcal/mol). To obtain these results, we performed the same thermal unfolding experiment as done previously, monitoring the secondary structure of the peptide scaffold by circular dichroism (CD)(182). Two aspects of our approach differed from the original study. First, we performed a double mutant cycle to isolate the methionine-aromatic interaction from possible interference due to neighboring residues (Figure 5-12). This approach solidifies our reported interaction free energies, and is especially important in the case of oxidized methionine because of the increased likelihood of hydrogen bonds and electrostatic interactions with the other residues in the peptide.

Peptide	**ΔG_{Int} (kcal/mol)**
Phe-Met	0.62 ± 0.09
Phe-Met (ox)	1.24 ± 0.09

Table 5-3. Determined ΔG_{Int} for Phe-Met and Phe-Met^{Ox} at 0°C. ΔG_{Int} in kcal/mol determined through double mutant cycle analysis for Phe-Met and Phe-Met^{Ox}. ΔG_{Int} was determined at 0°C where the strongest α-helical character was present.

Second, we followed Greenfield(216) by fitting the temperature-dependence of each CD spectrum (Figure 5-13) to the Gibbs-Helmholtz equation (GHE, Figure 5-14). We justify applying a two-state approximation and hence using the GHE by: 1) observation of complete reversibility (overlap) in the heating and cooling curves (Figure 5-15); and 2) the presence of a molar ellipticity isodichroic

point in all constructs(217) (Figure 5-13, inset). Additionally, principal component analysis(218) of the CD spectra yielded only two components that dominated the CD spectra (Figure 5-16 and 0), again consistent with the two-state assumption. Together with the addition of the double mutant cycle, the fact that we obtained nearly identical values for the Met-Phe energy as in the original study (compare 0.62±0.09 to 0.65 kcal/mol) reinforces the robustness of our approach. Thus, our peptide study lends experimental support to the conclusions drawn from the quantum calculations: oxidation increases the strength of the methionine-aromatic interaction.

5.4.4 Oxidation of calmodulin transforms structure by establishing a new Met-aromatic contact

In order to test the impact of the increased strength of the S^{Ox}/Ar motif in proteins, we first investigated the effects of methionine oxidation in an already well-characterized protein, CaM. The C-terminal helix of CaM has a high methionine content and is sensitive to oxidative stress *in vivo,* which alters the protein's structure and function(202, 203, 206, 208, 209, 219). In the crystal structures of CaM, both in its calcium-bound (halo, 3CLN)(220) and unbound (apo, 1CFD)(221) forms, a C-terminal methionine forms an S/Ar interaction with F141 (M144 in apo (Figure 5-4a) and M145 in halo). It has been speculated previously that oxidation at M144 and M145 might destabilize the protein by altering an important, nearby hydrogen bond between Y138 and E82 that connects the short C-terminal helix to the central linker(202, 222). No specific molecular mechanism for this effect has been proposed or tested.

Based on our results above, one possibility is that oxidation of M144 and/or M145 increases the likelihood of an S^{Ox}/Ar interaction with Y138, which would be manifest in a spatial rearrangement within the C-terminal domain that should be observable by EPR. As M144/145 and Y138 are on opposite ends of a short helix, such an interaction would require helical unwinding, an effect that has been observed using NMR(207). Replica exchange molecular dynamics simulations (REMD) of the isolated, Ca^{2+}-free (apo) C-terminal peptide fragment (residues 136-146) of CaM were used to guide the design and interpretation of experimental EPR measurements on full-length protein. We simulated both the unoxidized and doubly oxidized (at M144 and M145) forms. Because of the expectation of helical unwinding, a computational investigation of full-length CaM is hampered by limitations in sampling efficiency. Thus, while the peptide fragment is an abstraction of the real system, it is nevertheless a useful tool because it accelerates the sampling of relevant conformational space. Furthermore, the simulations were useful in 1) establishing V136 and T146 as appropriate sites for spin-labels to test the impact of oxidation on the full-length protein; and 2) providing molecular scale details unavailable from EPR that correlate distance changes to the potential presence of an S^{Ox}/Ar motif.

In the simulation of the unoxidized peptide, an S/Ar interaction formed between Y138/M144 or Y138/M145 only 3.3% of the time. On the other hand, an S^{Ox}/Ar interaction formed 22.7% of the time when both M144 and M145 were oxidized (Figure 5-4b, Figure 5-17). In only 1.2% of these interactions did a hydrogen-bond form (Figure 5-18). As can be seen in Figure 5-4b, the S^{Ox}/Ar

interaction with Y138 leads to a spatial rearrangement that brings together residues V136 and T146. The distribution of the distance between the Cα atoms of those two residues is shown in Figure 5-4c. Likewise, the frequency of the native interaction between M144 and F141 is also increased upon oxidation (49% *vs.* 12% of frames, Figure 5-19). Thus, oxidation increased the total percentage of simulated frames in which an S/Ar interaction occurs by 3.7-fold (72% *vs.* 15%). Based on Boltzmann's law, this change reflects a roughly 1.6 kcal/mol increase in the free energy of the interaction upon oxidation. This value compares well to the results of our peptide experiment (0.62 kcal/mol, Table 5-3) and supports the underlying conclusion of increased interaction strength upon oxidation of the S/Ar motif, even absent hydrogen bonds. It is important to note that the simulations of the short, unoxidized peptide fragment sample unfolded conformational states that are not represented by the crystal structure (where residues 138-146 are helical) and may not be accessible in a simulation of the full-length protein. Nonetheless, the emergence of a second population of states containing the S^{Ox}/Ar motif (with Y138)—only in the oxidized simulation—motivated experiments to explore whether this subpopulation exists in the full-length protein when oxidized.

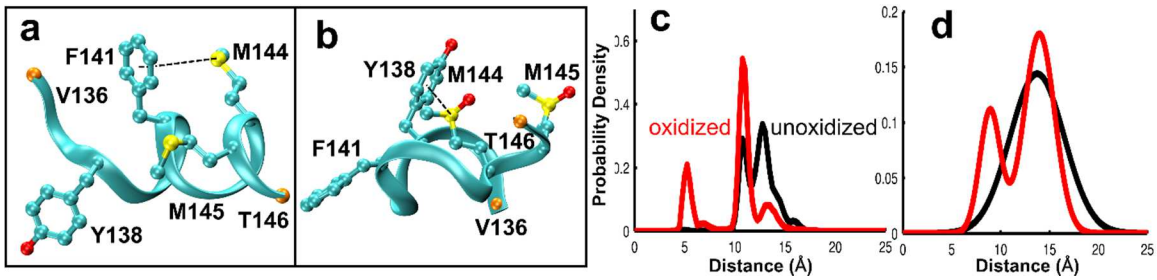

Figure 5-4. REMD and EPR measurements of CaM. Structure of unoxidized apo-CaM fragment (residue 136-146, PDB:1CFD) where F141 interacts with M144 (a) compared to a representative structure of the Y138 aromatic interacting with oxidized M144 (b) from REMD. Distance distribution calculated between Cα atoms of T136/V146 from REMD (c) and best-fit models of the distance distribution from

dipolar EPR spectroscopy at submicromolar [Ca^{2+}] with maleimide spin labels at Cys residues 136 and 146 (d).

To test the effects of oxidation of CaM's C-terminal helix in the full-length protein, we used dipolar EPR spectroscopy to detect intramolecular structural perturbations at submicromolar [Ca^{2+}]. The intramolecular distance distributions detected by EPR are shown in Figure 5-4d. As shown in Figure 5-19, the EPR spectrum of the unoxidized protein was best fit to a single broad Gaussian distance distribution, centered at 13.7 Å, with a width of 6.5 Å. After methionine oxidation, the data were best fit to a two-population model in which one population is centered at a similar distance to that observed in the absence of oxidation (14.0 Å), except that the width is narrower (3.7 Å), and there is a new population at shorter distance (8.9 Å) with an even narrower width (2.5 Å). In several respects, this confirms the predictions from MD simulations (Figure 5-4c): the long-distance population becomes narrower, and a new well-ordered short distribution emerges. The EPR distances and widths are slightly greater than those predicted by MD simulation, as expected since our MD simulations report the distances between Cα atoms, while EPR distances are between nitroxide groups at the ends of flexible side chains. EPR spectra do not directly detect C_α-C_α distances, but changes in such distances have been shown to correlate well with EPR data(223). The convergence of the simulated and experimental results strongly suggests that upon oxidation of CaM a new S^{Ox}/Ar interaction forms between either M144/Y138 or M145/Y138. Work still remains to definitively show that this minor component in the overall accessible conformational space (Figure 5-4c and Figure 5-4d) is

responsible for disruption of the Y138/E82 hydrogen bond and alters the protein's function.

5.4.5 Oxidation of LTα stabilizes intra-molecular Met-aromatic interactions, diminishing binding and ablating function

We investigated the effects of oxidation on the bioactivity and binding of LTα and TNF in live cells. We have previously shown that the interaction between LTα and TNFR1 is stabilized by a methionine-aromatic interaction via M120 of LTα and W107 of TNFR1. Mutation of M120 to alanine interrupts ligand binding, resulting in a >10 fold loss in ligand function(175). Thus, we hypothesized that the increased strength of the S/Ar interaction upon oxidation should stabilize binding via the M120/W107 interaction. Western blot analysis (Figure 5-5a) showed that untreated LTα and TNF efficiently induced downstream signaling, as has been definitively established. Surprisingly, LTα pretreated with H_2O_2 failed to induce IκBα degradation.

In order to isolate the impact of oxidation of M120 on LTα function and binding, we mutated the methionines at residues 20 and 133 to remove their susceptibility to oxidization (see Methods for details). This mutant ligand—denoted here as M120 or $M^{Ox}120$ when oxidized—triggered IκBα degradation in the unoxidized form to the same extent as wild-type (indicating that two other mutated methionine residues, M20 and M133, are not important for activity). Site-specific oxidation ($M^{Ox}120$) rendered LTα inactive (Figure 5-5a). Co-immunoprecipitation experiments explain this loss in function as a result of lost binding of the $M^{Ox}120$ ligand to TNFR1 (Figure 5-5b). Thus, we conclude that oxidation of LTα inhibits its

activity by disrupting the critical M120-W107 methionine-aromatic interaction, thereby preventing binding to TNFR1.

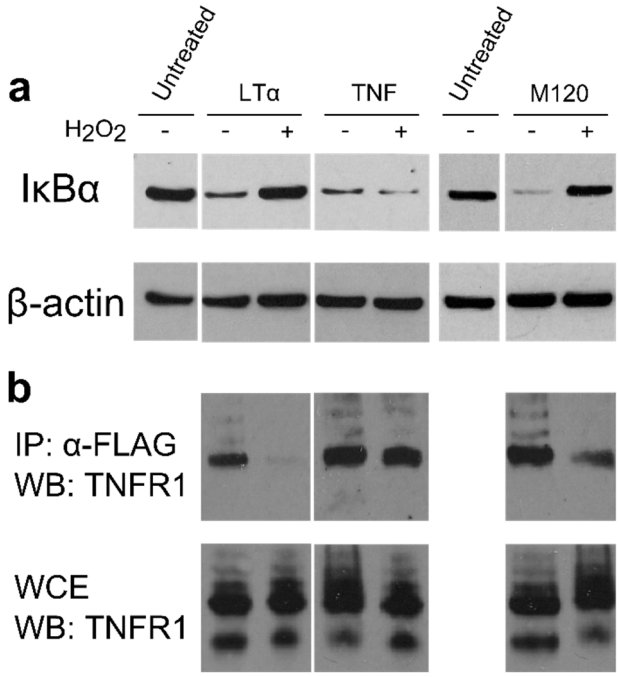

Figure 5-5. Oxidation of LTα, but not TNF ablates its interaction with TNFR1. Western blot analysis of IκBα degradation in response to treatment with oxidized (+) and unoxidized (-) LTα and TNF (a). LTα bioactivity is ablated after exposure to oxidative stress. This effect is not observed in TNF, where oxidized and unoxidized ligand trigger IκBα degradation to the same extent. Exposure to oxidative stress similarly prevented M120 LTα from triggering IκBα degradation. Co-immunoprecipitation of TNFR1 with oxidized (+) and unoxidized (-) ligands (b). LTα efficiently pulls down TNFR1 when untreated. Treatment of LTα under oxidative stress causes dramatic reduction in the amount of receptor bound. TNF is again unaffected by oxidative stress. The LTα M120 mutant again behaves the same as wild-type, indicating that oxidation of M120 is responsible for the loss of binding.

To explore the molecular basis for this loss in binding, and to explain this apparent contradiction (decreased binding despite increased S/Ar interaction strength), we used molecular dynamics simulations and quantum calculations. Analysis of the ligand/receptor crystal structure (1TNR) revealed aromatic residues in the ligand (Y96 and Y122) that are near to and on the same chain as M120 (Figure 5-6a). Given their spatial proximity, it is likely that M120 forms S/Ar contacts

with either or both of these tyrosines. MD simulations of the unbound ligand showed this to be the case in approximately 70% of the simulated frames (the M120-Y122 interaction was approximately twice as frequent as the M120-Y96 interaction). Oxidation of M120 increased the interaction strength of M120 with Y96—again using the Boltzmann equation we calculate an increased affinity of 0.35 kcal/mol. This value is lower than that described above for CaM, but once again is consistent with our general conclusion that oxidation strengthens S/Ar interactions. Interestingly, there was no oxidation-induced change in the frequency of M120/Y122 contacts. These data raise the possibility that Y122 and Y96 interact differently with M120 under oxidative conditions. We confirmed that hydrogen bonding was not a major factor in the interaction (Figure 5-20). We again used the simulations to generate an ensemble of configurations for quantum energy calculations. A snapshot from the oxidized ensemble is shown in Figure 5-6b. As was the case with our calculations on the non-hydrogen-bonded ensemble of DMS/DMSO-phenol configurations, oxidation increased the strength of the S/Ar interaction by 1-2 kcal/mol (Figure 5-6c).

We hypothesized that the strengthened M^{Ox}120/Y96 interaction could lock the ligand in a configuration that prevents M^{Ox}120/W107 interaction, thereby interrupting binding. To test this, we first needed to show that the addition of a sulfonyl oxygen to M120 in the crystal structure binding configuration does not itself destabilize the binding pocket by steric overlap or electrostatic repulsion. We first simulated the unoxidized crystal structure of the ligand-receptor complex. Figure 5-6d highlights the stability of the M120/W107 interaction, and shows the

infrequent instances of M120 interaction with either Y122 or Y96. We then started a simulation of the ligand-receptor complex in a configuration in which the M^{Ox}120/Y122 pair was pre-formed (using a configuration generated from the unbound ligand simulation). Y96 was allowed to remain in its receptor backbone binding position. The binding cavity organization reverted to that of the crystal structure configuration after 50ns (Figure 5-6d) and was stable throughout the remainder of the simulation (Figure 5-21). Therefore, we conclude that loss of ligand-receptor binding is not caused by intrinsic steric clashes with M^{Ox}120 that disrupt the binding pocket. We also conclude that M^{Ox}120/Y122 interactions do not prevent M^{Ox}120/W107 interactions and ligand binding.

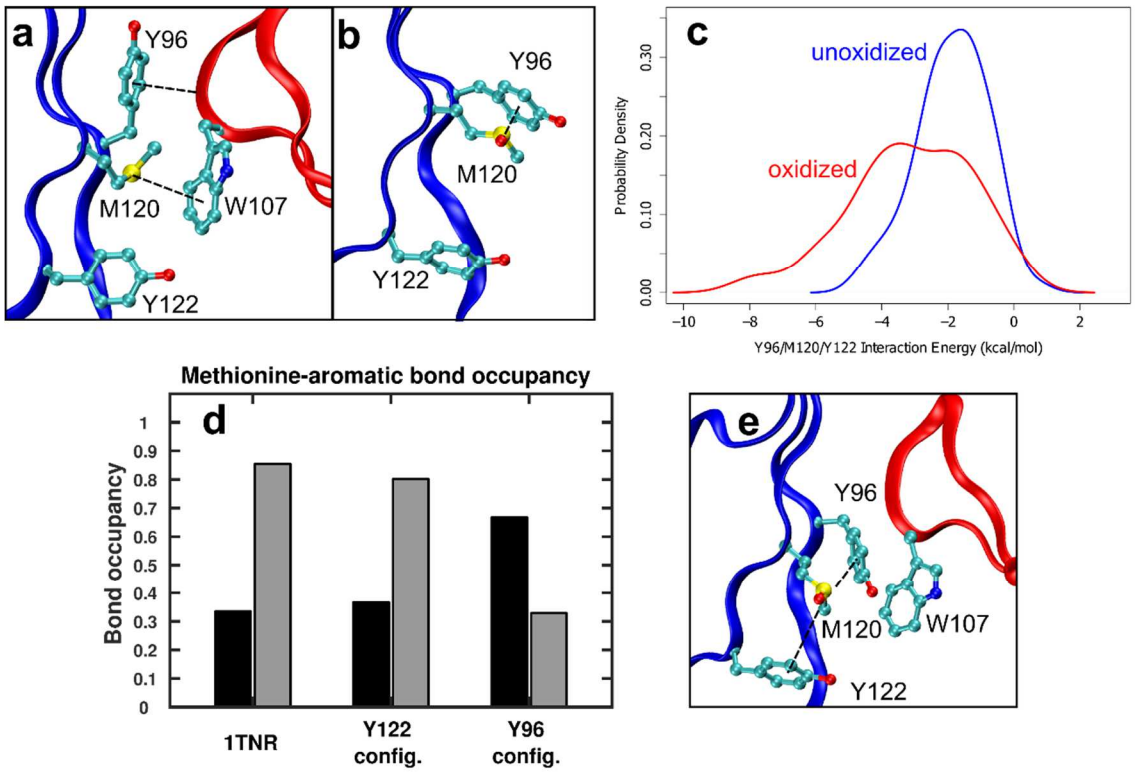

Figure 5-6. Molecular dynamics simulations of LTα with M120 oxidized show that competitive interaction of M120 with Y96/Y122 prevents its interaction with W107. In the receptor bound state, Y96 is folded upward so that it interacts with the backbone of the receptor, allowing M120 to form a stable methionine-aromatic interaction with W107 (a). When Met120 is oxidized, it draws Y96 downward so that it protrudes into the binding pocket (b). The histogram of the interaction energy between M120 and Y96/Y122 calculated from 128 structures taken from the MD simulations shows enhanced interaction due to oxidation. The histogram was smoothed with the Gaussian kernel-smoothing function "density" of the program "R" (c). The bond occupancy of the M120-Y96/Y122 (black) and M120-W107 (gray) interactions is shown for 3 systems: the unmodified crystal structure (1TNR), the M120-Y122 interacting configuration, and the M120-Y96 interacting configuration (d). M120 interacts stably with W107 in 1TNR. In the M120-Y122 interacting system, M120 interacts somewhat more with Y96/Y122, but still primarily with W107. In the M120-Y96 interacting system, the bond occupancy is reversed - that is, M120 interacts primarily with Y96/Y122 and the W107 interaction is blocked. A snapshot of the Y96 interacting system with Y96 blocking the M120-W107 interaction is shown (e).

We then started a second oxidized ligand-receptor simulation, this time with a pre-formed M^{Ox}120-Y96 pair. We observed two distinct effects of oxidation, both of which are consistent with loss of receptor binding. In two of the three chains (of the symmetric ligand trimer), M^{Ox}120 remained stably bound to Y96, preventing it from forming the critical S/Ar motif with W107 (Figure 5-6d) and also preventing Y96 from binding the receptor backbone. In these cases, the M^{Ox}120/Y96 pairing (Figure 5-6e), along with the surrounding binding pocket, remained stable throughout the simulation. In the remaining chain, Y96 released from M^{Ox}120, and in this process disrupted the binding pocket while ejecting the receptor. Collectively, the results suggest that increased stability of the M^{Ox}120/Y96 pair prevents the critical M120/W107 interaction and destabilizes the bound state.

5.5. Concluding Remarks

Oxidative stress plays a prominent role in a number of normal and pathological biological functions. However, the precise chemical and physical mechanism through which oxidative modification of proteins influences their structures and functions is largely unknown. We have shown that oxidation of methionine strengthens the methionine-aromatic interaction motif, independent of hydrogen bonding, by at least 0.5 kcal/mol and up to 1.5 kcal/mol. In the vast majority of instances in the PDB and CSD as well as the two proteins studied here in detail, the aromatic group does not form a stable hydrogen bond with the sulfoxide due to solvation of both the donor and acceptor by water. Hydrogen bonding may further enhance the interaction in hydrophobic and aprotic environments, however we do not observe that in our two test cases where the motif is solvent exposed. In LTα-TNFR1 and CaM, we have shown that competing interactions between methionine sulfoxide and nearby aromatic residues contributes to the modulation of protein structure and function.

To conclude, non-covalent interactions are the cornerstone of biological molecular recognition events. For bioactive small-molecule development, which exploits these interactions, sulfur is the third most commonly incorporated heteroatom in pharmaceuticals next to nitrogen and oxygen.(224) The sulfoxide-aromatic interaction provides a new handle for tuning affinities of small molecules for chemical probe and therapeutic development as well as altering protein function. Moreover, the dynamic nature of methionine oxidation provides a reversible switch that can be employed for introducing responsive molecules to

changes in redox environment. The energy range of these altered interactions corresponds to twofold to tenfold change in the equilibrium constant, which together with the ambivalent character of sulfoxide functional groups, the dynamic nature of their formation, and their prevalence in biology and pharmaceutics, offers medicinal chemists and chemical biology a useful tool to probe biological systems.

5.6. Methods

5.6.1 Structural bioinformatics analysis of the Protein Data Bank

A non-redundant (sequence identity <90%) subset of the Protein Data Bank (PDB) containing DMSO molecules was analyzed using the Biopython toolset and a custom Python script adapted from our previous study(175). Distances were defined between the DMSO sulfur and the center of the aromatic ring. Distance data were collected up to a cutoff of 20 Å. Hydrogen bonds were defined as having a heavy-atom donor to sulfonyl oxygen distance of < 3.5 Å. For the radial density function (RDF), the distance from a DMSO to its nearest aromatic group was binned and divided by shell volume. Each RDF was normalized by the relative population of amino acids in the analyzed PDB files (divided by 9.25% for F, Y, W, 22.47% for L, I, V, and by 100% for all amino acids). The resulting plots were normalized by the mean value at the long distance, non-interacting region of the "All Amino Acids" RDF to shift the bulk density to 1 and to cast the y-axis as an enrichment factor.

5.6.2 Structural bioinformatics analysis of the Cambridge Structural Database

Searches were executed in the Conquest program of the Cambridge Structural Database (CSD version 5.35, 2014 release), and structural analyses

were performed using the Mercury program (v 1.5). The distance was defined as in the PDB. C-CH_2-C was used as a non-interacting analog to C-S-C, following the previous CSD analysis by Zauhar, et al.(176) The sulfur (or carbon in control) atom to aromatic distance was constrained to 0-10 Å. For the radial density function (RDF), the distances from each DMSO (or C-CH_2-C) to all aromatic groups were binned and divided by shell volume, then normalized by the total number of contacts. The resulting RDFs were shifted to 1 as in the PDB analysis, by normalizing to the value at the flat region of the C-CH_2-C RDF. A total of 20630 DMSO-aromatic pairs were found in 840 structures and 3093875 C-CH_2-C-aromatic pairs were found in 72745 structures.

5.6.3 ABF simulations of DMSO and aromatic groups in three solvents

Simulations were performed using the Adaptive Biasing Force (ABF) module in NAMD 2.9 using the CHARMM 36 generalized forcefield. The adaptive biasing force (ABF) module was used so that the system could overcome free energy barriers and fully sample all conformational states. Parameters for DMS were adapted from those for ethylmethylsulfide. The distance between the DMSO thioether and the center of mass of the 6-membered ring of phenol, or indole was used as the reaction coordinate of the mean force calculation. The system potential along the reaction coordinate was negated by the adaptive biasing force to simulate a flat free energy landscape. Each system was solvated in a ~45 $Å^3$ periodic box of TIP3P water, hexane, or ethyl acetate, for a total of 18 systems. The adaptive biasing potential was applied between 2.5 and 14 Å with a binwidth of 0.1 Å and simulations were carried out for at least 7.5 x 10^6 steps. All other

simulation parameters were set as in our traditional MD (see Molecular dynamics simulations of LTα and TNFR1 methods). The calculated PMF was not used in our analysis.

5.6.4 Quantum calculations

The interaction energy between model compounds was investigated with quantum mechanical calculations performed in the gas phase. The reduced and oxidized states of methionine were modeled by dimethyl sulfide (DMS) and dimethyl sulfoxide (DMSO), respectively; the side chains of phenylalanine, tyrosine, and tryptophan were modeled by benzene, phenol, and indole. The interaction energy between compounds A and B was defined as:

$$E(AB)_{int} = E(AB)_{complex} - E(A) - E(B) \quad (1)$$

All energies were obtained from fully unrestrained structure optimizations carried out with Gaussian 09(225) at the MP2/6-311+G(d,p) level and account for basis set superposition error(226). Additional data computed at the M06-2X/6-311+G(d,p)(227) level are reported in Table 5-4. These two levels of calculation were chosen because we previously showed that they bracket the interaction energy calculated at the CCSD(T)/6-311+G(d,p) level(175). Notice that for each complex several minima were characterized, and the data is reported only for the lowest energy one.

The dispersion energy contribution to the complex formation was calculated as in Ref. (175) by taking the difference between the interaction energy (eq 1) computed at the MP2 and Hartree-Fock (HF) levels. In both cases the same basis

set was employed, and the HF energies were calculated as single point on the MP2 optimized structures.

The effect that the variety of conformations adopted in solution has on the interaction energy was investigated by averaging the interaction energies of 128 structures randomly sampled from the minimum (sulfur – aromatic distance between 4 – 6 Å) of the ABF simulations in ethyl acetate described below. Upon removal of the solvent, the instantaneous interaction energy was calculated at the MP2/aug-cc-pVDZ level using eq. 1 without any additional structure optimization.

A similar procedure was employed to investigate the interaction energy between the side chains of M120, Y96, and Y122 in LTα. From the MD simulations described below, 128 structures were randomly selected and the average interaction energy calculated at the MP2/aug-cc-pVDZ level as:

$$E(M_{120}Y_{96}Y_{122})_{int} = E(M_{120}Y_{96}Y_{122})_{complex} - E(M_{120}) - E(Y_{96}) - E(Y_{122}) \quad (2)$$

The side chains were truncated at the C_β-C_γ bond and the missing valence was saturated with a hydrogen atom. Upon removal of the rest of the protein and the solvent and without any further optimization, the interaction energy was calculated at the MP2/aug-cc-pVDZ level and corrected for the basis set superposition error.

For the calculations on the ethyl acetate simulations described above, the Natural Bond Orbital(228) (NBO) charges were calculated and averaged over all 128 structures. The NBO localization scheme was tested along Mulliken(229) localization over a number of different basis sets of increasing size. Because the

results showed a strong dependence of the Mulliken charges on the basis set size(230) while NBO charges did not, the NBO localization scheme was preferred.

5.6.5 Peptide Synthesis

To study the appropriate pair sequences in a peptide chain, the un-oxidized amino acid Met or oxidized Met was inserted into the sequence: a) Tyr-Gly-Gly-Ser-Ala-Ala-Glu-Ala-***Aromatic***-Ala-Lys-Ala-**Met**-Ala-Arg-NH2, b) Tyr-Gly-Gly-Ser-Ala- Ala-Glu-Ala-***Aromatic***-Ala-Lys-Ala-**Met (ox)**-Ala-Arg-NH2. The peptides were assembled on Fmoc-PAL-PEG-PS resin by Fmoc chemistry using a PE Biosystems PioneerTM protein synthesis system. Single Met oxidation was accomplished by incorporation of Fmoc-Met (ox)-OH during synthesis. Standard *N*-[(dimethylamino)-1*H*-1,2,3-triazolo[4,5-*b*]pyridin-1-ylmethylene]-*N*-methylmethanaminium hexafluorophosphate N-oxide (HA TU)/ *N,N*-diisopropylethylamine (DIEA) (1/2.4 eq.) activation, in 1-methyl-2-pyrrolidinone (NMP), was applied. Fmoc deprotection was achieved with 20% piperidine in NMP. The final release of the peptides, with removal of the side chain protecting groups, were accomplished by exposure of the peptide-resin to 82.5% trifluoroacetic acid (TFA), 5% phenol, 5% thioanisol, 2.5% 1,2-ethanedithiol, 5% water (Reagent K). The peptides were precipitated with cold methyl-*t*-butyl ether, vortexed, centrifuged, decanted, and dried over argon. The dried peptides were dissolved in degassed water and purified by high-performance liquid chromatography (HPLC) using a reversed- phase C8 HPLC column. Peptide elution was achieved with a linear gradient from 0 to 34% B (95% acetonitrile / 5% water / 0.1% TFA) in 40 min at a flow rate of 2.5 mL/min with detection at 280 nm using a System Gold

Beckman Coulter system. The HPLC fractions were collected and analyzed by mass spectrometry (MS).

5.6.6 Peptide Scaffold Design

The peptide scaffold utilized for defining the energetic impact of oxidation on Met-Aromatic interaction had a number of specific design elements. The helical content was optimized to reside within a range that enabled sensitive detection of its change by CD. The capping box motif at the N-terminus is the sequence Ser/Thr-X-X-Glu/Gln and is a helix stop signal(231). This stop signal has Ser or Thr as the N-cap and a Glu or Gln residue at position i+3, specifically; the sequence Ser-Ala-Ala-Glu is the capping motif in each of the peptides of the double mutant cycle. To this capping box, the N-terminus had a tyrosine added for concentration determination. The C-terminus was blocked by changing the COO- to a CONH2 to mediate this effect of dipole destabilization and to increase helical propensity(232).

5.6.7 Electrospray ionization (ESI)-MS

The peptides were analyzed on a LC/MSD ion trap (Agilent). ESI-MS spectra were acquired in positive ion mode. The solvent contained 40 % acetonitrile and 0.1 % formic acid. 10 to 30 μL sample were directly injected at a flow rate of 10 μL/min with a source temperature of 300 ˚C. The applied spray voltage was 3500 V, and the skimmer voltage 40 V. MS scans were acquired over an m/z range of 200 to 2000. The scan for the native mass 1499.69 Da of the sequence Tyr-Gly-Gly-Ser-Ala-Ala-Glu-Ala-**Phe**-Ala-Lys-Ala-**Met**-Ala-Arg, shows the single charged ion with *m/z* 1500.0 and the double charged ion *m/z* 750.7. The

scan for the Met(O)-Phe sequence pair (1515.69 Da) shows the singly charged ion with *m/z* 1515.7, the double charged ion *m/z* 758.4, and the triple charged ion *m/z* 505.9. The observed masses for the respective molecular ions agree with the theoretical peptide scaffold design.

5.6.8 Circular Dichroism Spectroscopy

All peptides were stored in tetrafluoroethylene (TFE) after synthesis, which was removed by evaporation using Nitrogen gas prior to use. To ensure complete removal of the TFE, the sample was then put under vacuum for one hour. The dried peptide was re-constituted in 10mM KH_2PO_4, 100mM KCl at pH 7.5, and prepared for CD data collection. All CD experiments were performed on a Jasco J-815 CD Specrometer (Annapolis, MD) using a 0.1cm quartz cuvette using 150μM peptide concentration for all samples. Concentrations of the peptide samples were determined using a Nanodrop Spectrometer. Data points were collected from 200 to 260nm in 1nm increments from -2°C to 60°C for FM and FM (ox) For YA, FA, AM, AM (ox) and AA, one data point was collected at 222nm at each 0.5°C or 2°C change as temperature increased from - 2°C to 60°C. Cooling melts were also collected on all peptides as temperature decreased from 60°C to -2°C. All collected data points were averaged from 3 acquisitions of the recorded ellipticity.

5.6.9 Analysis of CD data

To extract the free energy of interaction from the temperature dependence of the CD, spectra were collected from the lowest experimentally accessible temperature (-2^{o}C) to a temperature beyond which there were no observable changes in spectral shape for all peptides (60^{o}C). The spectra are given in Figure

5-13. Following Greenfield(216), we used the signal, Θ, at 222nm to report on changes in peptide structure. This wavelength was chosen because it reflects helical content and is also the wavelength at which the overall change in ellipticity is greatest across the temperature ramp. Following the same rationale we used previously(233), the CD signal is given by:

$$\Theta = (\Theta_{initia} + K\Theta_{final})/(1 + K) \quad (3)$$

where $\Theta_{initial}$ is the value at 222nm recorded at -2°C, and Θ_{final} is the value at 222nm recorded at 60°C. Because $K = e^{-\Delta G/RT}$, we rewrite this equation as:

$$\Theta(T) = (\Theta_{initial} + e^{-\frac{\Delta G}{RT}}\Theta_{final})/(1 + e^{-\frac{\Delta G}{RT}}). \quad (4)$$

We then fit the temperature dependent data, $\Theta(T)$, by substituting the Gibbs-Helmholtz equation into equation 4,

$$\Delta G = \Delta H_{Tm}\left(1 - \frac{T}{T_m}\right) + \Delta C_p(T - T_m - T(\ln(\frac{T}{T_m}))), \quad (5)$$

and varying the three parameters: enthalpy (ΔH_{Tm}), heat capacity change (ΔC_p), and transition temperature (T_m).

Data for Phe-Met and Pet-Met(ox) are given for each replica in Figure 5-14. By varying the concentrations of the peptide in each of its three replicates, the measured signal varies for each replica. The three replicates are globally fit simultaneously, an approach that improves the stringency of the parameter fits for each peptide. The free energy is then extracted from the fit at the desired

temperature (T=0^{o}C in this case). The change in free energy for each leg of the double mutant cycle is reported in Figure 5-12.

5.6.10 Double Mutant Cycle

To construct a double mutant cycle, peptides were synthesized in which the aromatic residue and Met (or Met^{Ox}) was replaced first individually, then concurrently by the neutral residue alanine (Ala). The difference in ΔG between the Met-aromatic (oxidized or un-oxidized) and its respective singly substituted construct, or between the singly substituted construct and the doubly mutated construct gives a ΔΔG. The difference of the respective ΔΔG values produces a ΔΔΔG, which indicates whether the specific interaction is contributing to the stabilization of structure. ΔΔΔG is simplified here as ΔG_{int} to match the free energy of interaction reported in the reference(182) (the two expressions are thermodynamically equivalent, although Vigeura et al. did not use a double mutant cycle). If ΔG_{int} equals zero, the interaction observed is not contributing to the structural stability; if greater than zero, the interaction is stabilizing; and if less than zero, destabilizing(234-236).

5.6.11 Principal Component Analysis

Principal component analysis for each of the FM, FM^{Ox}, FA, AM, AM^{Ox}, and AA peptides data sets was carried out with the “prcomp” function of the program R (v. 3.2.1). For each data set only one of the three replicates was used. To increase the sensitivity of the analysis, we focused on the isodichroic point region by analyzing only the wavelengths between 200 nm and 210 nm (11 data points),

while the entire temperature range was included in the analysis. The correlation matrix was calculated between the mean-centered vectors of wavelengths:

$$C_{ij}=T_i(\lambda_1,\lambda_2,\ldots,\lambda_N)\cdot T_j(\lambda_1,\lambda_2,\ldots,\lambda_N)$$

The results reported in Figure 5-16 and 0 show that the first two principal components describe 94% or more of the total variance, which is consistent with the assumption that the change in molar ellipticity is dominated by only two sources of signal.

5.6.12 Replica exchange molecular dynamics of calmodulin

The replica exchange molecular dynamics (REMD) simulation was performed in NAMD 2.9 using the CHARMM22 potential parameters(237). Eleven residues of the last helix (136-146) of CaM (3CLN.pdb) were used in the all-atom point-charge force field in vacuum without change neutralization(220). Eight replicas with temperatures exponentially spaced from 300K to 600K (300, 331.23, 365.7, 403.77, 445.8, 492.2, 543.43, 600 K) were used with the initial velocities of the atoms generated by the Maxwell-Boltzmann distribution and a timestep of 1 fs. The first 10^6 steps were performed without attempting exchanges to equilibrate, then exchanges were attempted every 1000 steps (1 ps) with an acceptance rate ~20%. Coordinates were taken every 100,000 steps (100 ps). 78,810 frames were taken for the unoxidized peptide and 74,400 frames for the oxidized peptide, corresponding to a total simulation time per replica of 985 and 930 ns, respectively. Only the replicas at 300 K were used in the analysis. Methionine-aromatic interactions were identified as having a distance of <7 Å and an angle less than

60°, consistent with previous definitions(175, 176). Hydrogen bonds were cutoff at <2.5Å from hydrogen to acceptor.

5.6.13 Dipolar EPR spectroscopy of spin-labeled calmodulin.

A mammalian CaM mutant, with V136 and T146 both mutated to Cys, was prepared by site-directed mutagenesis (QuikChange II kit, Agilent, Santa Clara CA), confirmed by DNA sequencing, expressed and purified as described previously(211), and dialyzed overnight at 4°C against 10mM NaCl, 10mM Tris (pH 7.0). Spin-labeling with maleimide spin label (MSL, N-(1-oxyl-2,2,5,5-tetramethyl pyrrolidinyl) maleimide, Toronto Research Chemicals, Canada) was carried out by incubating 120 μM CaM with 480 μM MSL in CaM buffer (10 mM NaCl, 10 mM Tris, 5 mM EGTA, pH 7.0) for two hours at 22^{o} C (followed by overnight dialysis against CaM buffer to remove unreacted label), resulting in complete labeling of the two Cys, as shown by mass spectrometry. To oxidize methionine side chains, spin-labeled CaM was incubated in 500 mM hydrogen peroxide for 30 min, followed by dialysis into CaM buffer. As shown previously under similar conditions(211), mass spectrometry verified that all of the nine methionine residues of CaM were oxidized. X-band (9.5 GHz) EPR spectra of 200 μM CaM (in CaM buffer plus 10% glycerol) were acquired at 200^{o} K with a Bruker ER500 spectrometer, using 1 G modulation amplitude and sub-saturating microwave power (0.63 mW). EPR spectra were analyzed to determine the distribution of distances between the two spin labels, as described previously(108).

5.6.14 Ligand preparation and treatment

Plasmids encoding LTα and TNF expressing an N-terminal FLAG tag, downstream from an inducible T7 promoter were subcloned using standard cloning techniques. Plasmids were transformed into chemically competent BL21 bacteria, plated on LB agar plates, and cultured in LB to an OD600 of ~0.5. Cultures were then cooled to 18°C, induced with 0.5 mM isopropyl β-D-1-thiogalactopyranoside, and grown for 18 hours. The bacteria suspension was centrifuged, then lysed by sonication in ice-cold PBS. The lysate was column purified using anti-FLAG M2 Affinity Gel (Sigma) according to the manufacturer protocol, dialyzed exhaustively against MilliQ H_2O, and then lyophilized. FLAG-LTα, as prepared in our laboratory, contains 4 methionine residues, of which M120 and M133 potentially play structural and functional roles in the ligand-receptor complex. M133 is buried between two folds of a β-sheet, and its precise functional role, if any, has not been established. For the LTα-M120 mutant, we mutated M133 to valine and M20 to alanine in order to match the homologous residues found in Bos Taurus LTα, which shares 73% sequence identity and 81% sequence similarity (Sequence Manipulation Suite), but lacks methionines except for its N-terminus. TNF, which also binds to and activates TNFR1 with similar potency(15) was used as a control.

Oxidative stress was applied by dissolving 8 µg of ligand in buffer containing 10 mM HEPES, 100 mM KCl, 1 mM MgCl, 1 mM CaCl, then adding 100 mM H_2O_2 to a total volume of 100 uL. The oxidation reaction was allowed to proceed for 18 hours at room temperature, then stopped by removing H_2O_2 in 2 sequential stages using Zeba 7KDa molecular weight cutoff spin columns.

Removal of H_2O_2 was confirmed by Amplex red assay, and the residual concentration of H_2O_2 was determined as insufficient to induce autophagy. We measured tryptophan fluorescence to confirm that oxidation does not lead to gross unfolding of LTα, finding no shift in the emission spectrum when excited at 280 nm (Figure 5-22).

5.6.15 Western blot analysis of IκBα

HEK 293 cells were maintained in DMEM supplemented with 10% FBS, penicillin/streptomycin, and 2 mM L-glutamine. Confluent cells were split at 1:12 into 6-well plates and used for experiments on day 3. Untreated and oxidized ligands were added to cells to final concentrations of 200 ng/mL and 20 ng/mL for LTα and TNF respectively, and incubated for 20 minutes at 37 °C. Cells were then washed once and gently sheared from the plate with ice-cold PBS, then centrifuged and resuspended in radioimmunoprecipitation assay (RIPA) lysis buffer. Cell lysates were normalized to equal protein concentrations, and 60 µg were loaded onto 4-12% Bis-Tris gradient gels for Western blot analysis. IκBα was detected using horseradish peroxidase (HRP) conjugated rabbit α-IκBα (Cell Signaling Technology, #9242) and α-Rabbit IgG (Amersham).

5.6.16 Co-immunoprecipitation

Co-immunoprecipitation was performed using anti-FLAG M2 agarose beads (Invitrogen) according to the manufacturer instructions. Briefly, HEK 293 cells were split at 1:12 into 15 cm plates and transfected with 8 µg of plasmid encoding TNFR1 (pCMV6-XL5-TNFR1) on day 1 by calcium phosphate transfection. On day 3, cells were lifted by shearing, washed once, and

resuspended in ice-cold PBS at ~10^6/mL. LTα and TNF were added at 12 and 25 ng/mL respectively, and the cells were incubated for 30 minutes at 4 °C while rocking. Cells were then washed 3 times in ice-cold PBS and resuspended in RIPA lysis buffer, then analyzed by Western blot. TNFR1 was detected using rabbit α-TNFR1 (Abcam, ab19139) and α-rabbit secondary, as described above.

5.6.17 Molecular dynamics simulations of LTα and TNFR1

We carried out molecular dynamics simulations of oxidized or unoxidized LTα in its unbound state and unoxidized in complex with TNFR1 using the structure solved by Banner et al. (1TNR) as the starting configuration(8). Two additional systems, Y122 interacting config. and Y96 interacting config., were constructed in which M120 began bound to Y122 or Y96, respectively, while all other residues in the 1TNR crystal structure were left essentially unchanged (minor manipulation and steepest descent minimization was required to resolve overlap in the binding pocket). The starting configurations of M120, Y96, and Y122 in these systems were taken from the oxidized ligand simulation. Each system was solvated in a box of at least 40,000 water molecules modeled as TIP3P(238) and the charge was neutralized by adding K^+ and Cl^- ions. The isothermal-isobaric (NPT) ensemble was used along with the CHARMM36 force field(153, 239, 240) at a temperature of 303 K and 1 atm pressure, which were maintained using the Langevin piston and Nosé-Hoover(158) algorithms. Parameters for Met^{Ox} were provided by Krzysztof Kuczera(241) and adapted for use in the CHARMM36 force field. Long-range electrostatics were calculated using the particle mesh Ewald method (242) with a 1.5 Å grid spacing and 4^{th} order interpolation. Lennard-Jones interactions

were switched off at a cutoff distance of 10 Å. Each system (except the Y96 and Y122 interacting configurations) was minimized using NAMD 2.8(237) for 1000 steps, then equilibrated with Cα harmonic constraints of 1, 0.1, and 0.01 kcal/mol/Å^2 for 2 ns at each stage. Dynamic trajectories were propagated with the r-RESPA algorithm (243) with a 2 fs time step and the RATTLE algorithm (244) was applied to all covalent bonds involving hydrogen. The ligand-receptor system was simulated for ~35 ns and distance and angle analyses were averaged over the entire trajectory. The ligand-only systems were simulated for a total of ~430 ns. The first 150 ns (including relaxation) were excluded from structural analyses to allow re-equilibration of the ligand after removal of the receptor chains. The Y96 and Y122 interacting systems were equilibrated with great care before running unrestrained dynamics. Each was minimized to resolve steric clashes, then equilibrated according to the scheme shown in Table 5-9. Distances and angles were calculated from the thioether sulfur of M120 to the centers and normal vectors of the aromatic groups of Y96, Y122, and W107. Methionine-aromatic interaction cutoffs were defined as in the CaM simulations.

5.7. Supplemental Figures

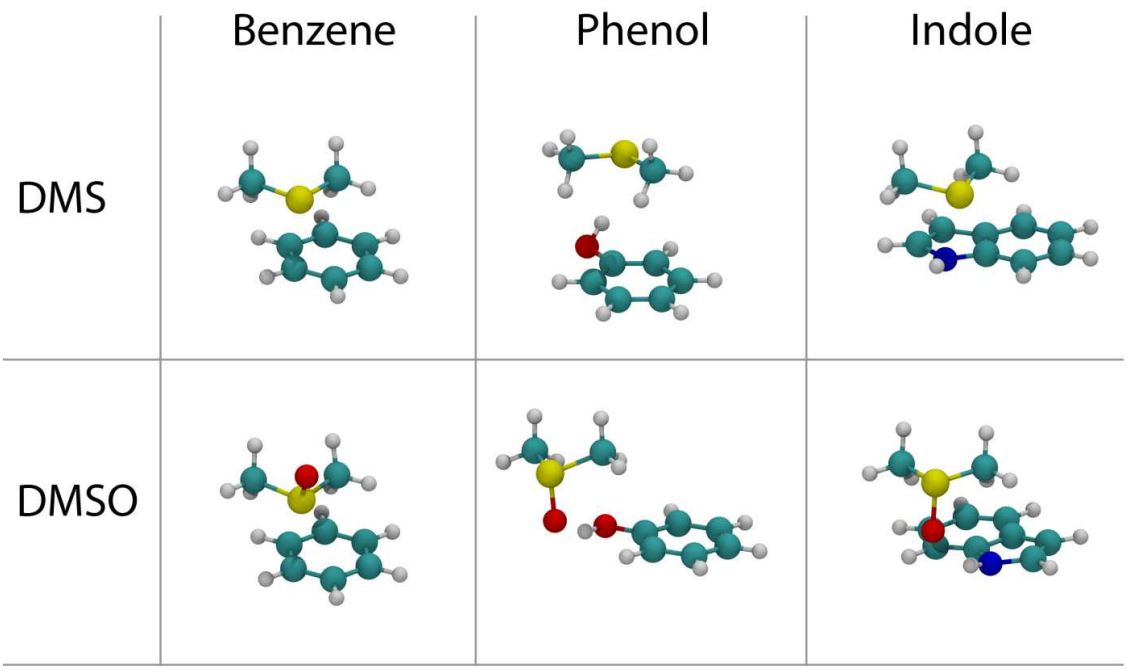

Figure 5-7. Minimum energy structures. The minimum energy structures for the complex between DMS or DMSO and benzene, phenol, and indole, calculated from full optimizations at the MP2/6-311+G(d,p) level.

Figure 5-8.

	Benzene		Phenol		Indole	
Complex	M06-2X	MP2	M06-2X	MP2	M06-2X	MP2
DMS	-4.6 (-4.0)	-6.0 (-2.4)	-8.3 (-7.3)	-9.3 (-4.9)	-7.3 (-6.3)	-9.5 (-4.7)
DMSO	-6.2 (-4.9)	-7.3 (-3.3)	-16.0 (-14.4)	-16.0 (-10.6)	-13.6 (-12.1)	-15.5 (-10.0)

Table 5-4. Interaction energies for DMS and DMSO with benzene, phenol, and indole. Computed interaction energies in kcal/mol for the complexes of benzene, phenol, and indole with DMS and DMSO (structures are shown in Figure 5-7). M06-2X and MP2 data are reported for structures fully optimized at the corresponding levels of theory with the 6-311+G(d,p) basis set. Hartree-Fock data are reported for benzene only as single point energy calculations on the MP2 optimized structures. Interaction energies corrected for basis set superposition error are reported in parenthesis.

	MP2	HF	Dispersion Energy
DMS	-6.0	2.4	-8.4
DSMO	-7.3	0.9	-8.2

Table 5-5. Dispersion energy interactions. Dispersion energy interactions are calculated in kcal/mol for the complexes of benzene with DMS and DMSO as the difference between the MP2/6-311G(g,p) interaction energies and the HF/6-311+G(d,p) calculated as single point on the MP2 minima.

	DMSO/Benzene	DMS/Benzene	DMSO	DMS	Benzene
O	-0.96		-0.96		
S	1.19	0.19	1.18	0.20	
C	-0.77	-0.70	-0.76	-0.70	
H	0.22	0.21	0.22	0.21	
H	0.22	0.21	0.21	0.19	
H	0.21	0.19	0.21	0.19	
C	-0.76	-0.70	-0.76	-0.70	
H	0.22	0.21	0.22	0.21	
H	0.21	0.19	0.21	0.19	
H	0.21	0.19	0.21	0.19	
C	-0.20	-0.20			-0.20
C	-0.21	-0.21			-0.20
C	-0.20	-0.19			-0.20
C	-0.20	-0.21			-0.20
C	-0.21	-0.20			-0.20
C	-0.20	-0.20			-0.20
H	0.21	0.20			0.20
H	0.20	0.20			0.20
H	0.21	0.20			0.20
H	0.21	0.20			0.20
H	0.20	0.20			0.20
H	0.21	0.20			0.20

Table 5-6. NBO Charges analysis of the benzene complexes with DMS and DMSO, and of the isolated species based on the MP2/6-311+G(d,p) electron density.

	Gas	EtOAc	Water
DMS	-4.7	-3.9	-3.6
DMSO	-6.2	-5.1	-4.7
ΔE_{int}	-1.5	-1.2	-1.1

Table 5-7. Effects of solvation on quantum mechanical interaction energy. The effect of solvation on quantum mechanical interaction energies has been tested for the complex of benzene with DMS and DMSO. The interaction energy in kcal/mol for the complexes optimized in gas phase at the M06-2X level was calculated in the gas phase and with single point PCM calculations to describe the effect of solvation in

EtOAc and water. The basis set employed was 6-311+G(d,p). The ΔE_{int} entry shows that the effect of solvation is less than 0.4 kcal/mol.

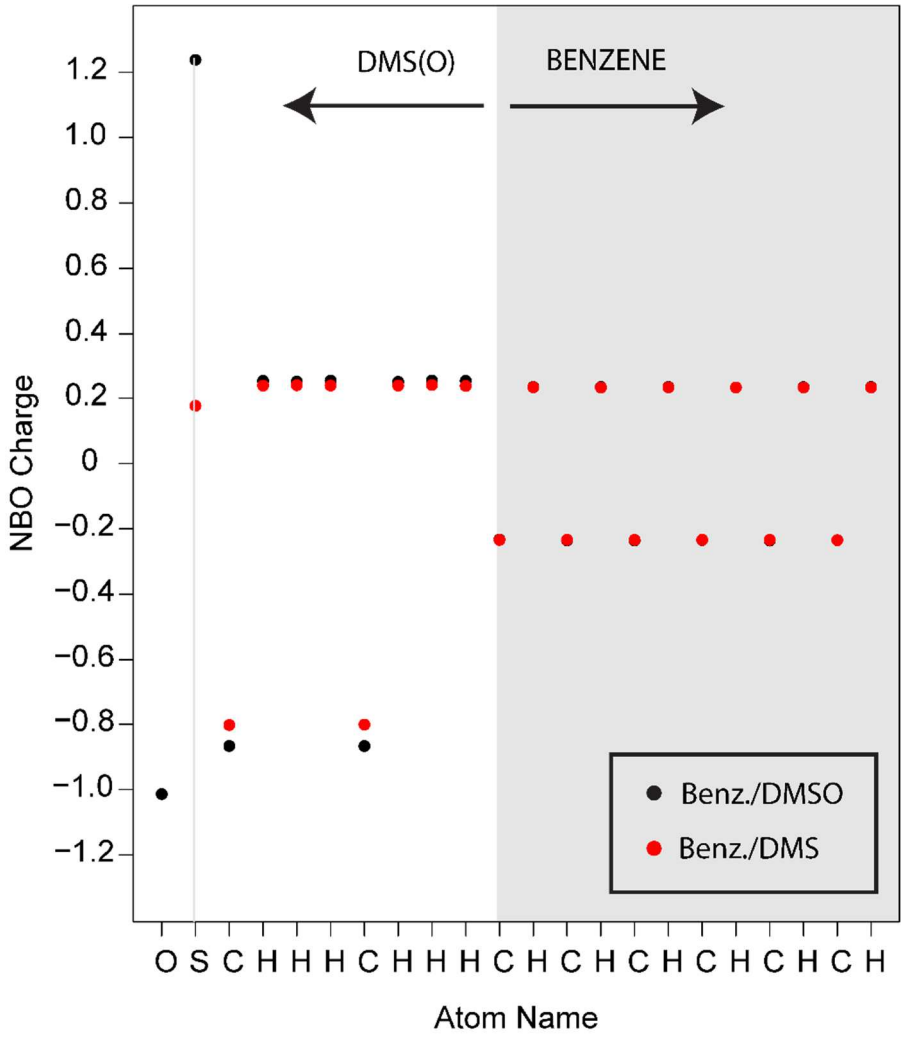

Figure 5-9. NBO average charges for the ABF simulations. NBO charges were computed as the average for the 128 structures for the simulations of DMS/DMSO and benzene in EtOAc using the MP2/6-311+G(d,p) electron density. In red the charges for benzene/DMS are reported, and in black for benzene/DMSO.

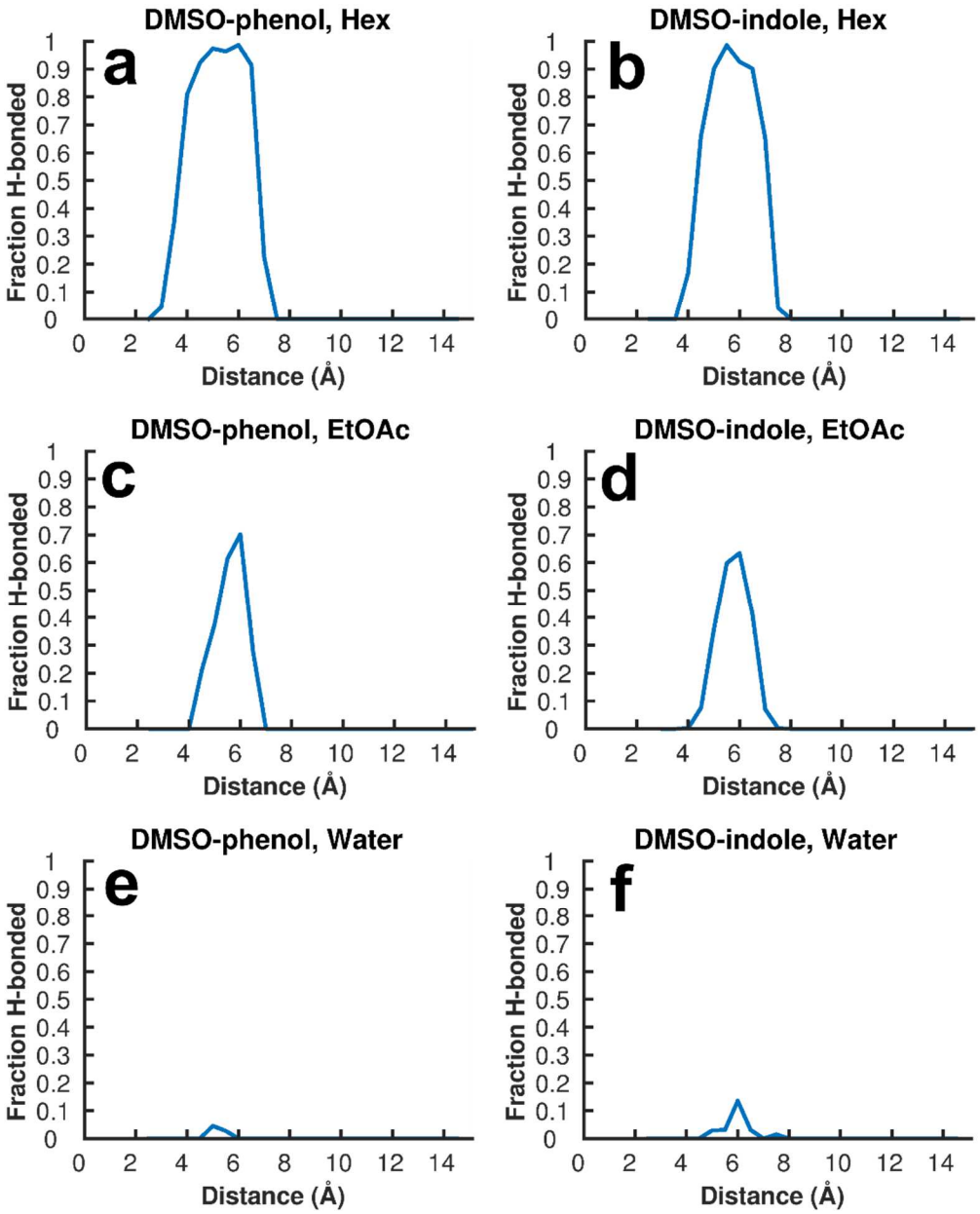

Figure 5-10. Fraction of structures in which the DMSO sulfonyl accepts a hydrogen bond from the aromatic. Structures were extracted from the ABF simulations of DMSO and aromatic amino acid analogs in three solvents. The fraction of structures that are hydrogen bonded (H-acceptor distance < 2.5Å) along all sulfur-aromatic distances is plotted. Hydrogen bonding occurred in nearly all configurations that were in range in hexane (a, b), fewer configurations in EtOAc (the frequency of hydrogen bonding was reduced by ~60%) (c, d), and almost none of the configurations in TIP3P water (e, f). EtOAc is able to accept hydrogen bonds from the aromatic group and TIP3P is able to donate and accept hydrogen bonds, which results in the lower prevalence of bonding between the DMSO and aromatic group.

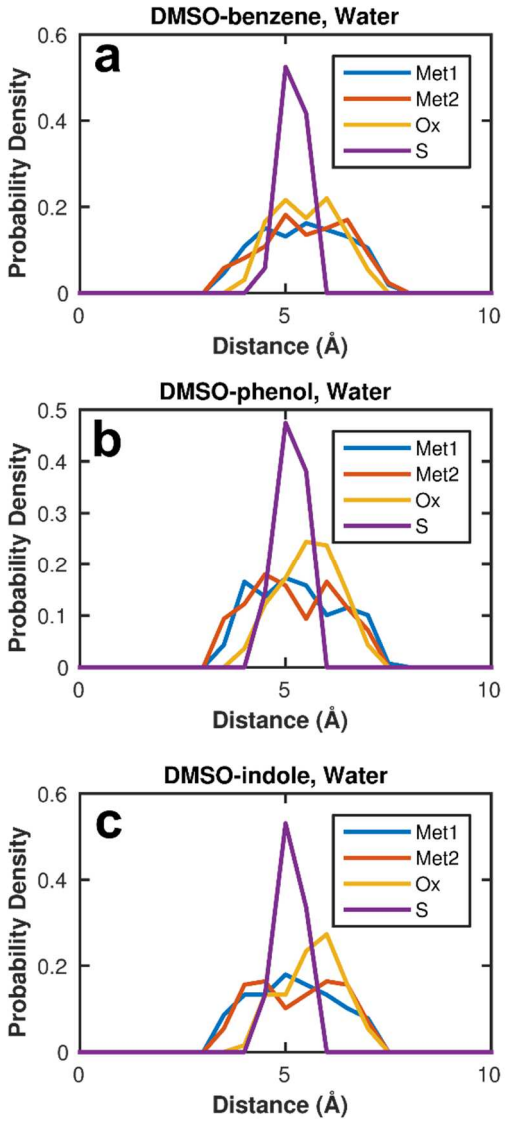

Figure 5-11. Histogram of distances from each DMSO atom to the center of the aromatic ring. Non-hydrogen-bonded DMSO-aromatic pairs from the ABF simulations were analyzed and show no strong bias for the methyl groups to interact with the aromatic ring. Benzene (a), phenol (b), and indole (c).

Peptide	***Abbreviation***	***Construct Sequence***
Phe-Met	FM	YGGSAAEA-**F**-AKA-**M**-AR-NH_2
Phe-Met (ox)	$FM_{(ox)}$	YGGSAAEA-**F**-AKA-**M (ox)**-AR-NH_2

Phe-Ala	FA	YGGSAAEA-**F**-AKA-**A**-AR-NH_2
Ala-Met	AM	YGGSAAEA-**A**-AKA-**M**-AR-NH_2
Ala-Met (ox)	$AM_{(ox)}$	YGGSAAEA-**A**-AKA-**M (ox)**-AR-NH_2
Ala-Ala	AA	YGGSAAEA-**A**-AKA-**A**-AR-NH_2

Table 5-8. All peptides used in CD thermal studies , their appropriate abbreviation and their sequences. Only residues 9 and 13 were varied, and these positions are shown in bold.

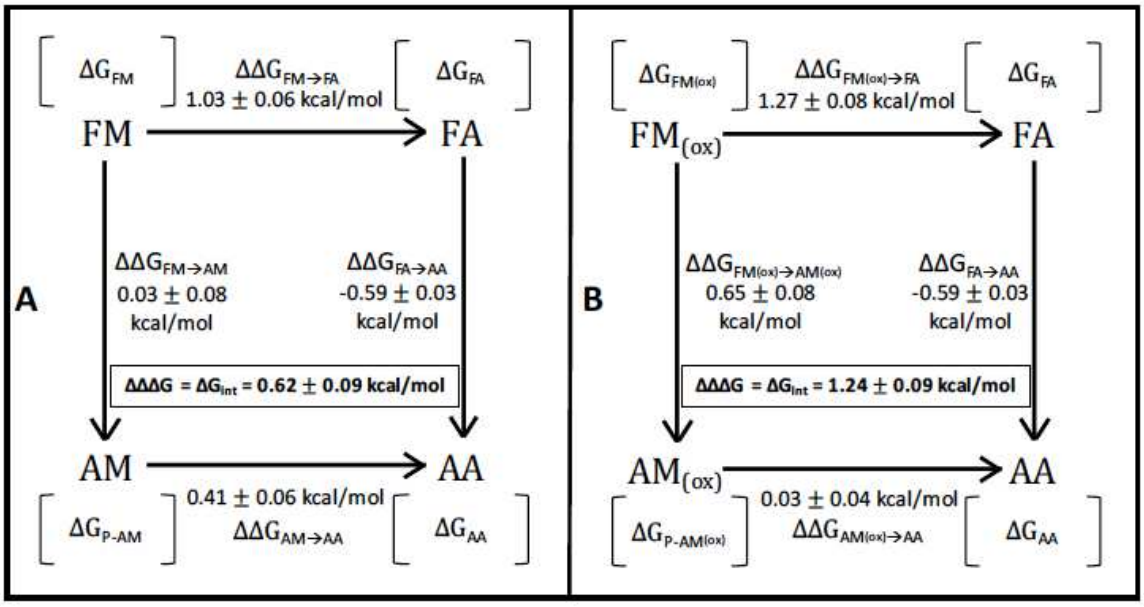

Figure 5-12. Double-mutant cycle. Thermodynamic double mutant cycle of FM (a) and $FM_{(ox)}$ (b) peptides. Nomenclature is: Wild-type peptide (FM and $FM_{(ox)}$), singly mutated peptide (FA, AM and $AM_{(ox)}$) and doubly mutated peptide (AA). F, M and A represent phenylalanine, methionine (un-oxidized or oxidized) and alanine, respectively. Free energy of each peptide denaturation is represented as ΔG at each step in the cycle. ΔΔG values are determined by the difference in ΔG denaturation values of peptides at 0°C, which were used to determine the ΔΔΔG. For simplicity, and as described in the Methods, we assign the nomenclature ΔG_{int} to reflect the change in interaction free energy between Met/Phe and $Met_{(ox)}$/Phe (S^{Ox}/Ar- S/Ar = 1.24 - 0.62 = 0.62 kcal/mol). Thus there is a doubling of the strength of the interaction upon oxidation. Error was calculated through a total differential approach, where the derivatives of the GHE with respect to ΔH, ΔCp and Tm were calculated. The error for each thermal denaturation ΔG is the sum of the products of each derivative and their respective individual error values. Error was then calculated with ΔG values for each side of the thermodynamic cycle for ΔΔG and ΔG_{Int}.

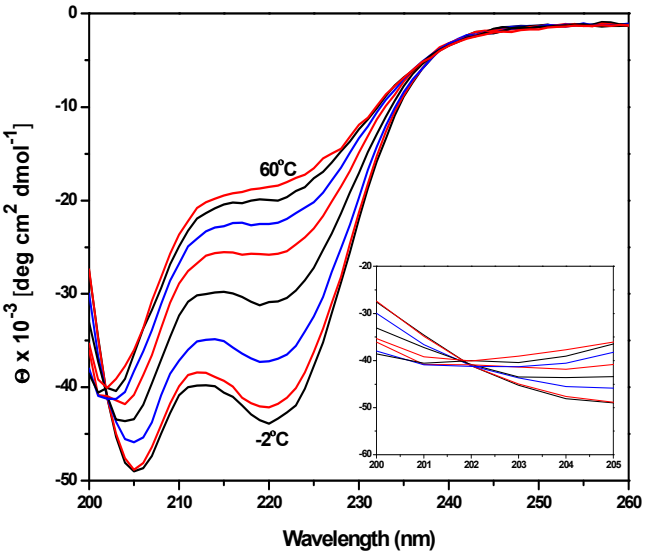

Figure 5-13. Combined spectra of one peptide observed from 200 to 260nm at increasing temperatures from -2°C to 60°C. Crossing of all spectra at ~202nm indicates isodichroic point seen in inset plot.

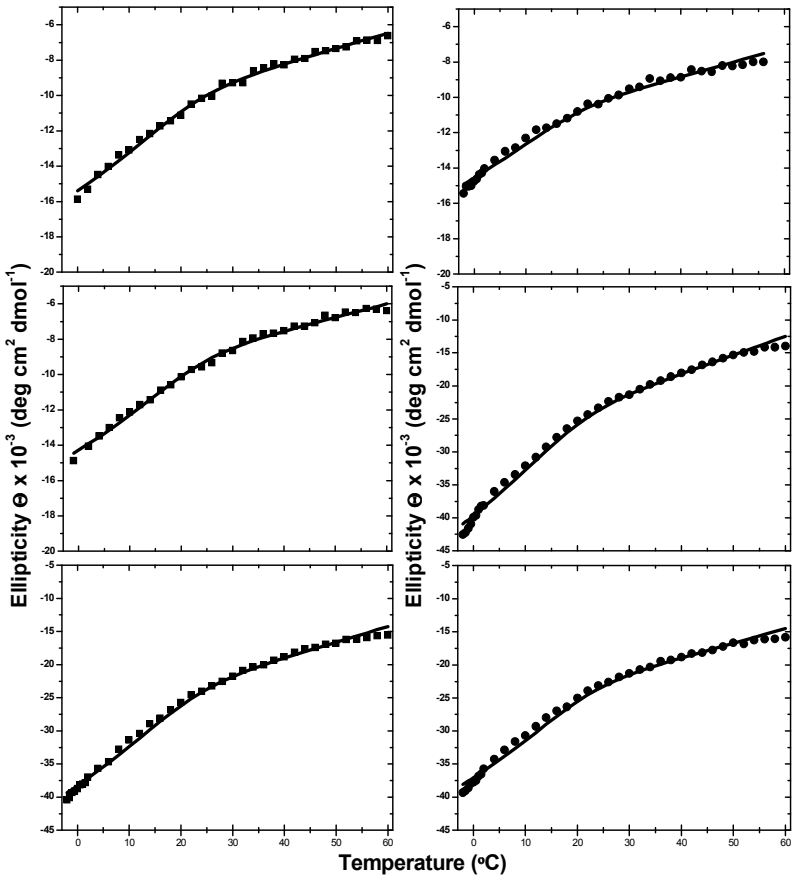

Figure 5-14. Representative data sets and global fits for three replicas of Phe-Met (Left, solid squares) and Phe-Met (ox) (Right, solid circles). For each peptide, a black solid line represents the global fit to all three datasets using the Gibbs Helmholtz equation, as described in Methods. The fitting parameters are, for Phe-Met: ΔH_{Tm} = 26.0 ± 0.7 kcal/mol, ΔC_P = 0.2 ± 0.2 kcal/mol°C and T_m = 18.3 ± 0.3 °C; and for Phe-Met(ox) are: ΔH_{Tm} = 27.1 ± 0.1 kcal/mol, ΔC_P = 0.21 ± 0.02 kcal/mol°C and T_m = 21 ± 1°C were determined for Phe-Met (ox) peptide. Raw ellipticity signal varies for each peptide sample set due to variations in each individual peptide experiment (~150μM concentration). Free energy values were extracted from the global fit at T=0°C and are presented in Figure 5-12.

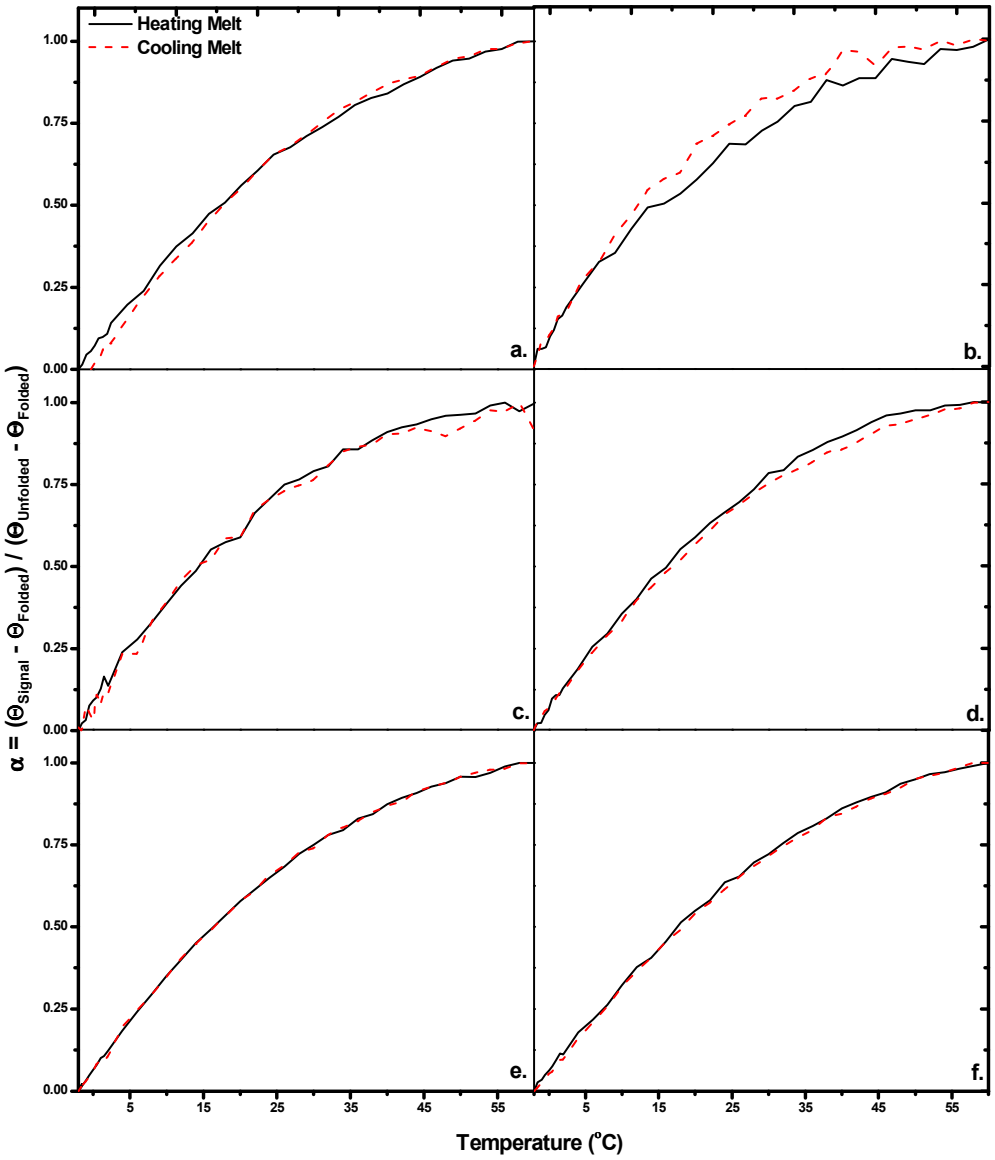

Figure 5-15. Overlaid heating and cooling melt curves for FM, $FM_{(ox)}$, FA, AM, $AM_{(ox)}$, and AA peptides. Heating curves are represented by a black solid line, and cooling curves are represented by a red dashed line. Ellipticity displayed as a fraction of unfolded peptide. FM heating and cooling melt (a), $FM_{(ox)}$ heating and cooling melt (b), FA heating and cooling melt (c), AM heating and cooling melt (d), $AM_{(ox)}$ heating and cooling melt (e), and AA heating and cooling melt (f).

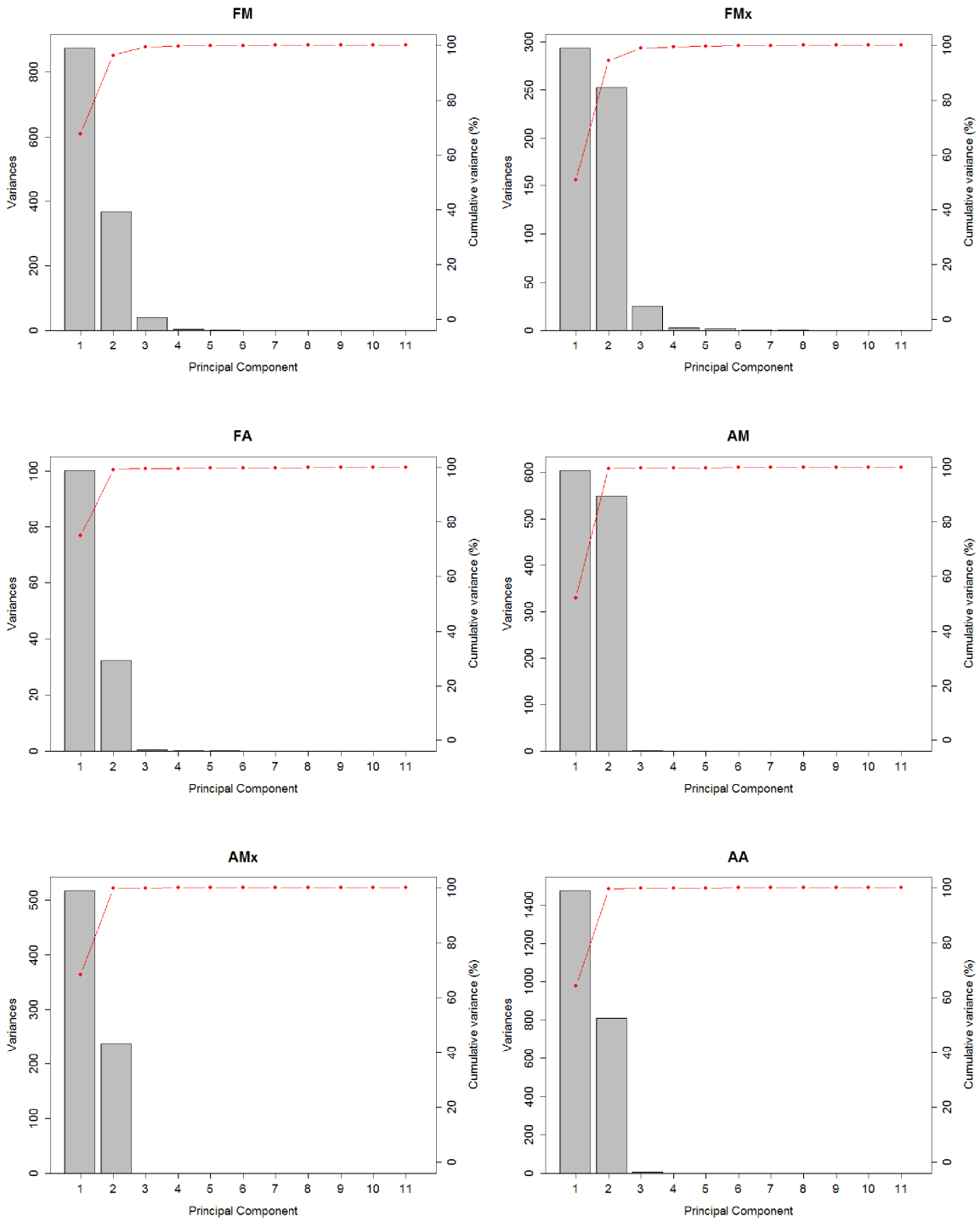

Figure 5-16. Principal Component Analysis. The variance for all principal components is shown as gray bars, and the cumulative percent variance is shown as red lines for all peptides.

FM	PC1	PC2	PC3	PC4	PC5	PC6	PC7	PC8	PC9	PC10	PC11
σ	29.55	19.16	6.30	1.99	1.40	0.85	0.62	0.59	0.37	0.27	0.00
Var Prop.	0.68	0.29	0.03	0.00	0.00	0.00	0.00	0.00	0.00	0.00	0.00
Cum. Prop.	0.68	0.96	0.99	1.00	1.00	1.00	1.00	1.00	1.00	1.00	1.00
FMx	PC1	PC2	PC3	PC4	PC5	PC6	PC7	PC8	PC9	PC10	PC11
σ	17.12	15.89	5.03	1.62	1.46	0.93	0.67	0.55	0.36	0.32	0.00
Var Prop.	0.51	0.44	0.04	0.00	0.00	0.00	0.00	0.00	0.00	0.00	0.00
Cum. Prop.	0.51	0.94	0.99	0.99	1.00	1.00	1.00	1.00	1.00	1.00	1.00
FA	PC1	PC2	PC3	PC4	PC5	PC6	PC7	PC8	PC9	PC10	PC11
σ	10.00	5.69	0.66	0.46	0.36	0.29	0.23	0.21	0.18	0.14	0.00
Var Prop.	0.75	0.24	0.00	0.00	0.00	0.00	0.00	0.00	0.00	0.00	0.00
Cum. Prop.	0.75	0.99	1.00	1.00	1.00	1.00	1.00	1.00	1.00	1.00	1.00
AM	PC1	PC2	PC3	PC4	PC5	PC6	PC7	PC8	PC9	PC10	PC11
σ	24.56	23.44	1.30	0.87	0.59	0.52	0.42	0.31	0.23	0.16	0.00
Var Prop.	0.52	0.48	0.00	0.00	0.00	0.00	0.00	0.00	0.00	0.00	0.00
Cum. Prop.	0.52	1.00	1.00	1.00	1.00	1.00	1.00	1.00	1.00	1.00	1.00
AMx	PC1	PC2	PC3	PC4	PC5	PC6	PC7	PC8	PC9	PC10	PC11
σ	22.72	15.39	0.65	0.39	0.36	0.25	0.21	0.20	0.12	0.12	0.00
Var Prop.	0.68	0.31	0.00	0.00	0.00	0.00	0.00	0.00	0.00	0.00	0.00
Cum. Prop.	0.68	1.00	1.00	1.00	1.00	1.00	1.00	1.00	1.00	1.00	1.00
AA	PC1	PC2	PC3	PC4	PC5	PC6	PC7	PC8	PC9	PC10	PC11
σ	38.38	28.45	2.60	1.19	1.07	0.80	0.47	0.42	0.27	0.19	0.00
Var Prop.	0.64	0.35	0.00	0.00	0.00	0.00	0.00	0.00	0.00	0.00	0.00
Cum. Prop.	0.64	1.00	1.00	1.00	1.00	1.00	1.00	1.00	1.00	1.00	1.00

Principal Component Analysis. The details of PCA for each peptide are shown as standard deviations, proportion of variance, and cumulative proportion of variance.

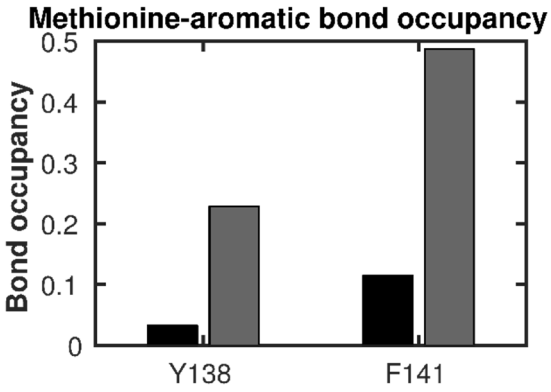

Figure 5-17. S/Ar interactions in CaM simulations. The fractional occupancy of the unoxidized (black) and oxidized (gray) methionine aromatic interaction involving either M144 or M145 from the REMD simulation.

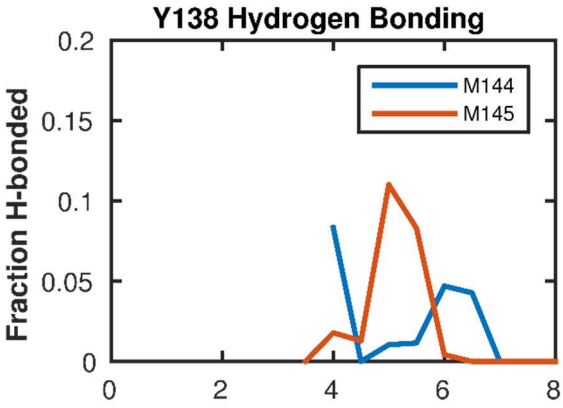

Figure 5-18. Hydrogen bonding of $M^{Ox}144$ and $M^{Ox}145$ with Y138 in the calmodulin simulations. The histogram shows that only a small fraction of Met-aromatic interactions involve a hydrogen bond. The methionine-aromatic distances were binned, and then the fraction of structures that were hydrogen bonded in each bin was plotted.

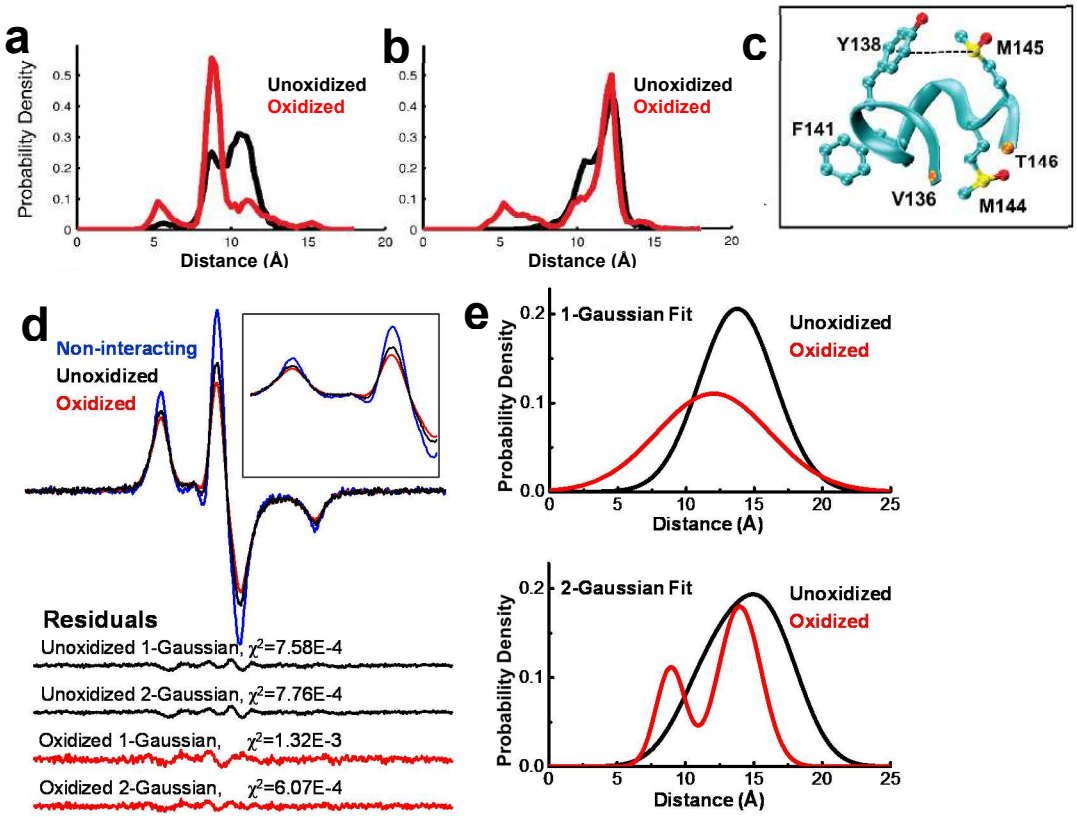

Figure 5-19. Distribution of distances in CaM, from MD simulation , between sulfoxide and center of aromatic ring of Y138-M144 (a) and Y138-M145 (b). (c). A snapshot from MD simulation showing the interaction between Y138 and M145. (d) EPR spectra (200 G scan width, inset shows expanded view of a 50-G portion of the low-field spectra) of CaM spin-labeled at V136 and Y138, showing residuals to fits. (e) Distribution of distances from fits. For unoxidized CaM, residuals show that the

2-Gaussian fit is no better than the 1-Gaussian fit, which is thus shown in Figure 5-4. For oxidized CaM, the 2-Gaussian fit is superior and is thus shown in Figure 5-4.

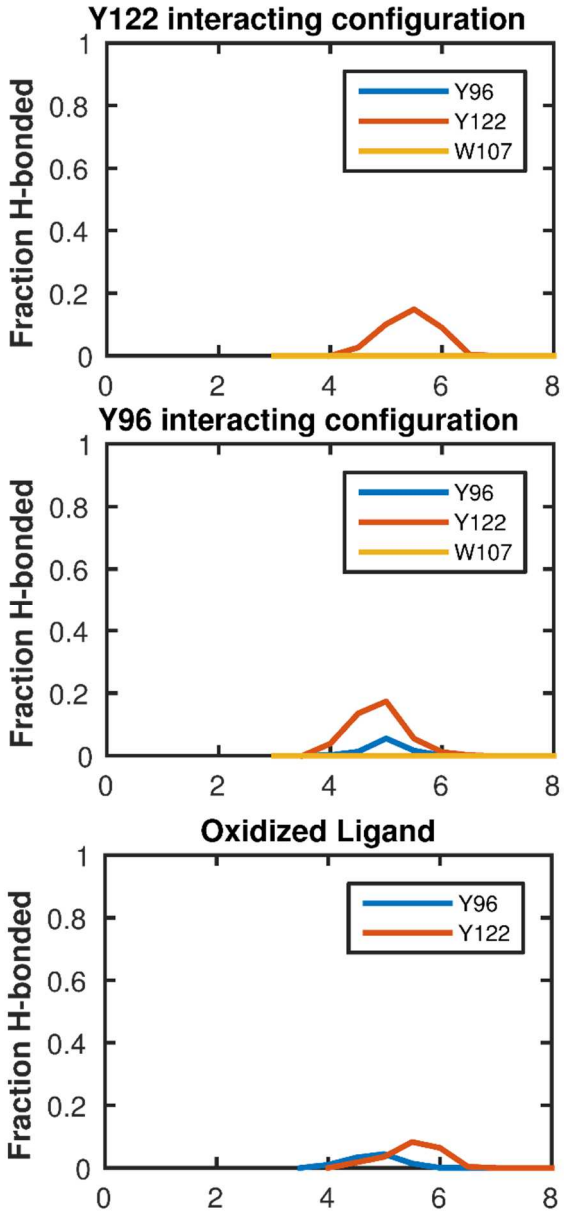

Figure 5-20. Hydrogen bonding in the molecular dynamics simulations of LTα. The fraction of frames in which hydrogen bonding occurs for the range of methionine-aromatic distances. The methionine-aromatic distances were binned, then the fraction of structures that were hydrogen bonded in each bin were plotted. In all three simulations, the fraction of structures that are hydrogen bonded is small.

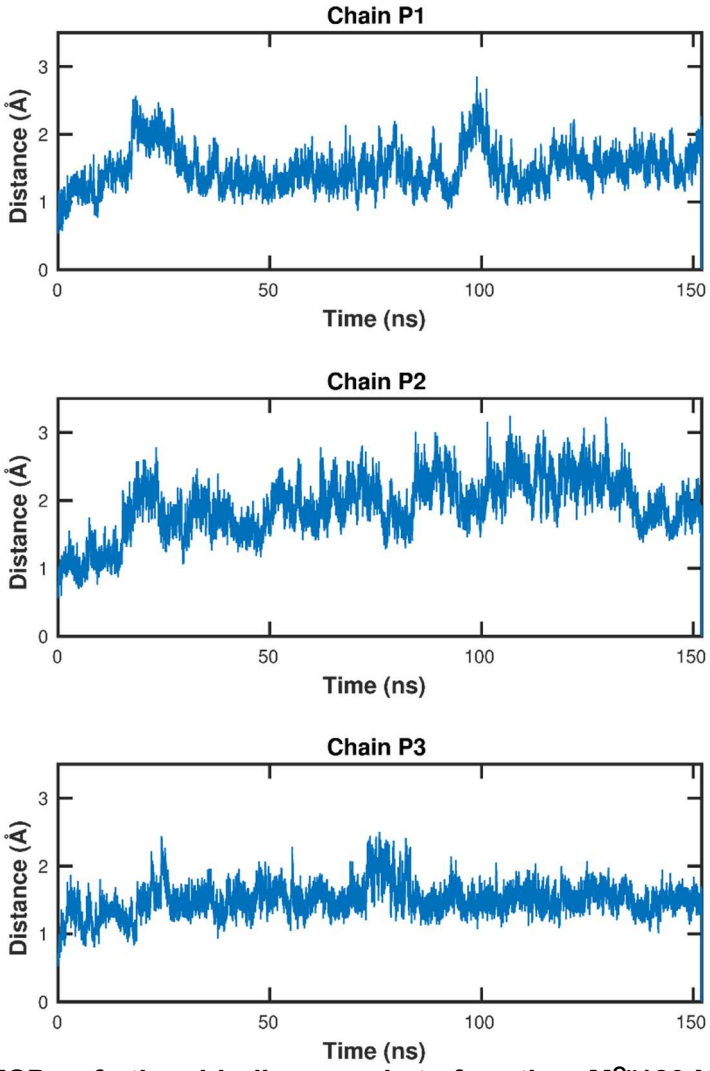

Figure 5-21. RMSD of the binding pocket for the M^{Ox}120-Y122 interacting configuration. The RMSD is shown for the binding pocket (all ligand and receptor residues within 15 Å of M^{Ox}120) for the 3 ligand chains. All three binding pockets are stable.

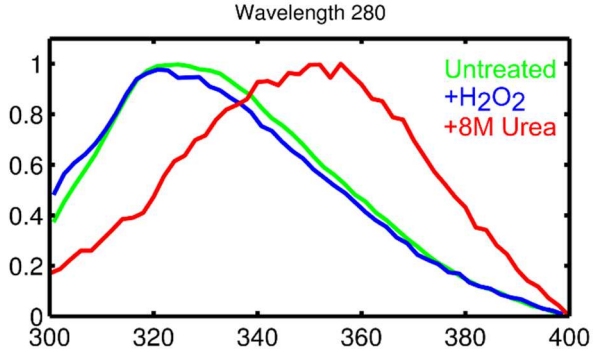

Figure 5-22. Tryptophan fluorescence of LTα after exposure to oxidative stress. LTα was left untreated or oxidized as in cell experiments, and its fluorescence emission spectrum was measured after ~18 hours. The unfolded control sample was dissolved in 8M urea for several hours before measuring its emission spectrum. Fluorescence emission wavelength scans from 300 – 400 nm were taken on a Varian Cary Eclipse Fluorescence spectrometer at an excitation wavelength of 280 nm and a scan rate of 30 nm/min. Excitation and emission slits were set to 5 nm. The emission spectra were normalized between 0 and 1. Total unfolding in 8M urea causes tryptophan residues to become exposed to polar solvent, resulting in a red-shifted emission spectrum (red). Exposure of LTα to oxidative stress does not result in red-shifting of the emission spectrum (blue) compared with the untreated LTα spectrum (green), indicating that the ligand is stably folded.

Stage	Receptor		Ligand		Steps
	Backbone	Sidechain	Backbone	Sidechain	
1	1	1	1	1	10^6
2	0.1	1	1	1	10^6
3	0.01	1	1	1	10^6
4	0	1	1	1	10^6
5	0	0.1	1	1	10^6
6	0	0.01	1	1	10^6
7	0	0.005	1	1	10^6
8	0	0	1	1	10^6
9	0	0	0.1	1	10^6
10	0	0	0.01	1	10^6
11	0	0	0	1	10^6
12	0	0	0	0.1	10^6
13	0	0	0	0.01	10^6
14	0	0	0	0.005	10^6
15	0	0	0	0	10^6

Table 5-9. Relaxation schedule for the $M^{Ox}120$-receptor complex simulations. Restraint spring constants are given in kcal/mol/Å^2.

Chapter 6 – Rationally selected mutations in the TNFR1 preligand assembly domain ablate self-interactions but preserve ligand binding

6.1. Introduction

Tumor necrosis factor receptor (TNFR) 1 is the prototypical member of the TNFR superfamily. When activated, it triggers pro-inflammatory signaling via a well-characterized signaling cascade that culminates in activation of NF-κB (72). TNFR1 exists on the membrane as self-associated homodimers (55), which are bound and activated by its cognate ligands, TNF and LTα (58). Members of the TNF receptor superfamily are notable for having extracellular domains comprised of multiple cysteine-rich domains (CRDs). TNFR1 in particular contains 4 CRDs, each consisting of 3 pairs of disulfide-linked cysteines (75). CRD1 is also known as the preligand assembly domain (PLAD) and is responsible for receptor self-association (55), while ligand binding occurs through CRD2 and CRD3 (8). The long standing model for activation holds that homotrimeric ligand binds to TNFR1 to bring together 3 receptor chains. The TNFR1 cytosolic death domains are consequently trimerized, and with this stoichiometry, are then able to bind intracellular adapter proteins. However, this model does not explain the significance of preligand receptor dimers, nor does it explain overexpression-induced activation (19) and spontaneous activation in disease mutants (37).

The trimerization model also does not suggest a role for ligand/receptor clusters that form on the cell membrane, modeled by us and others as organized lattices (43, 56, 57, 60-62). Structural analysis indicates that the TNFR1 PLAD and

ligand-binding interfaces are distinct and distant from each other. Thus the receptor homodimer survives ligand binding to produce a hexagonal network of receptor-receptor edges linked by trimeric ligand/receptor vertices.

We have recently uncovered evidence for an alternative mechanism of TNF receptor activation involving conformational change of the receptor dimer (60). In our proposed model, ligand/receptor, receptor/receptor, and receptor/membrane interactions combine to produce a reconfiguration of the extracellular domain upon ligand/receptor network formation. The signal mechanically propagates through the cell membrane by hinging of the transmembrane helices (53) to expose the cytosolic death domains and allow them to bind adapter proteins. This model does not require receptor trimerization to form the signaling apparatus, permitting ligand-independent activation.

In light of the evidence that receptor dimers initiate signaling, we hypothesized that disruption of dimers by mutagenesis in the PLAD would inhibit ligand-independent TNFR1 activity. TNFR1 inhibition is an active area of therapeutic interest. Currently available therapies acting on the TNFR1 pathway, including Etanercept, Adalimumab, and Infliximab, work by sequestering TNF or LTα and reducing its bioavailability (245). However, these drugs can cause significant life-threatening side-effects and are not always effective (246, 247). Deng et al. previously targeted receptor dimerization to ameliorate inflammatory signaling due to abnormal TNFR1 activity using a soluble PLAD peptide (27). However, sPLAD also prevented ligand binding and the study did not decouple loss of signaling due to reduced receptor self-association and ligand blockade, a

critical distinction if we are to engineer a novel therapeutic strategy for TNFR inhibition.

Chan et al. performed a mutagenic analysis of the TNFR1 dimerization domain in their seminal study of the TNFR1/2 preligand assembly domains (55). Among their mutants, KY19/20AA and K32A were found to disrupt receptor self-association. However, these mutations affect amino acids (Y20 and K32) that are buried and form extensive intra-protomeric contacts, especially joining CRD1 to CRD2. Thus, they cannot be reasonably expected to preserve the native protein fold. Indeed, both mutants showed reduced binding to the conformation-selective monoclonal antibodies MAB225 and Clone 4.12. Deletion of the PLAD in its entirety (residues 1-55) was likewise found not to dimerize or bind ligand and several have noted that this modification is not expected to result in wholesale conformational disruption due to its apparent stability as an isolated module (248-251). The PLAD deletion mutant did have an intact binding epitope for MAB225, but not Clone 4.12. However the epitopes of these antibodies were not known so deletion of residues 1-55 may have either removed or deformed the antibody epitope. Branschadel et al. have alternatively argued a scaffold role for CRD1, wherein non-covalent contacts between CRD1 and CRD2 are necessary to preserve the ligand-binding interface of CRD2 and CRD3 (76).

Proper folding of TNFR1 has more recently been shown to be highly-sensitive to point mutations in CRD1 and elsewhere. Lobito et al. showed the formation of disulfide-linked oligomers (an indication that intramolecular disulfide bonds are not forming correctly) in the H22Y, C33G, T50M, C52F, C88R, and

R92P mutants associated with TRAPS. Mutation of any cysteine obviously results in a mismatch of disulfide pairs and misfolding is not surprising. H22 and T50, like Chan's Y20 and K32 mutations, project into the protein core and make intra-molecular contacts. R92Q is notable for folding correctly and retaining its ability to bind ligand, but R92P disrupts both.

This study mutates rationally selected amino acids in the PLAD to ablate receptor dimers. We hypothesize that TNFR1 signaling can be inhibited in a manner not dependent on ligand-blockade, by reducing dimerization affinity of the receptor. Future studies will target receptor dimerization by small-molecule inhibition.

6.2. Materials and Methods

6.2.1 Plasmid preparation and transfection

All plasmids encoding TNFR1 were generated using standard cloning technique. The pEXFP-n1-TNFR1 constructs were prepared previously(60) and pCMV6-XL5 TNFR1 was purchased from Origene. All mutations were introduced by Quikchange mutagenesis and sequenced to ensure the correct sequence. pGL-NF-κB and pRL-CMV were purchased from Promega. FLAG-LTα was expressed, purified, and dialyzed in our lab as described previously(43).

Transient transfection was carried out using the calcium phosphate method. HEK293 cells, maintained in DMEM with 10% FBS, 4mM L-Glutamine, and penicillin/streptomycin were plated at ~20% confluence in 12-well, 6-well, or 10 cm plates. Transfectant volume and total DNA was scaled according to culture

volume. The following day, cells were transfected by adding 50 μL transfection mixture with 1 μg total DNA to every 1 mL of media.

6.2.2 FRET

HEK293 cells were transfected with 0.5 μg pECFP-TNFR1ΔCD and 1.5 μg pEYFP-TNFR1ΔCD in a 12-well plate. The following day, cells were lifted with TrypLE, resuspended in phenol red-free DMEM, and plated on poly-D-Lysine coated plates. Cells were allowed to settle at room temperature for 1 hour before imaging. Live-cell FRET imaging was performed on a Nikon Eclipse TE200 inverted microscope and a 20x objective configured as in our previous study (60) with minor modifications detailed here. Cells were imaged in the EYFP and ECFP channels every 15 s for 5 min. Between image captures, acceptor was bleached by continuous exposure through the EYFP excitation channel. Image analysis was carried out in ImageJ. FRET efficiency of each cell was determined as the intercept of the linear fit of normalized EYFP fluorescence plotted against ECFP enhancement. FRET efficiencies were plotted against EYFP intensity of individual cells and fit to a two-parameter saturable binding curve.

6.2.3 Co-immunoprecipitation

Co-immunoprecipitation was performed using anti-FLAG M2 agarose beads (Invitrogen) according to the manufacturer instructions. 1 μg pCMV6-XL5-TNFR1 and 9 μg pCDNA3.1 (for correct total DNA) were transfected into HEK293 cells in a 10 cm plate. After 48 hours, cells were lifted by gentle shearing, washed, and then resuspended in ice-cold PBS, then transferred to 1.5 mL centrifuge tubes. FLAG-LTα was added at 20 ng/mL and incubated for 30 minutes at 4 °C. Cells

were then washed 3 times in ice-cold PBS and resuspended in RIPA lysis buffer. Co-immunoprecipitated samples were incubated with M2 agarose beads overnight with rocking at 4 °C. TNFR1 was detected by Western blot using rabbit α-TNFR1 (Abcam, ab19139).

6.2.4 NF-κB luciferase reporter assay

HEK293 cells were transfected one day after seeding in a 6-well plate with 0.1 μg pCMV6-XL5-TNFR1, 0.1 μg pRL-CMV, 1 μg pGL4.32-(NFκB)-RE, and 0.8 μg pCDNA3.1. After 48 hours, cells were lifted with TrypLE, resuspended in phenol red-free DMEM, and seeded in octuplicate into 384-well plates. Firefly and renilla luciferase was measured using the Promega Dual-Glo kit according to the manufacturer instructions.

6.3. Results

6.3.1 Analysis of the TNFR1 dimerization interface

We first analyzed the crystal structure of the TNFR1 extracellular domain dimer (1ncf) to select residues that stabilize interactions between protomer chains, but are not expected to play a substantial architectural role within the protomer. Such residues are found in CRD1 with sidechains that project away from the protein core and are within 5 Å of reactive atoms on the opposite chain (Figure 6-1). We first identified 4 residues that satisfied these criteria. Glutamine is a potential hydrogen bond donor or acceptor and Q17 is in range of the backbone or sidechains of K35 and G36 and the sidechain of E54 of the opposite protomer. K19 is positively charged and can potentially form a salt bridge with D49. H34

potentially stacks with its counterpart on the opposite chain, and may also serve as a hydrogen donor to the backbone oxygen of C33. Lastly, Q48 can potentially hydrogen bond with its opposite.

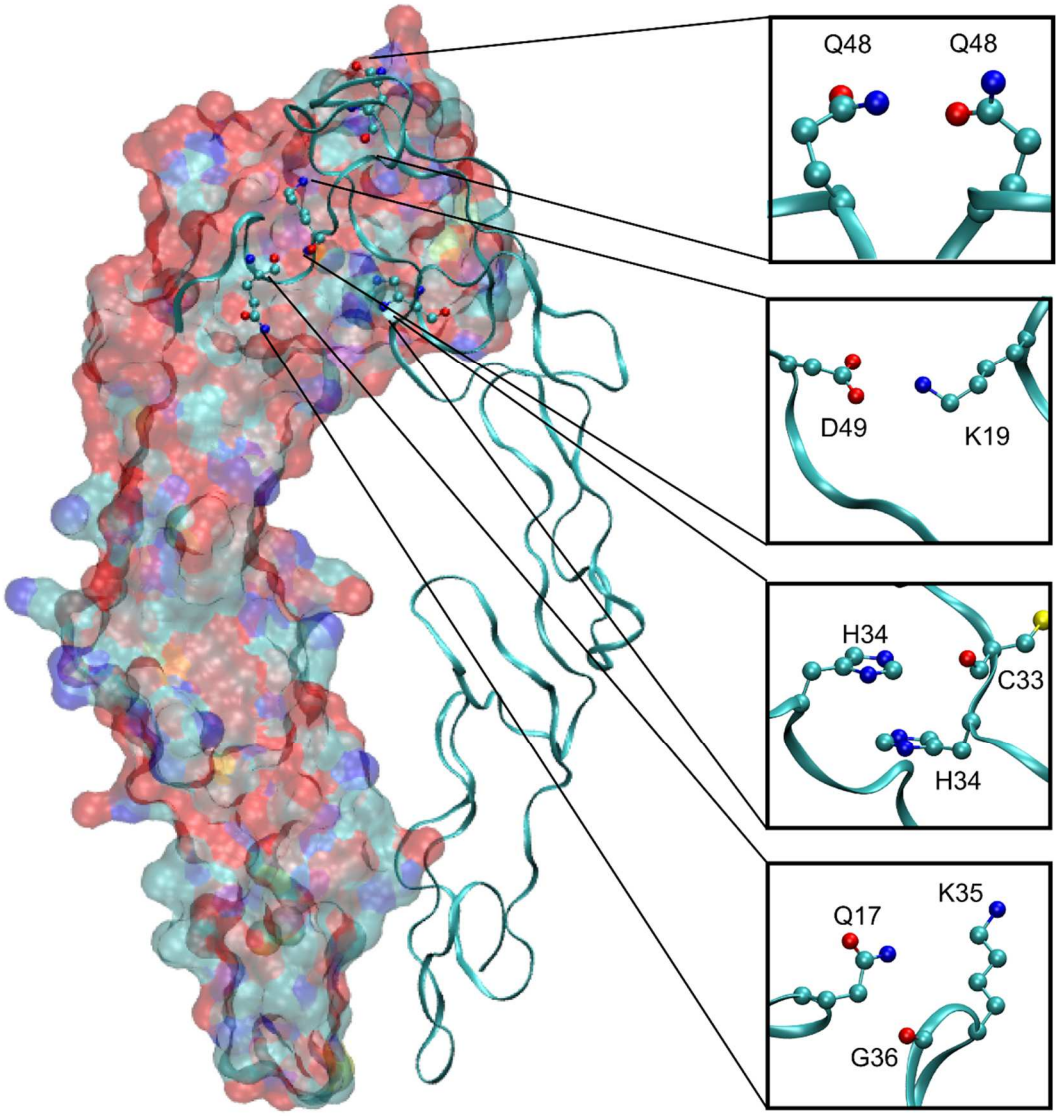

Figure 6-1. Selected residues for mutation and their interaction partners in the TNFR1 PLAD.

6.3.2 Selected mutants in the PLAD reduce dimer affinity

To determine whether selected polymorphisms of interacting PLAD residues can reduce the dimerization affinity of TNFR1, we tested our mutants

using a previously established photobleaching FRET assay (60). We first subcloned plasmids for each TNFR1 mutant in which an ECFP or EYFP fluorophore was inserted in place of its death domain. The plasmids were then cotransfected in a 4:1 EYFP:ECFP ratio to increase the percentage of donors fluorophores that would dimerize with acceptors. Normalized ECFP-enhancement was plotted against EYFP depletion and the intercept where EYFP would be fully bleached was taken as F_D (fluorescence in absence of acceptor). The initial ECFP was normalized to unity and taken as F_{DA} (fluorescence in presence of acceptor). FRET efficiency was calculated as FRET = $1-(F_{DA}/F_D)$ (252). All mutants displayed an essentially linear donor-enhancement vs. acceptor-depletion profile, indicating that our FRET constructs, and by extension, our TNFR1 mutants are dimeric (91).

The plot of FRET efficiency vs. EYFP for each cell can be fit to a two-parameter saturable binding curve to extract dissociation constant (K_d) and $FRET_{max}$ (an indicator of how near the fluorophores are when dimerized) (Figure 6-4) (82, 90). In the case of our mutants, we expect an increase in K_d, which corresponds to reduced dimer affinity and a larger monomer population. $FRET_{max}$ is not expected to change. We observed (Figure 6-2) a nearly 5-fold increase in K_d for K19A and H34A and more than a 5-fold increase in K_d for Q48A compared to wild type. The Q17A mutation did not substantially affect K_d. This indicates that we can modulate the proportion of TNFR1 dimers by rationally selected point mutations. However, this assay cannot rule out the possibility that misfolding of receptors is interrupting dimerization.

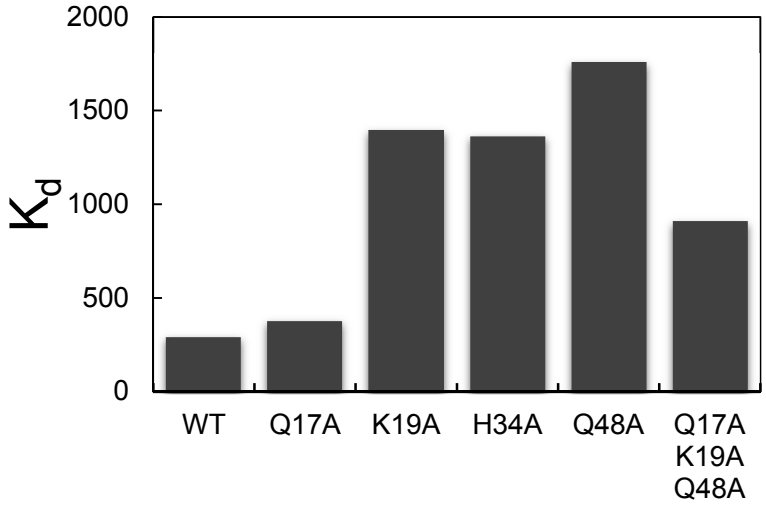

Figure 6-2. K_d as determined from fitting acceptor-selective photobleaching FRET data to a two-parameter binding curve. Q17A dimerizes with roughly the same affinity as WT. All other mutants (Q17A, K19A, H34A, Q48A, and the triple mutant Q17AK19AQ48A) result in a > 3-fold increase in K_d.

6.3.3 Reduced dimer affinity does not necessarily prevent ligand binding

We co-immunoprecipitated TNFR1 with its ligand, LTα, to indicate whether TNFR1 mutants are properly folded and to show that mutations reducing dimer affinity do not necessarily ablate ligand-binding. Previous studies have suggested that receptor dimerization is necessary for ligand binding, however this hypothesis does not resonate with analysis of the TNFR1 structures, which clearly shows the ligand-binding and dimerization motifs to be distinct. This is the first study that rationally targets the PLAD while trying to preserve receptor conformation and especially ligand-binding affinity. None of the selected mutants is directly involved in ligand binding or stabilizing the monomer architecture.

Co-immunoprecipitation of LTα with transiently transfected full-length (death domain included) TNFR1 mutants revealed that ligand-binding and

dimerization affinity are not strictly correlated (Figure 6-3). Endogenous expression levels of TNFR1 were not detectable, therefore the visible bands on the Western Blots are the transfected mutants. H34 is included in the binding epitope of Ab19139, thus it did not appear on the IP or WCE blot and we cannot conclude whether it binds ligand. W107A was previously shown to reduce ligand binding (43) and is included here as a control. Other than H34A, all mutants were confirmed to bind ligand. Q17A appears to bind less LTα. K19A appears to bind more ligand, but this may be a consequence of slightly greater protein load on the gel (see whole cell extract, WCE). Q48A also appears to bind ligand more avidly. Our mutants do not completely abolish dimerization, however a loss in dimer affinity should correspond to a smaller number of TNFR1 dimers on the membrane and would produce a commensurate loss in ligand-binding if the latter phenomenon were directly dependent on receptor self-association. Therefore, these data reject the hypothesis that dimerization is required for ligand binding.

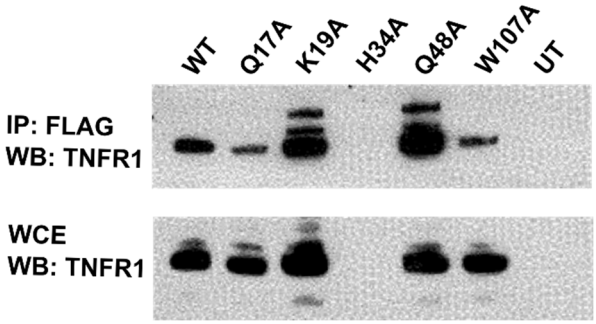

Figure 6-3. Co-Immunoprecipitation of TNFR1 mutants with FLAG-tagged LTα. Q17A, K19A, Q48A, and W107A all bind to LTα. Binding efficiency was reduced with Q17A and W107A (as we have previously shown (175)). Binding to Q48A is enhanced. H34 is in the binding epitope of Ab19139 and its mutant was not labeled. TNFR1 in untransfected (UT) cells was undetectable.

6.4. Concluding remarks

We have shown that dimerization affinity of TNFR1 can be modulated by introducing rationally selected mutants to the PLAD in the extracellular domain. Moreover, we are the first to show that TNFR1 self-assembly and ligand binding ability are not necessarily tied in live cells – that is, our data suggest that TNFR1 monomers are able to bind to ligand. This agrees with a study that first determined the stoichiometry of binding between soluble TNFR1 ECD monomers and LTα (58).

Our data deal exclusively with the extracellular domain and do not address the potential influence of death domain (94, 95) or transmembrane self-interactions. The transmembrane domain does not contain any obvious dimerization motifs, except for a cysteine at its midpoint that has thus far not been shown to form disulfide bonds (55). However, death domain aggregation is a noted finding across the death receptor family (94). Our FRET constructs do not contain death domains, and it is not known how reduced dimerization affinity in the ECD will balance with the dimerization affinity of the whole protein. Previous studies have shown TNFR1 signaling to be sensitive to extracellular mutations (253), therefore cytosolic interactions are not expected to dominate receptor self-association.

Lastly, the goal of this research is to demonstrate whether the TNFR1 dimer is a potential target for modulating its activity. No currently available drug acts on the TNFR1 dimer, although this strategy has been proposed as early as 2000 (254) and has proven successful in animal models (27). However, in that study,

ligand/receptor binding was also prevented, leading to doubt as to whether the observed effects were due to receptor dissociation or ligand blockade. This is an important distinction if we are to fully understand activation/inhibition mechanisms for TNFR1 and generalize to other TNFRs, for which there is therapeutic interest in both agonistic and antagonistic drugs. To explore whether receptor dissociation can be exploited for potential therapeutic applications, ongoing work will determine whether dimer ablation correlates to a loss of both ligand-independent and ligand-induced signaling of the NF-κB pathway. Lastly, future efforts will work towards identifying small-molecule drugs to affect self-association of TNFR1, DR5, and other death receptors.

6.5. Supplementary Figures

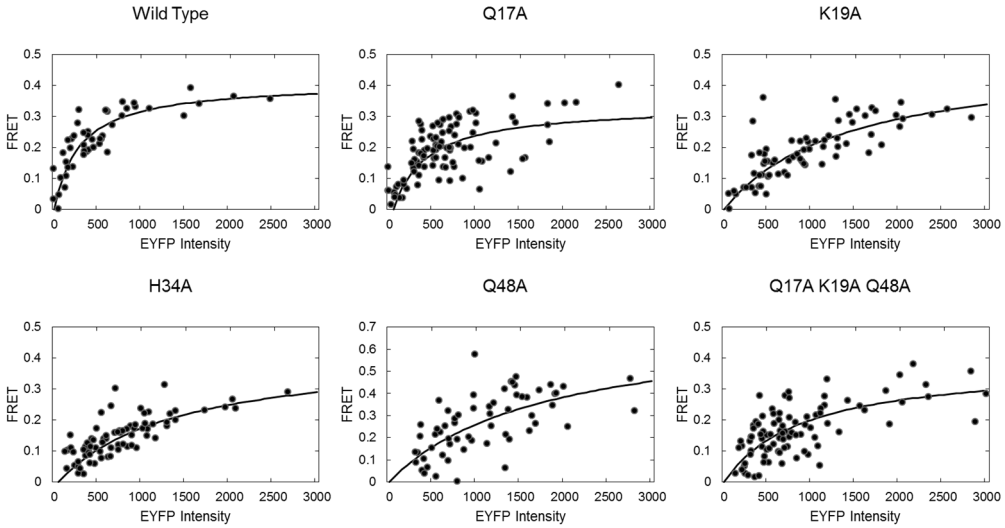

Figure 6-4. Individual plots of FRET vs. EYFP intensity for wild type TNFR1 (A), Q17A (B), K19A (C), H34A (D), Q48A (E), and Q17A K19A Q48A (F). Each fit to a two-parameter saturable binding curve is shown.

Chapter 7 – Concluding remarks and future work

The work here represents only a single facet of the broader goal of the Sachs lab of fully characterizing ligand/receptor networks formed by members of the TNFR superfamily. We show that in the cases of TNFR1 and DR5-L, conformational change occurs at the level of the receptor dimer which is subsumed within a networks. However, we still only have a model of what these networks look like. They certainly contain receptor/receptor and ligand/receptor interactions, but several features have yet to be characterized including network size, binding site saturation, kinetics of their formation, stability, and of course, definitive proof of their arrangements. Certainly a crystal structure of the pre-ligand DR5 (a dimer based on the TM domain, a trimer based on cross-linking studies, or perhaps both exist) would help illuminate the arrangement of those networks. After TNFR1 and DR5, there remain the 27 other members of the TNFR superfamily, not to mention all possible arrangements with ligands. At least for TNFR1, all evidence points to hexagonal lattices, but this has yet to be *seen*. Unfortunately, the feature size lies below the diffraction limit and traditional light microscopy will provide little more utility than it already has. Super-resolution methods have recently advanced and hold promise, with precision in the range of tens of nanometers, but significant improvement must still occur before we can observe network structure.

As far as translating our findings for therapeutic use, there is still much insight to be gained as to the functional significance of ligand/receptor networks. The crystal structure of the LTα-TNFR1 trimer complex was solved in 1993 and

experimental evidence for trimerization had emerged shortly before that, however these described only the binding stoichiometry of the TNFR1 extracellular domain. Francis Chan's crosslinking studies showed that in live cells, networks are found, not trimer complexes. So in functional cell studies, we always observe network-induced activation, not ligand-induced activation. This dissertation provides evidence that receptor dimers are the minimal functional subunit for activation, however we cannot rule out that receptor aggregation due to ligand binding would similarly induce some activation. Networks likely also create synergistic effects due to elevated local concentrations of signaling components. This could amplify signals in both the extracellular and cytosolic spaces through phenomena such as ligand passing. Thus, there is still interest in determining the functional potency of individual ligand/receptor trimer complexes and what bioactivity is gained by network-induced change in local concentration.

We have also begun to further characterize the functional significance of TNFR1 dimerization, both in the absence of ligand and when ligand bound, following the lead set up in chapter 6. Ongoing efforts hope to show that disruption of TNFR1 dimerization results in a concomitant loss in TNFR1 function. This will prove the TNFR1 PLAD as a viable site for inhibitory binding of small molecules or antibodies. We have tested several mutants that reduce dimerization affinity, but do not fully abolish it. Combining mutants and introducing more may accomplish this. We expect that total ablation of TNFR1 dimers would result in the dissociation of ligand/receptor networks and the difference may be observable by confocal microscopy.

Disrupting TNFR1 dimers is one approach for inhibiting TNFR1 activity. The other strategy is to lock TNFR1 in its closed, inactive conformation (although TNFR1 antagonists and agonists are both of interest). We have developed a FRET assay for activation as detailed in Chapter 2 and 6 and can determine a $FRET_{max}$ proportional to the distance between the donor and acceptor fluorophores and a K_D, which provides a measure of binding kinetics. Fluorescent lifetime detection provides both of these pieces of information with a single measurement and in a high-throughput format. Thus, our lab is currently screening for small molecules that modulate TNFR1 dimerization kinetics, cytosolic domain separation, or both. This strategy is being extended to DR5 with the hope of finding agonists that entirely bypass network formation and might better overcome TRAIL resistance. Identified agonists and antagonists will then be subjected to the usual IκBα or caspase 8 detection assays to determine whether they are also functionally effective. Small molecule modulators of TNFR activity represent a novel approach and we hope that this strategy will provide safer and more effective drugs for inflammatory disease and cancer.

References

1. Croft, M., C. A. Benedict, and C. F. Ware. 2013. Clinical targeting of the TNF and TNFR superfamilies. Nat Rev Drug Discov 12:147-168.
2. Bhardwaj, A., and B. B. Aggarwal. 2003. Receptor-mediated choreography of life and death. J Clin Immunol 23:317-332.
3. Croft, M., W. Duan, H. Choi, S. Y. Eun, S. Madireddi, and A. Mehta. 2012. TNF superfamily in inflammatory disease: translating basic insights. Trends Immunol 33:144-152.
4. Takei, Y., and R. Laskey. 2008. Tumor necrosis factor alpha regulates responses to nerve growth factor, promoting neural cell survival but suppressing differentiation of neuroblastoma cells. Mol Biol Cell 19:855-864.
5. Matsumoto, M. 1999. Role of TNF ligand and receptor family in the lymphoid organogenesis defined by gene targeting. J Med Invest 46:141-150.
6. Tansey, M. G., and D. E. Szymkowski. 2009. The TNF superfamily in 2009: new pathways, new indications, and new drugs. Drug Discov Today 14:1082-1088.
7. Idriss, H. T., and J. H. Naismith. 2000. TNF alpha and the TNF receptor superfamily: structure-function relationship(s). Microsc Res Tech 50:184-195.
8. Banner, D. W., A. D'Arcy, W. Janes, R. Gentz, H. J. Schoenfeld, C. Broger, H. Loetscher, and W. Lesslauer. 1993. Crystal structure of the soluble human 55 kd TNF receptor-human TNF beta complex: implications for TNF receptor activation. Cell 73:431-445.
9. Lavrik, I., A. Golks, and P. H. Krammer. 2005. Death receptor signaling. J Cell Sci 118:265-267.
10. Ashkenazi, A., and V. M. Dixit. 1999. Apoptosis control by death and decoy receptors. Curr Opin Cell Biol 11:255-260.
11. Aggarwal, B. B. 2003. Signalling pathways of the TNF superfamily: a double-edged sword. Nat Rev Immunol 3:745-756.
12. Aggarwal, B. B., S. C. Gupta, and J. H. Kim. 2012. Historical perspectives on tumor necrosis factor and its superfamily: 25 years later, a golden journey. Blood 119:651-665.
13. Chen, G., and D. V. Goeddel. 2002. TNF-R1 signaling: a beautiful pathway. Science 296:1634-1635.
14. Aggarwal, B. B., W. J. Kohr, P. E. Hass, B. Moffat, S. A. Spencer, W. J. Henzel, T. S. Bringman, G. E. Nedwin, D. V. Goeddel, and R. N. Harkins. 1985. Human tumor necrosis factor. Production, purification, and characterization. J Biol Chem 260:2345-2354.
15. Etemadi, N., J. K. Holien, D. Chau, G. Dewson, J. M. Murphy, W. S. Alexander, M. W. Parker, J. Silke, and U. Nachbur. 2013. Lymphotoxin α induces apoptosis, necroptosis and inflammatory signals with the same potency as tumour necrosis factor. FEBS J 280:5283-5297.

16. Horiuchi, T., H. Mitoma, S. Harashima, H. Tsukamoto, and T. Shimoda. 2010. Transmembrane TNF-alpha: structure, function and interaction with anti-TNF agents. Rheumatology (Oxford) 49:1215-1228.
17. Crowe, P. D., T. L. VanArsdale, B. N. Walter, C. F. Ware, C. Hession, B. Ehrenfels, J. L. Browning, W. S. Din, R. G. Goodwin, and C. A. Smith. 1994. A lymphotoxin-beta-specific receptor. Science 264:707-710.
18. Browning, J. L., A. Ngam-ek, P. Lawton, J. DeMarinis, R. Tizard, E. P. Chow, C. Hession, B. O'Brine-Greco, S. F. Foley, and C. F. Ware. 1993. Lymphotoxin beta, a novel member of the TNF family that forms a heteromeric complex with lymphotoxin on the cell surface. Cell 72:847-856.
19. Jiang, Y., J. D. Woronicz, W. Liu, and D. V. Goeddel. 1999. Prevention of constitutive TNF receptor 1 signaling by silencer of death domains. Science 283:543-546.
20. Hsu, H., J. Huang, H. B. Shu, V. Baichwal, and D. V. Goeddel. 1996. TNF-dependent recruitment of the protein kinase RIP to the TNF receptor-1 signaling complex. Immunity 4:387-396.
21. Devin, A., A. Cook, Y. Lin, Y. Rodriguez, M. Kelliher, and Z. Liu. 2000. The distinct roles of TRAF2 and RIP in IKK activation by TNF-R1: TRAF2 recruits IKK to TNF-R1 while RIP mediates IKK activation. Immunity 12:419-429.
22. Chen, G., P. Cao, and D. V. Goeddel. 2002. TNF-induced recruitment and activation of the IKK complex require Cdc37 and Hsp90. Mol Cell 9:401-410.
23. Miyamoto, S., M. Maki, M. J. Schmitt, M. Hatanaka, and I. M. Verma. 1994. Tumor necrosis factor alpha-induced phosphorylation of I kappa B alpha is a signal for its degradation but not dissociation from NF-kappa B. Proc Natl Acad Sci U S A 91:12740-12744.
24. Piva, R., G. Belardo, and M. G. Santoro. 2006. NF-kappaB: a stress-regulated switch for cell survival. Antioxid Redox Signal 8:478-486.
25. Sugarman, B. J., B. B. Aggarwal, P. E. Hass, I. S. Figari, M. A. Palladino, and H. M. Shepard. 1985. Recombinant human tumor necrosis factor-alpha: effects on proliferation of normal and transformed cells in vitro. Science 230:943-945.
26. Balkwill, F. 2009. Tumour necrosis factor and cancer. Nat Rev Cancer 9:361-371.
27. Deng, G. M., L. Zheng, F. K. Chan, and M. Lenardo. 2005. Amelioration of inflammatory arthritis by targeting the pre-ligand assembly domain of tumor necrosis factor receptors. Nat Med 11:1066-1072.
28. Kimberley, F. C., A. A. Lobito, R. M. Siegel, and G. R. Screaton. 2007. Falling into TRAPS--receptor misfolding in the TNF receptor 1-associated periodic fever syndrome. Arthritis Res Ther 9:217.
29. Hadziselimovic, F., L. R. Emmons, and H. Gallati. 1995. Soluble tumour necrosis factor receptors p55 and p75 in the urine monitor disease activity and the efficacy of treatment of inflammatory bowel disease. Gut 37:260-263.
30. Poirier, O., V. Nicaud, J. Gariépy, D. Courbon, A. Elbaz, C. Morrison, F. Kee, A. Evans, D. Arveiler, P. Ducimetière, P. Amarenco, and F. Cambien. 2004. Polymorphism R92Q of the tumour necrosis factor receptor 1 gene is associated with myocardial infarction and carotid intima-media thickness--the ECTIM, AXA, EVA and GENIC Studies. Eur J Hum Genet 12:213-219.

31. Amoura, Z., C. Dodé, S. Hue, S. Caillat-Zucman, S. Bahram, M. Delpech, G. Grateau, B. Wechsler, and J. C. Piette. 2005. Association of the R92Q TNFRSF1A mutation and extracranial deep vein thrombosis in patients with Behçet's disease. Arthritis Rheum 52:608-611.
32. Caminero, A., M. Comabella, and X. Montalban. 2011. Role of tumour necrosis factor (TNF)-α and TNFRSF1A R92Q mutation in the pathogenesis of TNF receptor-associated periodic syndrome and multiple sclerosis. Clin Exp Immunol 166:338-345.
33. Cheng, X., Y. Shen, and R. Li. 2014. Targeting TNF: a therapeutic strategy for Alzheimer's disease. Drug Discov Today 19:1822-1827.
34. Van Deventer, S. J. 1997. Tumour necrosis factor and Crohn's disease. Gut 40:443-448.
35. Monaco, C., J. Nanchahal, P. Taylor, and M. Feldmann. 2015. Anti-TNF therapy: past, present and future. Int Immunol 27:55-62.
36. Brennan, F. M., D. Chantry, A. Jackson, R. Maini, and M. Feldmann. 1989. Inhibitory effect of TNF alpha antibodies on synovial cell interleukin-1 production in rheumatoid arthritis. Lancet 2:244-247.
37. Lobito, A. A., F. C. Kimberley, J. R. Muppidi, H. Komarow, A. J. Jackson, K. M. Hull, D. L. Kastner, G. R. Screaton, and R. M. Siegel. 2006. Abnormal disulfide-linked oligomerization results in ER retention and altered signaling by TNFR1 mutants in TNFR1-associated periodic fever syndrome (TRAPS). Blood 108:1320-1327.
38. Chen, Y. F., P. Jobanputra, P. Barton, S. Jowett, S. Bryan, W. Clark, A. Fry-Smith, and A. Burls. 2006. A systematic review of the effectiveness of adalimumab, etanercept and infliximab for the treatment of rheumatoid arthritis in adults and an economic evaluation of their cost-effectiveness. Health Technol Assess 10:iii-iv, xi-xiii, 1-229.
39. Sedger, L. M., and M. F. McDermott. 2014. TNF and TNF-receptors: From mediators of cell death and inflammation to therapeutic giants - past, present and future. Cytokine Growth Factor Rev 25:453-472.
40. Schall, T. J., M. Lewis, K. J. Koller, A. Lee, G. C. Rice, G. H. Wong, T. Gatanaga, G. A. Granger, R. Lentz, and H. Raab. 1990. Molecular cloning and expression of a receptor for human tumor necrosis factor. Cell 61:361-370.
41. Bongartz, T., A. J. Sutton, M. J. Sweeting, I. Buchan, E. L. Matteson, and V. Montori. 2006. Anti-TNF antibody therapy in rheumatoid arthritis and the risk of serious infections and malignancies: systematic review and meta-analysis of rare harmful effects in randomized controlled trials. JAMA 295:2275-2285.
42. McCann, F. E., D. P. Perocheau, G. Ruspi, K. Blazek, M. L. Davies, M. Feldmann, J. L. Dean, A. A. Stoop, and R. O. Williams. 2014. Selective tumor necrosis factor receptor I blockade is antiinflammatory and reveals immunoregulatory role of tumor necrosis factor receptor II in collagen-induced arthritis. Arthritis Rheumatol 66:2728-2738.
43. Valley, C. C., A. K. Lewis, D. J. Mudaliar, J. D. Perlmutter, A. R. Braun, C. B. Karim, D. D. Thomas, J. R. Brody, and J. N. Sachs. 2012. Tumor necrosis factor-

related apoptosis-inducing ligand (TRAIL) induces Death Receptor 5 networks that are highly organized. J Biol Chem.
44. Pan, G., J. Ni, Y. F. Wei, G. Yu, R. Gentz, and V. M. Dixit. 1997. An antagonist decoy receptor and a death domain-containing receptor for TRAIL. Science (New York, N.Y.) 277:815-818.
45. Yang, A., N. S. Wilson, and A. Ashkenazi. 2010. Proapoptotic DR4 and DR5 signaling in cancer cells: toward clinical translation. Curr Opin Cell Biol 22:837-844.
46. Ashkenazi, A., P. Holland, and S. G. Eckhardt. 2008. Ligand-based targeting of apoptosis in cancer: the potential of recombinant human apoptosis ligand 2/Tumor necrosis factor-related apoptosis-inducing ligand (rhApo2L/TRAIL). Journal of clinical oncology : official journal of the American Society of Clinical Oncology 26:3621-3630.
47. Johnstone, R. W., A. J. Frew, and M. J. Smyth. 2008. The TRAIL apoptotic pathway in cancer onset, progression and therapy. Nat Rev Cancer 8:782-798.
48. Stern, H. M., M. Padilla, K. Wagner, L. Amler, and A. Ashkenazi. 2010. Development of immunohistochemistry assays to assess GALNT14 and FUT3/6 in clinical trials of dulanermin and drozitumab. Clin Cancer Res 16:1587-1596.
49. Swers, J. S., L. Grinberg, L. Wang, H. Feng, K. Lekstrom, R. Carrasco, Z. Xiao, I. Inigo, C. C. Leow, H. Wu, D. A. Tice, and M. Baca. 2013. Multivalent scaffold proteins as superagonists of TRAIL receptor 2-induced apoptosis. Mol Cancer Ther 12:1235-1244.
50. Huet, H. A., J. D. Growney, J. A. Johnson, J. Li, S. Bilic, L. Ostrom, M. Zafari, C. Kowal, G. Yang, A. Royo, M. Jensen, B. Dombrecht, K. R. Meerschaert, J. A. Kolkman, K. D. Cromie, R. Mosher, H. Gao, A. Schuller, R. Isaacs, W. R. Sellers, and S. A. Ettenberg. 2014. Multivalent nanobodies targeting death receptor 5 elicit superior tumor cell killing through efficient caspase induction. MAbs 6:1560-1570.
51. Dimberg, L. Y., C. K. Anderson, R. Camidge, K. Behbakht, A. Thorburn, and H. L. Ford. 2013. On the TRAIL to successful cancer therapy? Predicting and counteracting resistance against TRAIL-based therapeutics. Oncogene 32:1341-1350.
52. Lemke, J., S. von Karstedt, J. Zinngrebe, and H. Walczak. 2014. Getting TRAIL back on track for cancer therapy. Cell death and differentiation.
53. Lewis, A. K., Z. M. James, J. E. McCaffrey, A. R. Braun, C. B. Karim, D. D. Thomas, and J. N. Sachs. 2014. Open and closed conformations of the isolated transmembrane domain of death receptor 5 support a new model of activation. Biophys J 106:L21-24.
54. Vilar, M., I. Charalampopoulos, R. S. Kenchappa, A. Simi, E. Karaca, A. Reversi, S. Choi, M. Bothwell, I. Mingarro, W. J. Friedman, G. Schiavo, P. I. Bastiaens, P. J. Verveer, B. D. Carter, and C. F. Ibáñez. 2009. Activation of the p75 neurotrophin receptor through conformational rearrangement of disulphide-linked receptor dimers. Neuron 62:72-83.

55. Chan, F. K., H. J. Chun, L. Zheng, R. M. Siegel, K. L. Bui, and M. J. Lenardo. 2000. A domain in TNF receptors that mediates ligand-independent receptor assembly and signaling. Science 288:2351-2354.
56. Chan, F. K. 2007. Three is better than one: pre-ligand receptor assembly in the regulation of TNF receptor signaling. Cytokine 37:101-107.
57. Naismith, J. H., T. Q. Devine, B. J. Brandhuber, and S. R. Sprang. 1995. Crystallographic evidence for dimerization of unliganded tumor necrosis factor receptor. J Biol Chem 270:13303-13307.
58. Loetscher, H., R. Gentz, M. Zulauf, A. Lustig, H. Tabuchi, E. J. Schlaeger, M. Brockhaus, H. Gallati, M. Manneberg, and W. Lesslauer. 1991. Recombinant 55-kDa tumor necrosis factor (TNF) receptor. Stoichiometry of binding to TNF alpha and TNF beta and inhibition of TNF activity. J Biol Chem 266:18324-18329.
59. Hymowitz, S. G., H. W. Christinger, G. Fuh, M. Ultsch, M. O'Connell, R. F. Kelley, A. Ashkenazi, and A. M. de Vos. 1999. Triggering cell death: the crystal structure of Apo2L/TRAIL in a complex with death receptor 5. Mol Cell 4:563-571.
60. Lewis, A. K., C. C. Valley, and J. N. Sachs. 2012. TNFR1 signaling is associated with backbone conformational changes of receptor dimers consistent with overactivation in the R92Q TRAPS mutant. Biochemistry 51:6545-6555.
61. Ozsoy, H. Z., N. Sivasubramanian, E. D. Wieder, S. Pedersen, and D. L. Mann. 2008. Oxidative stress promotes ligand-independent and enhanced ligand-dependent tumor necrosis factor receptor signaling. J Biol Chem 283:23419-23428.
62. Scott, F. L., B. Stec, C. Pop, M. K. Dobaczewska, J. J. Lee, E. Monosov, H. Robinson, G. S. Salvesen, R. Schwarzenbacher, and S. J. Riedl. 2009. The Fas-FADD death domain complex structure unravels signalling by receptor clustering. Nature 457:1019-1022.
63. Siegel, R. M., J. R. Muppidi, M. Sarker, A. Lobito, M. Jen, D. Martin, S. E. Straus, and M. J. Lenardo. 2004. SPOTS: signaling protein oligomeric transduction structures are early mediators of death receptor-induced apoptosis at the plasma membrane. The Journal of cell biology 167:735-744.
64. Lee, K. H., C. Feig, V. Tchikov, R. Schickel, C. Hallas, S. Schütze, M. E. Peter, and A. C. Chan. 2006. The role of receptor internalization in CD95 signaling. EMBO J 25:1009-1023.
65. Henkler, F., E. Behrle, K. M. Dennehy, A. Wicovsky, N. Peters, C. Warnke, K. Pfizenmaier, and H. Wajant. 2005. The extracellular domains of FasL and Fas are sufficient for the formation of supramolecular FasL-Fas clusters of high stability. The Journal of cell biology 168:1087-1098.
66. Schneider-Brachert, W., V. Tchikov, J. Neumeyer, M. Jakob, S. Winoto-Morbach, J. Held-Feindt, M. Heinrich, O. Merkel, M. Ehrenschwender, D. Adam, R. Mentlein, D. Kabelitz, and S. Schütze. 2004. Compartmentalization of TNF receptor 1 signaling: internalized TNF receptosomes as death signaling vesicles. Immunity 21:415-428.

67. Krippner-Heidenreich, A., F. Tübing, S. Bryde, S. Willi, G. Zimmermann, and P. Scheurich. 2002. Control of receptor-induced signaling complex formation by the kinetics of ligand/receptor interaction. J Biol Chem 277:44155-44163.
68. Boldin, M. P., I. L. Mett, E. E. Varfolomeev, I. Chumakov, Y. Shemer-Avni, J. H. Camonis, and D. Wallach. 1995. Self-association of the "death domains" of the p55 tumor necrosis factor (TNF) receptor and Fas/APO1 prompts signaling for TNF and Fas/APO1 effects. J Biol Chem 270:387-391.
69. Wagner, K. W., E. A. Punnoose, T. Januario, D. A. Lawrence, R. M. Pitti, K. Lancaster, D. Lee, M. von Goetz, S. F. Yee, K. Totpal, L. Huw, V. Katta, G. Cavet, S. G. Hymowitz, L. Amler, and A. Ashkenazi. 2007. Death-receptor O-glycosylation controls tumor-cell sensitivity to the proapoptotic ligand Apo2L/TRAIL. Nat Med 13:1070-1077.
70. Ashkenazi, A., and V. M. Dixit. 1998. Death receptors: signaling and modulation. Science 281:1305-1308.
71. Hsu, H., J. Xiong, and D. V. Goeddel. 1995. The TNF receptor 1-associated protein TRADD signals cell death and NF-kappa B activation. Cell 81:495-504.
72. Wajant, H., and P. Scheurich. 2011. TNFR1-induced activation of the classical NF-κB pathway. FEBS J 278:862-876.
73. Hsu, H., H. B. Shu, M. G. Pan, and D. V. Goeddel. 1996. TRADD-TRAF2 and TRADD-FADD interactions define two distinct TNF receptor 1 signal transduction pathways. Cell 84:299-308.
74. Goh, C. R., C. S. Loh, and A. G. Porter. 1991. Aspartic acid 50 and tyrosine 108 are essential for receptor binding and cytotoxic activity of tumour necrosis factor beta (lymphotoxin). Protein Eng 4:785-791.
75. Naismith, J. H., and S. R. Sprang. 1998. Modularity in the TNF-receptor family. Trends Biochem Sci 23:74-79.
76. Branschädel, M., A. Aird, A. Zappe, C. Tietz, A. Krippner-Heidenreich, and P. Scheurich. 2010. Dual function of cysteine rich domain (CRD) 1 of TNF receptor type 1: conformational stabilization of CRD2 and control of receptor responsiveness. Cell Signal 22:404-414.
77. Tama, F., and Y. H. Sanejouand. 2001. Conformational change of proteins arising from normal mode calculations. Protein Eng 14:1-6.
78. Zheng, W., and B. R. Brooks. 2005. Normal-modes-based prediction of protein conformational changes guided by distance constraints. Biophys J 88:3109-3117.
79. Wang, M., R. T. Borchardt, R. L. Schowen, and K. Kuczera. 2005. Domain motions and the open-to-closed conformational transition of an enzyme: a normal mode analysis of S-adenosyl-L-homocysteine hydrolase. Biochemistry 44:7228-7239.
80. Humphrey, W., A. Dalke, and K. Schulten. 1996. VMD: visual molecular dynamics. J Mol Graph 14:33-38, 27-38.
81. Romo, T. D., and A. Grossfield. 2009. LOOS: an extensible platform for the structural analysis of simulations. Conf Proc IEEE Eng Med Biol Soc 2009:2332-2335.

82. Zacharias, D. A., J. D. Violin, A. C. Newton, and R. Y. Tsien. 2002. Partitioning of lipid-modified monomeric GFPs into membrane microdomains of live cells. Science 296:913-916.
83. Atilgan, A. R., S. R. Durell, R. L. Jernigan, M. C. Demirel, O. Keskin, and I. Bahar. 2001. Anisotropy of fluctuation dynamics of proteins with an elastic network model. Biophys J 80:505-515.
84. Petrone, P., and V. S. Pande. 2006. Can conformational change be described by only a few normal modes? Biophys J 90:1583-1593.
85. Marques, O., and Y. H. Sanejouand. 1995. Hinge-bending motion in citrate synthase arising from normal mode calculations. Proteins 23:557-560.
86. Ma, J., and M. Karplus. 1997. Ligand-induced conformational changes in ras p21: a normal mode and energy minimization analysis. J Mol Biol 274:114-131.
87. Van Wynsberghe, A. W., and Q. Cui. 2006. Interpreting correlated motions using normal mode analysis. Structure 14:1647-1653.
88. Rebelo, S. L., S. E. Bainbridge, M. R. Amel-Kashipaz, P. M. Radford, R. J. Powell, I. Todd, and P. J. Tighe. 2006. Modeling of tumor necrosis factor receptor superfamily 1A mutants associated with tumor necrosis factor receptor-associated periodic syndrome indicates misfolding consistent with abnormal function. Arthritis Rheum 54:2674-2687.
89. Li, M., L. G. Reddy, R. Bennett, N. D. Silva, L. R. Jones, and D. D. Thomas. 1999. A fluorescence energy transfer method for analyzing protein oligomeric structure: application to phospholamban. Biophys J 76:2587-2599.
90. Kelly, E. M., Z. Hou, J. Bossuyt, D. M. Bers, and S. L. Robia. 2008. Phospholamban oligomerization, quaternary structure, and sarco(endo)plasmic reticulum calcium ATPase binding measured by fluorescence resonance energy transfer in living cells. J Biol Chem 283:12202-12211.
91. Autry, J. M., J. E. Rubin, S. D. Pietrini, D. L. Winters, S. L. Robia, and D. D. Thomas. 2011. Oligomeric interactions of sarcolipin and the Ca-ATPase. J Biol Chem 286:31697-31706.
92. Kim, M., C. V. Carman, and T. A. Springer. 2003. Bidirectional transmembrane signaling by cytoplasmic domain separation in integrins. Science 301:1720-1725.
93. Ishikawa-Ankerhold, H. C., R. Ankerhold, and G. P. Drummen. 2012. Advanced fluorescence microscopy techniques--FRAP, FLIP, FLAP, FRET and FLIM. Molecules 17:4047-4132.
94. Sukits, S. F., L. L. Lin, S. Hsu, K. Malakian, R. Powers, and G. Y. Xu. 2001. Solution structure of the tumor necrosis factor receptor-1 death domain. J Mol Biol 310:895-906.
95. Telliez, J. B., G. Y. Xu, J. D. Woronicz, S. Hsu, J. L. Wu, L. Lin, S. F. Sukits, R. Powers, and L. L. Lin. 2000. Mutational analysis and NMR studies of the death domain of the tumor necrosis factor receptor-1. J Mol Biol 300:1323-1333.
96. Zhu, J., C. V. Carman, M. Kim, M. Shimaoka, T. A. Springer, and B. H. Luo. 2007. Requirement of alpha and beta subunit transmembrane helix separation for integrin outside-in signaling. Blood 110:2475-2483.

97. Russ, W. P., and D. M. Engelman. 2000. The GxxxG motif: a framework for transmembrane helix-helix association. Journal of molecular biology 296:911-919.
98. Walczak, H., M. A. Degli-Esposti, R. S. Johnson, P. J. Smolak, J. Y. Waugh, N. Boiani, M. S. Timour, M. J. Gerhart, K. A. Schooley, C. A. Smith, R. G. Goodwin, and C. T. Rauch. 1997. TRAIL-R2: a novel apoptosis-mediating receptor for TRAIL. EMBO J 16:5386-5397.
99. Ashkenazi, A. 2002. Targeting death and decoy receptors of the tumour-necrosis factor superfamily. Nat Rev Cancer 2:420-430.
100. Inbaraj, J. J., M. Laryukhin, and G. A. Lorigan. 2007. Determining the helical tilt angle of a transmembrane helix in mechanically aligned lipid bilayers using EPR spectroscopy. J Am Chem Soc 129:7710-7711.
101. Ghimire, H., S. Abu-Baker, I. D. Sahu, A. Zhou, D. J. Mayo, R. T. Lee, and G. A. Lorigan. 2012. Probing the helical tilt and dynamic properties of membrane-bound phospholamban in magnetically aligned bicelles using electron paramagnetic resonance spectroscopy. Biochim Biophys Acta 1818:645-650.
102. Kim, T., and W. Im. 2010. Revisiting hydrophobic mismatch with free energy simulation studies of transmembrane helix tilt and rotation. Biophys J 99:175-183.
103. Castillo, N., L. Monticelli, J. Barnoud, and D. P. Tieleman. 2013. Free energy of WALP23 dimer association in DMPC, DPPC, and DOPC bilayers. Chem Phys Lipids 169:95-105.
104. Karim, C. B., Z. Zhang, and D. D. Thomas. 2007. Synthesis of TOAC spin-labeled proteins and reconstitution in lipid membranes. Nat Protoc 2:42-49.
105. Grossfield, A. WHAM: the weighted histogram analysis method, version 2.0.7, http://membrane.urmc.rochester.edu/content/wham.
106. Cho, H. S., J. L. Dominick, and M. M. Spence. 2010. Lipid domains in bicelles containing unsaturated lipids and cholesterol. J Phys Chem B 114:9238-9245.
107. De Angelis, A. A., D. H. Jones, C. V. Grant, S. H. Park, M. F. Mesleh, and S. J. Opella. 2005. NMR experiments on aligned samples of membrane proteins. Methods Enzymol 394:350-382.
108. Klein, J. C., A. R. Burr, B. Svensson, D. J. Kennedy, J. Allingham, M. A. Titus, I. Rayment, and D. D. Thomas. 2008. Actin-binding cleft closure in myosin II probed by site-directed spin labeling and pulsed EPR. Proc Natl Acad Sci U S A 105:12867-12872.
109. Pannier, M., S. Veit, A. Godt, G. Jeschke, and H. W. Spiess. 2000. Dead-time free measurement of dipole-dipole interactions between electron spins. J Magn Reson 142:331-340.
110. Jeschke, G., V. Chechik, P. Ionita, A. Godt, H. Zimmermann, J. Banham, C. R. Timmel, D. Hilger, and H. Jung. 2006. DeerAnalysis2006 - a comprehensive software package for analyzing pulsed ELDOR data. Applied Magnetic Resonance 30:473-498.
111. Jeschke, G. 2012.
112. Jo, S., T. Kim, V. G. Iyer, and W. Im. 2008. CHARMM-GUI: a web-based graphical user interface for CHARMM. J Comput Chem 29:1859-1865.

113. Wiley, S. R., K. Schooley, P. J. Smolak, W. S. Din, C. P. Huang, J. K. Nicholl, G. R. Sutherland, T. D. Smith, C. Rauch, C. A. Smith, and R. G. Goodwin. 1995. Identification and characterization of a new member of the TNF family that induces apoptosis. Immunity 3:673-682.
114. Pan, G., K. O'Rourke, A. M. Chinnaiyan, R. Gentz, R. Ebner, J. Ni, and V. M. Dixit. 1997. The receptor for the cytotoxic ligand TRAIL. Science 276:111-113.
115. Thorburn, A. 2004. Death receptor-induced cell killing. Cellular signalling 16:139--144.
116. Schneider, P., and J. Tschopp. 2000. Apoptosis induced by death receptors. Pharmaceutica acta Helvetiae 74:281-286.
117. Bodmer, J.-L., P. Schneider, and J. Tschopp. 2002. The molecular architecture of the TNF superfamily. Trends in biochemical sciences 27:19-26.
118. Walczak, H., R. E. Miller, K. Ariail, B. Gliniak, T. S. Griffith, M. Kubin, W. Chin, J. Jones, a. Woodward, T. Le, C. Smith, P. Smolak, R. G. Goodwin, C. T. Rauch, J. C. Schuh, and D. H. Lynch. 1999. Tumoricidal activity of tumor necrosis factor-related apoptosis-inducing ligand in vivo. Nature medicine 5:157-163.
119. Rowinsky, E. K. 2005. Targeted induction of apoptosis in cancer management: the emerging role of tumor necrosis factor-related apoptosis-inducing ligand receptor activating agents. Journal of clinical oncology : official journal of the American Society of Clinical Oncology 23:9394--9407.
120. Gerspach, J., K. Pfizenmaier, and H. Wajant. 2011. Therapeutic targeting of CD95 and the TRAIL death receptors. Recent patents on anti-cancer drug discovery 6:294-310.
121. Yada, A., M. Yazawa, S. Ishida, H. Yoshida, K. Ichikawa, S. Kurakata, and K. Fujiwara. 2008. A novel humanized anti-human death receptor 5 antibody CS-1008 induces apoptosis in tumor cells without toxicity in hepatocytes. Annals of oncology : official journal of the European Society for Medical Oncology / ESMO 19:1060-1067.
122. Ichikawa, K., W. Liu, L. Zhao, Z. Wang, D. Liu, T. Ohtsuka, H. Zhang, J. D. Mountz, W. J. Koopman, R. P. Kimberly, and T. Zhou. 2001. Tumoricidal activity of a novel anti-human DR5 monoclonal antibody without hepatocyte cytotoxicity. Nature medicine 7:954-960.
123. Rosevear, H. M., A. J. Lightfoot, and T. S. Griffith. 2010. Conatumumab, a fully human mAb against death receptor 5 for the treatment of cancer. Current opinion in investigational drugs (London, England : 2000) 11:688-698.
124. Georgakis, G. V., Y. Li, R. Humphreys, M. Andreeff, S. O'Brien, M. Younes, A. Carbone, V. Albert, and A. Younes. 2005. Activity of selective fully human agonistic antibodies to the TRAIL death receptors TRAIL-R1 and TRAIL-R2 in primary and cultured lymphoma cells: induction of apoptosis and enhancement of doxorubicin- and bortezomib-induced cell death. British journal of haematology 130:501-510.
125. Motoki, K., E. Mori, A. Matsumoto, M. Thomas, T. Tomura, R. Humphreys, V. Albert, M. Muto, H. Yoshida, M. Aoki, T. Tamada, R. Kuroki, H. Yoshida, I. Ishida, C. F. Ware, and S. Kataoka. 2005. Enhanced apoptosis and tumor

regression induced by a direct agonist antibody to tumor necrosis factor-related apoptosis-inducing ligand receptor 2. Clinical cancer research : an official journal of the American Association for Cancer Research 11:3126-3135.
126. Zhang, L., X. Zhang, G. W. Barrisford, and A. F. Olumi. 2007. Lexatumumab (TRAIL-receptor 2 mAb) induces expression of DR5 and promotes apoptosis in primary and metastatic renal cell carcinoma in a mouse orthotopic model. Cancer letters 251:146-157.
127. Adams, C., K. Totpal, D. Lawrence, S. Marsters, R. Pitti, S. Yee, S. Ross, L. Deforge, H. Koeppen, M. Sagolla, D. Compaan, H. Lowman, S. Hymowitz, and A. Ashkenazi. 2008. Structural and functional analysis of the interaction between the agonistic monoclonal antibody Apomab and the proapoptotic receptor DR5. Cell Death Differ 15:751-761.
128. Akazawa, Y., J. L. Mott, S. F. Bronk, N. W. Werneburg, A. Kahraman, M. E. Guicciardi, X. W. Meng, S. Kohno, V. H. Shah, S. H. Kaufmann, M. A. McNiven, and G. J. Gores. 2009. Death receptor 5 internalization is required for lysosomal permeabilization by TRAIL in malignant liver cell lines. Gastroenterology 136:2365-2376.e2361-2367.
129. Donepudi, M. a. 2003. Insights into the regulatory mechanism for caspase-8 activation. Molecular cell 11:543--549.
130. Boatright, K. M., M. Renatus, F. L. Scott, S. Sperandio, H. Shin, I. M. Pedersen, J. E. Ricci, W. a. Edris, D. P. Sutherlin, D. R. Green, and G. S. Salvesen. 2003. A unified model for apical caspase activation. Molecular cell 11:529-541.
131. Blanchard, H., L. Kodandapani, P. R. Mittl, S. D. Marco, J. F. Krebs, J. C. Wu, K. J. Tomaselli, and M. G. Grütter. 1999. The three-dimensional structure of caspase-8: an initiator enzyme in apoptosis. Structure (London, England : 1993) 7:1125-1133.
132. Watt, W., K. a. Koeplinger, a. M. Mildner, R. L. Heinrikson, a. G. Tomasselli, and K. D. Watenpaugh. 1999. The atomic-resolution structure of human caspase-8, a key activator of apoptosis. Structure (London, England : 1993) 7:1135-1143.
133. Muzio, M., B. R. Stockwell, H. R. Stennicke, G. S. Salvesen, and V. M. Dixit. 1998. An induced proximity model for caspase-8 activation. The Journal of biological chemistry 273:2926-2930.
134. MacKenzie, K. R., J. H. Prestegard, and D. M. Engelman. 1997. A transmembrane helix dimer: structure and implications. Science (New York, N.Y.) 276:131-133.
135. Richter, F., T. Liebig, E. Guenzi, A. Herrmann, P. Scheurich, K. Pfizenmaier, and R. E. Kontermann. 2013. Antagonistic TNF receptor one-specific antibody (ATROSAB): receptor binding and in vitro bioactivity. PloS one 8:e72156-e72156.
136. Fricke, F., S. Malkusch, and G. Wangorsch. 2014. Quantitative single-molecule localization microscopy combined with rule-based modeling reveals ligand-induced TNF-R1 reorganization toward higher-order. Histochemistry and cell ….
137. Brown, D. A., and E. London. 1998. Functions of lipid rafts in biological membranes. Annual review of cell and developmental biology 14:111-136.

138. Simons, K., and E. Ikonen. 1997. Functional rafts in cell membranes. Nature 387:569-572.
139. Simons, K., and D. Toomre. 2000. Lipid rafts and signal transduction. Nature reviews Molecular cell biology 1:31-39.
140. Cottin, V., J. E. S. Doan, and D. W. H. Riches. 2002. Restricted localization of the TNF receptor CD120a to lipid rafts: a novel role for the death domain. Journal of immunology (Baltimore, Md. : 1950) 168:4095-4102.
141. Legler, D. F., O. Micheau, M. A. Doucey, J. Tschopp, and C. Bron. 2003. Recruitment of TNF receptor 1 to lipid rafts is essential for TNFalpha-mediated NF-kappaB activation. Immunity 18:655-664.
142. Scheel-Toellner, D., K. Wang, R. Singh, S. Majeed, K. Raza, S. J. Curnow, M. Salmon, and J. M. Lord. 2002. The death-inducing signalling complex is recruited to lipid rafts in Fas-induced apoptosis. Biochem Biophys Res Commun 297:876-879.
143. Muppidi, J. R., and R. M. Siegel. 2004. Ligand-independent redistribution of Fas (CD95) into lipid rafts mediates clonotypic T cell death. Nat Immunol 5:182-189.
144. Song, J. H., M. C. Tse, A. Bellail, S. Phuphanich, F. Khuri, N. M. Kneteman, and C. Hao. 2007. Lipid rafts and nonrafts mediate tumor necrosis factor related apoptosis-inducing ligand induced apoptotic and nonapoptotic signals in non small cell lung carcinoma cells. Cancer Res 67:6946-6955.
145. Min, Y., J. Shi, Y. Zhang, S. Liu, Y. Liu, and D. Zheng. 2009. Death receptor 5-recruited raft components contributes to the sensitivity of Jurkat leukemia cell lines to TRAIL-induced cell death. IUBMB life 61:261-267.
146. Gajate, C., and F. Mollinedo. 2007. Edelfosine and perifosine induce selective apoptosis in multiple myeloma by recruitment of death receptors and downstream signaling molecules into lipid rafts. Blood 109:711-719.
147. Delmas, D., C. Rébé, O. Micheau, A. Athias, P. Gambert, S. Grazide, G. Laurent, N. Latruffe, and E. Solary. 2004. Redistribution of CD95, DR4 and DR5 in rafts accounts for the synergistic toxicity of resveratrol and death receptor ligands in colon carcinoma cells. Oncogene 23:8979-8986.
148. Mérino, D., N. Lalaoui, A. Morizot, P. Schneider, E. Solary, and O. Micheau. 2006. Differential inhibition of TRAIL-mediated DR5-DISC formation by decoy receptors 1 and 2. Molecular and cellular biology 26:7046-7055.
149. Schuck, S., M. Honsho, K. Ekroos, A. Shevchenko, and K. Simons. 2003. Resistance of cell membranes to different detergents. Proceedings of the National Academy of Sciences of the United States of America 100:5795-5800.
150. Lingwood, D., and K. Simons. 2007. Detergent resistance as a tool in membrane research. Nature protocols 2:2159-2165.
151. Feig, M., J. Karanicolas, and C. L. Brooks III. 2001. MMTSB Tool Set. MMTSB NIH Research Resource, The Scripps Research Institute.
152. Brooks, B. R., and R. E. Bruccoleri. 1983. CHARMM: A program for macromolecular energy, minimization, and dynamics calculations. Journal of Computational Chemistry 4:187-217.

153. MacKerell, A. D., M. Feig, and C. L. Brooks. 2004. Improved treatment of the protein backbone in empirical force fields. Journal of the American Chemical Society 126:698-699.
154. Best, R. B., X. Zhu, J. Shim, P. E. M. Lopes, J. Mittal, M. Feig, and A. D. MacKerell. 2012. Optimization of the Additive CHARMM All-Atom Protein Force Field Targeting Improved Sampling of the Backbone phi, psi and Side-Chain chi(1) and chi(2) Dihedral Angles. Journal of Chemical Theory and Computation 8:3257-3273.
155. Ryckaert, J.-P., G. Ciccotti, and H. J. C. Berendsen. 1977. Numerical integration of the cartesian equations of motion of a system with constraints: molecular dynamics of n-alkanes. Journal of Computational Physics 23:327-341.
156. Im, W., M. Feig, and C. L. Brooks. 2003. An implicit membrane generalized born theory for the study of structure, stability, and interactions of membrane proteins. Biophysical journal 85:2900-2918.
157. Im, W., M. S. Lee, and C. L. Brooks. 2003. Generalized Born Model with a Simple Smoothing Function. Journal of Computational Chemistry 24:1691-1702.
158. Martyna, G. J., D. J. Tobias, and M. L. Klein. 1994. Constant-Pressure Molecular-Dynamics Algorithms. Journal of Chemical Physics 101:4177-4189.
159. Mahammad, S., and I. Parmryd. 2008. Cholesterol homeostasis in T cells. Methyl-beta-cyclodextrin treatment results in equal loss of cholesterol from Triton X-100 soluble and insoluble fractions. Biochim Biophys Acta 1778:1251-1258.
160. Wang, G., X. Wang, H. Yu, S. Wei, N. Williams, D. L. Holmes, R. Halfmann, J. Naidoo, L. Wang, L. Li, S. Chen, P. Harran, X. Lei, and X. Wang. 2013. Small-molecule activation of the TRAIL receptor DR5 in human cancer cells. Nature chemical biology 9:84-89.
161. Mongiat, M., G. Ligresti, S. Marastoni, E. Lorenzon, R. Doliana, and A. Colombatti. 2007. Regulation of the extrinsic apoptotic pathway by the extracellular matrix glycoprotein EMILIN2. Molecular and cellular biology 27:7176-7187.
162. Richter, C., S. Messerschmidt, G. Holeiter, J. Tepperink, S. Osswald, A. Zappe, M. Branschadel, V. Boschert, D. A. Mann, P. Scheurich, and A. Krippner-Heidenreich. 2012. The Tumor Necrosis Factor Receptor Stalk Regions Define Responsiveness to Soluble versus Membrane-Bound Ligand. 2515-2529.
163. Zhang, L., Y. Kaizuka, and N. Hanagata. 2012. Imaging of Fas-FasL membrane microdomains during apoptosis in a reconstituted cell-cell junction. Biochemical and biophysical research communications 422:298-304.
164. Kabsch, W., and C. Sander. 1983. Dictionary of protein secondary structure: pattern recognition of hydrogen-bonded and geometrical features. Biopolymers 22:2577-2637.
165. Joosten, R. P., T. A. te Beek, E. Krieger, M. L. Hekkelman, R. W. Hooft, R. Schneider, C. Sander, and G. Vriend. 2011. A series of PDB related databases for everyday needs. Nucleic Acids Res 39:D411-419.
166. Grossfield, A., and T. B. Woolf. 2002. Interaction of tryptophan analogs with POPC lipid bilayers investigated by molecular dynamics calculations. Langmuir 18:198-210.

167. Landolt-Marticorena, C., K. A. Williams, C. M. Deber, and R. A. Reithmeier. 1993. Non-random distribution of amino acids in the transmembrane segments of human type I single span membrane proteins. J Mol Biol 229:602-608.
168. Jacobs, R. E., and S. H. White. 1989. The nature of the hydrophobic binding of small peptides at the bilayer interface: implications for the insertion of transbilayer helices. Biochemistry 28:3421-3437.
169. Wimley, W. C., and S. H. White. 1996. Experimentally determined hydrophobicity scale for proteins at membrane interfaces. Nat Struct Biol 3:842-848.
170. Yau, W. M., W. C. Wimley, K. Gawrisch, and S. H. White. 1998. The preference of tryptophan for membrane interfaces. Biochemistry 37:14713-14718.
171. Fernandes, P. A., and M. J. Ramos. 2004. Theoretical insights into the mechanism for thiol/disulfide exchange. Chemistry 10:257-266.
172. Cristian, L., J. D. Lear, and W. F. DeGrado. 2003. Use of thiol-disulfide equilibria to measure the energetics of assembly of transmembrane helices in phospholipid bilayers. Proc Natl Acad Sci U S A 100:14772-14777.
173. Nezil, F. A., and M. Bloom. 1992. Combined influence of cholesterol and synthetic amphiphillic peptides upon bilayer thickness in model membranes. Biophysical journal 61:1176-1183.
174. Kucerka, N., J. D. Perlmutter, J. Pan, S. Tristram-Nagle, J. Katsaras, and J. N. Sachs. 2008. The effect of cholesterol on short- and long-chain monounsaturated lipid bilayers as determined by molecular dynamics simulations and X-ray scattering. Biophysical journal 95:2792-2805.
175. Valley, C. C., A. Cembran, J. D. Perlmutter, A. K. Lewis, N. P. Labello, J. Gao, and J. N. Sachs. 2012. The Methionine-aromatic Motif Plays a Unique Role in Stabilizing Protein Structure. J Biol Chem 287:34979-34991.
176. Zauhar, R. J., C. L. Colbert, R. S. Morgan, and W. J. Welsh. 2000. Evidence for a strong sulfur-aromatic interaction derived from crystallographic data. Biopolymers 53:233-248.
177. Reid, K. S. C., P. F. Lindley, and J. M. Thornton. 1985. Sulphur-aromatic interactions in proteins. FEBS Letters 190:209-213.
178. Pranata, J. 1997. Sulfur–Aromatic Interactions: A Computational Study of the Dimethyl Sulfide–Benzene Complex. Bioorganic Chemistry 25:213-219.
179. Morgan, R. S., and J. M. McAdon. 1980. Predictor for sulfur-aromatic interactions in globular proteins. International journal of peptide and protein research 15:177-180.
180. Morgan, R. S., C. E. Tatsch, R. H. Gushard, J. McAdon, and P. K. Warme. 1978. Chains of alternating sulfur and pi-bonded atoms in eight small proteins. International journal of peptide and protein research 11:209-217.
181. Tatko, C. D., and M. L. Waters. 2004. Investigation of the nature of the methionine–π interaction in β-hairpin peptide model systems. Protein science : a publication of the Protein Society 13:2515-2522.
182. Viguera, A. R., and L. Serrano. 1995. Side-chain interactions between sulfur-containing amino acids and phenylalanine in ??-helices. Biochemistry 34:8771-8779.

183. Shechter, Y., Y. Burstein, and A. Patchornik. 1975. Selective oxidation of methionine residues in proteins. Biochemistry 14:4497-4503.
184. Wong, P. S., and J. Travis. 1980. Isolation and properties of oxidized alpha-1-proteinase inhibitor from human rheumatoid synovial fluid. Biochem Biophys Res Commun 96:1449-1454.
185. Liebregts, T., B. Adam, C. Bredack, A. Röth, S. Heinzel, S. Lester, S. Downie-Doyle, E. Smith, P. Drew, N. J. Talley, and G. Holtmann. 2007. Immune activation in patients with irritable bowel syndrome. Gastroenterology 132:913-920.
186. Cantin, A. M., S. L. North, G. A. Fells, R. C. Hubbard, and R. G. Crystal. 1987. Oxidant-mediated epithelial cell injury in idiopathic pulmonary fibrosis. J Clin Invest 79:1665-1673.
187. Maier, K., L. Leuschel, and U. Costabel. 1991. Increased levels of oxidized methionine residues in bronchoalveolar lavage fluid proteins from patients with idiopathic pulmonary fibrosis. Am Rev Respir Dis 143:271-274.
188. Szatrowski, T. P., and C. F. Nathan. 1991. Production of large amounts of hydrogen peroxide by human tumor cells. Cancer Res 51:794-798.
189. Palmer, H. J., and K. E. Paulson. 1997. Reactive oxygen species and antioxidants in signal transduction and gene expression. Nutr Rev 55:353-361.
190. Hoshi, T., and S. H. Heinemann. 2001. Regulation of cell function by methionine oxidation and reduction. Journal of Physiology-London 531:1-11.
191. Levine, R. L., B. S. Berlett, J. Moskovitz, L. Mosoni, and E. R. Stadtman. 1999. Methionine residues may protect proteins from critical oxidative damage. Mech Ageing Dev 107:323-332.
192. Kim, G., S. J. Weiss, and R. L. Levine. 2014. Methionine oxidation and reduction in proteins. Biochimica et biophysica acta 1840:901-905.
193. Arakawa, T., Y. Kita, and S. N. Timasheff. 2007. Protein precipitation and denaturation by dimethyl sulfoxide. Biophysical Chemistry 131:62-70.
194. Drazic, A., and J. Winter. 2014. The physiological role of reversible methionine oxidation. Biochimica et biophysica acta 1844:1367-1382.
195. Bigelow, D. J., and T. C. Squier. 2011. Thioredoxin-dependent redox regulation of cellular signaling and stress response through reversible oxidation of methionines. Molecular bioSystems 7:2101-2109.
196. Bigelow, D. J., and T. C. Squier. 2005. Redox modulation of cellular signaling and metabolism through reversible oxidation of methionine sensors in calcium regulatory proteins. Biochimica et biophysica acta 1703:121-134.
197. Lim, J. C., G. Kim, and R. L. Levine. 2013. Stereospecific oxidation of calmodulin by methionine sulfoxide reductase A. Free Radical Biology and Medicine 61:257-264.
198. Younan, N. D., R. C. Nadal, P. Davies, D. R. Brown, and J. H. Viles. 2012. Methionine oxidation perturbs the structural core of the prion protein and suggests a generic misfolding pathway. The Journal of biological chemistry 287:28263-28275.

199. Colombo, G., M. Meli, G. Morra, R. Gabizon, and M. Gasset. 2009. Methionine sulfoxides on prion protein Helix-3 switch on the alpha-fold destabilization required for conversion. PloS one 4:e4296-e4296.
200. Liu, D., D. Ren, H. Huang, J. Dankberg, R. Rosenfeld, M. J. Cocco, L. Li, D. N. Brems, and R. L. Remmele. 2008. Structure and stability changes of human IgG1 Fc as a consequence of methionine oxidation. Biochemistry 47:5088-5100.
201. Klein, J. C., R. J. Moen, E. A. Smith, M. A. Titus, and D. D. Thomas. 2011. Structural and functional impact of site-directed methionine oxidation in myosin. Biochemistry 50:10318-10327.
202. Gao, J., D. H. Yin, Y. Yao, H. Sun, Z. Qin, C. Schöneich, T. D. Williams, and T. C. Squier. 1998. Loss of conformational stability in calmodulin upon methionine oxidation. Biophysical journal 74:1115-1134.
203. Boschek, C. B., T. E. Jones, H. S. Smallwood, T. C. Squier, and D. J. Bigelow. 2008. Loss of the calmodulin-dependent inhibition of the RyR1 calcium release channel upon oxidation of methionines in calmodulin. Biochemistry 47:131-142.
204. Balog, E. M., L. E. Norton, D. D. Thomas, and B. R. Fruen. 2006. Role of calmodulin methionine residues in mediating productive association with cardiac ryanodine receptors. American journal of physiology. Heart and circulatory physiology 290:H794-799.
205. Balog, E. M., L. E. Norton, R. a. Bloomquist, R. L. Cornea, D. J. Black, C. F. Louis, D. D. Thomas, and B. R. Fruen. 2003. Calmodulin oxidation and methionine to glutamine substitutions reveal methionine residues critical for functional interaction with ryanodine receptor-1. The Journal of biological chemistry 278:15615-15621.
206. Bartlett, R. K., R. J. Bieber Urbauer, A. Anbanandam, H. S. Smallwood, J. L. Urbauer, and T. C. Squier. 2003. Oxidation of Met144 and Met145 in calmodulin blocks calmodulin dependent activation of the plasma membrane Ca-ATPase. Biochemistry 42:3231-3238.
207. Anbanandam, A., R. J. Bieber Urbauer, R. K. Bartlett, H. S. Smallwood, T. C. Squier, and J. L. Urbauer. 2005. Mediating molecular recognition by methionine oxidation: conformational switching by oxidation of methionine in the carboxyl-terminal domain of calmodulin. Biochemistry 44:9486-9496.
208. Yin, D., K. Kuczera, and T. C. Squier. 2000. The sensitivity of carboxyl-terminal methionines in calmodulin isoforms to oxidation by H(2)O(2) modulates the ability to activate the plasma membrane Ca-ATPase. Chemical research in toxicology 13:103-110.
209. Gao, J., Y. Yao, and T. C. Squier. 2001. Oxidatively modified calmodulin binds to the plasma membrane Ca-ATPase in a nonproductive and conformationally disordered complex. Biophys J 80:1791-1801.
210. Walsh, M., and F. C. Stevens. 1978. Chemical modification studies on the Ca2+-dependent protein modulator: the role of methionine residues in the activation of cyclic nucleotide phosphodiesterase. Biochemistry 17:3924-3928.
211. Balog, E. M., E. L. Lockamy, D. D. Thomas, and D. A. Ferrington. 2009. Site-specific methionine oxidation initiates calmodulin degradation by the 20S proteasome. Biochemistry 48:3005-3016.

212. Chaiswing, L., and T. D. Oberley. 2010. Extracellular/microenvironmental redox state. Antioxid Redox Signal 13:449-465.
213. Rose, G. D., A. R. Geselowitz, G. J. Lesser, R. H. Lee, and M. H. Zehfus. 1985. HYDROPHOBICITY OF AMINO-ACID RESIDUES IN GLOBULAR-PROTEINS. Science 229:834-838.
214. Dougherty, D. A. 1996. Cation-pi interactions in chemistry and biology: a new view of benzene, Phe, Tyr, and Trp. Science 271:163-168.
215. Bogan, A. A., and K. S. Thorn. 1998. Anatomy of hot spots in protein interfaces. Journal of Molecular Biology 280:1-9.
216. Greenfield, N. J. 2006. Using circular dichroism collected as a function of temperature to determine the thermodynamics of protein unfolding and binding interactions. Nat Protoc 1:2527-2535.
217. Marqusee, S., and R. L. Baldwin. 1987. Helix stabilization by Glu-...Lys+ salt bridges in short peptides of de novo design. Proc Natl Acad Sci U S A 84:8898-8902.
218. Pearson, K. 1901. LIII. On lines and planes of closest fit to systems of points in space. The London, Edinburgh, and Dublin Philosophical Magazine and Journal of Science 2:559-572.
219. Sacksteder, C. A., J. E. Whittier, Y. Xiong, J. Li, N. A. Galeva, M. E. Jacoby, S. O. Purvine, T. D. Williams, M. C. Rechsteiner, D. J. Bigelow, and T. C. Squier. 2006. Tertiary structural rearrangements upon oxidation of Methionine145 in calmodulin promotes targeted proteasomal degradation. Biophys J 91:1480-1493.
220. Babu, Y. S., C. E. Bugg, and W. J. Cook. 1988. Structure of calmodulin refined at 2.2 A resolution. J Mol Biol 204:191-204.
221. Kuboniwa, H., N. Tjandra, S. Grzesiek, H. Ren, C. B. Klee, and A. Bax. 1995. Solution structure of calcium-free calmodulin. Nat Struct Biol 2:768-776.
222. Mukherjea, P., J. F. Maune, and K. Beckingham. 1996. Interlobe communication in multiple calcium-binding site mutants of Drosophila calmodulin. Protein Sci 5:468-477.
223. Jeschke, G. 2012. DEER Distance Measurements on Proteins. Annual Review of Physical Chemistry, Vol 63 63:419-446.
224. Ilardi, E. A., E. Vitaku, and J. T. Njardarson. 2014. Data-mining for sulfur and fluorine: an evaluation of pharmaceuticals to reveal opportunities for drug design and discovery. J Med Chem 57:2832-2842.
225. Frisch, M. J., G. W. Trucks, H. B. Schlegel, G. E. Scuseria, M. A. Robb, J. R. Cheeseman, G. Scalmani, V. Barone, B. Mennucci, G. A. Petersson, H. Nakatsuji, M. Caricato, X. Li, H. P. Hratchian, A. F. Izmaylov, J. Bloino, G. Zheng, J. L. Sonnenberg, M. Hada, M. Ehara, K. Toyota, R. Fukuda, J. Hasegawa, M. Ishida, T. Nakajima, Y. Honda, O. Kitao, H. Nakai, T. Vreven, J. A. Montgomery, J. E. Peralta, F. Ogliaro, M. Bearpark, J. J. Heyd, E. Brothers, K. N. Kudin, V. N. Staroverov, R. Kobayashi, J. Normand, K. Raghavachari, A. Rendell, J. C. Burant, S. S. Iyengar, J. Tomasi, M. Cossi, N. Rega, J. M. Millam, M. Klene, J. E. Knox, J. B. Cross, V. Bakken, C. Adamo, J. Jaramillo, R. Gomperts, R. E. Stratmann, O. Yazyev, A. J. Austin, R. Cammi, C. Pomelli, J. W. Ochterski, R. L. Martin, K. Morokuma, V. G. Zakrzewski, G. A. Voth, P. Salvador, J. J.

Dannenberg, S. Dapprich, A. D. Daniels, Farkas, J. B. Foresman, J. V. Ortiz, J. Cioslowski, and D. J. Fox. 2009. Gaussian 09, Revision D.01. Wallingford CT.
226. Boys, S. F., and F. Bernardi. 1970. The calculation of small molecular interactions by the differences of separate total energies. Some procedures with reduced errors. Molecular Physics 19:553-566.
227. Zhao, Y., and D. G. Truhlar. 2006. A new local density functional for main-group thermochemistry, transition metal bonding, thermochemical kinetics, and noncovalent interactions. Journal of Chemical Physics 125.
228. Reed, A. E., L. A. Curtiss, and F. Weinhold. 1988. Intermolecular interactions from a natural bond orbital, donor-acceptor viewpoint. Chemical Reviews 88:899-926.
229. Mulliken, R. S. 1955. Electronic Population Analysis on LCAO–MO Molecular Wave Functions. I. The Journal of Chemical Physics 23:1833-1840.
230. Cramer, C. J. 2013. Essentials of computational chemistry: theories and models. John Wiley & Sons.
231. Jimenez, M. A., V. Munoz, M. Rico, and L. Serrano. 1994. HELIX STOP AND START SIGNALS IN PEPTIDES AND PROTEINS - THE CAPPING BOX DOES NOT NECESSARILY PREVENT HELIX ELONGATION. Journal of Molecular Biology 242:487-496.
232. Vasquez, M., M. R. Pincus, and H. A. Scheraga. 1987. HELIX COIL TRANSITION THEORY INCLUDING LONG-RANGE ELECTROSTATIC INTERACTIONS - APPLICATION TO GLOBULAR-PROTEINS. Biopolymers 26:351-371.
233. Fealey, M. E., J. W. Gauer, S. C. Kempka, K. Miller, K. Nayak, R. B. Sutton, and A. Hinderliter. 2012. Negative Coupling as a Mechanism for Signal Propagation between C2 Domains of Synaptotagmin I. Plos One 7:11.
234. Horovitz, A. 1996. Double-mutant cycles: A powerful tool for analyzing protein structure and function. Folding & Design 1:R121-R126.
235. Horovitz, A., L. Serrano, B. Avron, M. Bycroft, and A. R. Fersht. 1990. STRENGTH AND COOPERATIVITY OF CONTRIBUTIONS OF SURFACE SALT BRIDGES TO PROTEIN STABILITY. Journal of Molecular Biology 216:1031-1044.
236. Serrano, L., M. Bycroft, and A. R. Fersht. 1991. AROMATIC AROMATIC INTERACTIONS AND PROTEIN STABILITY - INVESTIGATION BY DOUBLE-MUTANT CYCLES. Journal of Molecular Biology 218:465-475.
237. Phillips, J. C., R. Braun, W. Wang, J. Gumbart, E. Tajkhorshid, E. Villa, C. Chipot, R. D. Skeel, L. Kalé, and K. Schulten. 2005. Scalable molecular dynamics with NAMD. J Comput Chem 26:1781-1802.
238. Jorgensen, W. L., J. Chandrasekhar, J. D. Madura, R. W. Impey, and M. L. Klein. 1983. Comparison of Simple Potential Functions for Simulating Liquid Water. Journal of Chemical Physics 79:926-935.
239. MacKerell, A. D., D. Bashford, M. Bellott, R. L. Dunbrack, J. D. Evanseck, M. J. Field, S. Fischer, J. Gao, H. Guo, S. Ha, D. Joseph-McCarthy, L. Kuchnir, K. Kuczera, F. T. K. Lau, C. Mattos, S. Michnick, T. Ngo, D. T. Nguyen, B. Prodhom, W. E. Reiher, B. Roux, M. Schlenkrich, J. C. Smith, R. Stote, J. Straub,

M. Watanabe, J. Wiorkiewicz-Kuczera, D. Yin, and M. Karplus. 1998. All-atom empirical potential for molecular modeling and dynamics studies of proteins. Journal of Physical Chemistry B 102:3586-3616.
240. Best, R. B., X. Zhu, J. Shim, P. E. Lopes, J. Mittal, M. Feig, and A. D. Mackerell. 2012. Optimization of the additive CHARMM all-atom protein force field targeting improved sampling of the backbone φ, ψ and side-chain χ(1) and χ(2) dihedral angles. J Chem Theory Comput 8:3257-3273.
241. Jas, G. S., and K. Kuczera. 2002. Free-energy simulations of the oxidation of C-terminal methionines in calmodulin. Proteins: Structure, Function and Genetics 48:257-268.
242. Darden, T., L. Perera, L. P. Li, and L. Pedersen. 1999. New tricks for modelers from the crystallography toolkit: the particle mesh Ewald algorithm and its use in nucleic acid simulations. Structure with Folding & Design 7:R55-R60.
243. Tuckerman, M., B. J. Berne, and G. J. Martyna. 1992. Reversible Multiple Time Scale Molecular-Dynamics. Journal of Chemical Physics 97:1990-2001.
244. Andersen, H. C. 1983. Rattle - a Velocity Version of the Shake Algorithm for Molecular-Dynamics Calculations. Journal of Computational Physics 52:24-34.
245. Tracey, D., L. Klareskog, E. H. Sasso, J. G. Salfeld, and P. P. Tak. 2008. Tumor necrosis factor antagonist mechanisms of action: a comprehensive review. Pharmacol Ther 117:244-279.
246. Connor, V. 2011. Anti-TNF therapies: a comprehensive analysis of adverse effects associated with immunosuppression. Rheumatol Int 31:327-337.
247. Antoni, C., and J. Braun. 2002. Side effects of anti-TNF therapy: current knowledge. Clin Exp Rheumatol 20:S152-157.
248. Marsters, S. A., A. D. Frutkin, N. J. Simpson, B. M. Fendly, and A. Ashkenazi. 1992. Identification of cysteine-rich domains of the type 1 tumor necrosis factor receptor involved in ligand binding. J Biol Chem 267:5747-5750.
249. Chen, P. C., G. C. DuBois, and M. J. Chen. 1995. Mapping the domain(s) critical for the binding of human tumor necrosis factor-alpha to its two receptors. J Biol Chem 270:2874-2878.
250. Corcoran, A. E., K. Barrett, M. Turner, A. Brown, A. M. Kissonerghis, M. Gadnell, P. W. Gray, Y. Chernajovsky, and M. Feldmann. 1994. Characterization of ligand binding by the human p55 tumour-necrosis-factor receptor. Involvement of individual cysteine-rich repeats. Eur J Biochem 223:831-840.
251. Hsu, K. C., and M. V. Chao. 1993. Differential expression and ligand binding properties of tumor necrosis factor receptor chimeric mutants. J Biol Chem 268:16430-16436.
252. Robia, S. L., K. S. Campbell, E. M. Kelly, Z. Hou, D. L. Winters, and D. D. Thomas. 2007. Förster transfer recovery reveals that phospholamban exchanges slowly from pentamers but rapidly from the SERCA regulatory complex. Circ Res 101:1123-1129.
253. Greco, E., A. Aita, P. Galozzi, A. Gava, P. Sfriso, O. H. Negm, P. Tighe, F. Caso, F. Navaglia, E. Dazzo, M. De Bortoli, A. Rampazzo, L. Obici, S. Donadei, G. Merlini, M. Plebani, I. Todd, D. Basso, and L. Punzi. 2015. The novel S59P mutation in the TNFRSF1A gene identified in an adult onset TNF receptor

associated periodic syndrome (TRAPS) constitutively activates NF-κB pathway. Arthritis Res Ther 17:93.
254. Chan, F. K. 2000. The pre-ligand binding assembly domain: a potential target of inhibition of tumour necrosis factor receptor function. Ann Rheum Dis 59 Suppl 1:i50-53.